

STAVEBNÍ OBZOR

ČÍSLO 1/2019

Obsah čísla:

CALCULATION AND ANALYSIS OF THE PHYSICAL STOREY DRIFT FOR HIGH-RISE FRAME-DIAGRID STRUCTURES <i>Feng Zhang, Qingxuan Shi</i>
INFLUENCE ANALYSIS OF ROCK MECHANICAL PARAMETERS ON THE TBM PENETRATING RATE <i>Jin Lu, Xiaofan Liao</i>
RESTRICTED ZONE OF SUPERPAVE MIX DESIGN AND ITS IMPACT ON RESILIENT MODULUS AND PERMANENT DEFORMATION <i>Arshad Hussain, Fazal Haq, Nauman Javaid, Muhammad Bilal Khurshid</i>
INFLUENCE OF STRAINING BEAMS ON THE SEISMIC FRAGILITY OF DOUBLE-COLUMN BRIDGE PIERS <i>Yuye Zhang, Feng Xiao, Jahangir Badar</i>
EVALUATION ON COMPREHENSIVE BENEFIT OF LARGE-SCALED CONSTRUCTION PROJECT BASED ON FUZZY THEORY: A CASE STUDY OF GUANGZHOU IN CHINA <i>Jianfeng Li, Yousong Wang, Chiyu Luo, Fengwei Cai, Hui Yan</i>
EXPERIMENTAL EVALUATION OF CALCIUM CHLORIDE POWDER EFFECT ON THE REDUCTION OF THE PAVEMENT SURFACE LAYER PERFORMANCE <i>Seyed Ahmad Almasi, Mohammad Mehdi Khabir*</i>
STUDY ON THE INTERACTION BETWEEN FORMWORK SHORING SYSTEMS AND RC STRUCTURES IN A HIGH-RISE BUILDING DURING CONSTRUCTION 2 <i>Suchun Yang, Chengping Qu, Heng Yang</i>
CONSTRUCTION OF NEW MULTI-FUNCTION TYPE ARTIFICIAL BOUNDARY PILLAR FOR TRANSITION FROM OPEN PIT TO UNDERGROUND MINING <i>Honggang Ren, Zhuoying Tan, Panxue Feng</i>
EXPERIMENTAL STUDY OF BITUMINOUS MIXES, FATIGUE PHENOMENON UNDER TANDEM SOLICITATION AT LARGE STRAIN <i>Merbouh M'hammed</i>
WATER HAMMER IN PIPELINE WITH DIFFERENT CHARACTERISTICS OF VALVE CLOSING AND UNSTEADY WALL FRICTION <i>Haixiao Jing, Wen Wang, Guodong Li</i>
CHECKING THE ACCURACY OF LABORATORY TESTS <i>Dvořák Otto, Wald František</i>

CALCULATION AND ANALYSIS OF THE PHYSICAL STOREY DRIFT FOR HIGH-RISE FRAME-DIAGRID STRUCTURES

Feng Zhang¹, Qingxuan Shi²

1. *School of Civil Engineering, Xi'an University of Architecture and Technology, Xi'an, China, Shaanxi Architectural Design and Research Institute Co. Ltd., Xi'an, China; xszzf@hotmail.com*
2. *School of Civil Engineering, Xi'an University of Architecture and Technology, Xi'an, China; qingxuanshi@sina.com*

ABSTRACT

The high-rise frame-diagrid structure is a new type of dual system structure. The inner frame part can create a large space, and the external diagrid part can provide a larger lateral stiffness. In this paper, the lateral deformation formula for the high-rise frame-diagrid structures is derived. The bending deformation of the structure is divided into the bending rotational deformation and the floor rigid rotational deformation. The physical storey drift is proposed. The physical storey drift is directly related to the structural damage. When the structure is in the plastic state, the structure maximum storey drift and maximum physical storey drift are in different positions. It is recommended to use both storey drift and physical storey drift as structural deformation limitation criteria. Finally, the proposed method is used to structural parameters analysis for the high-rise frame-diagrid structure. It provides reference for the structural design.

KEYWORDS

Dual system; Lateral deformation; Bending deformation; Physical storey drift; Parameters analysis

INTRODUCTION

The traditional frame structure has better mechanical behaviour when it is subjected to gravity loads. But the lateral stiffness of the frame structure is caused by the bending and shearing stiffness of the beam and column, and the lateral stiffness is smaller than other structural systems [1]. With the increase of building height, structural deformation cannot be ignored by horizontal loads such as wind and seismic load. For this reason, a diagrid structure with large lateral stiffness is to be used in practice [2, 3]. The diagrid structure is a triangular space grid structure system composed of diagonal columns and ring beams [3]. The diagonal column in the diagrid structure system is mainly subjected to axial force, which can effectively utilize the material mechanical properties to provide greater lateral stiffness [4, 5]. At present, the diagrid structure has been successfully applied to practical projects such as the West Tower of Guangzhou in China, the Hearst Building in New York, and the CCTV headquarters in China [6]. And the super high-rise building approximately under 200 meters high can accommodate the diagrid tube outer cylinder and the interior include frame structures. This typical practice to it is the New York Hearst Building. This structural system can be called a high-rise frame diagrid structure.

High-rise buildings deformation limitation criteria is especially important in structural design [7, 8]. The storey drift is also an important limitation criteria, and frame-diagrid structure is no

exception. The main purpose of limiting the storey drift of high-rise buildings is threefold: (a) to ensure the stability of the structure; (b) to prevent cracking or obvious damage of non-structural components such as infill walls and decoration; (c) to satisfy human comfort under horizontal loads. The seismic hazard showed that there is a clear relationship between the storey drift and the building damage. The storey drift limitation required in the most building design codes [9-12]. However, these specifications do not distinguish different lateral deformation features. For example, the structure dominated by bending deformation will have a large error, which should be deducted the influence of the rotational deformation of the rigid body on the floor in the design. UBC1997 specified the storey drift under wind and seismic loads. IBC2000 storey drift limitation is similar to UBC1997, but it is mainly specified building seismic state. The Chinese seismic code also specified the storey drift limitation of different structural systems [11, 12]. However, in all the literature, there is little research storey drift features for the frame-diagrid structure systems.

In order to study the storey drift of building structures, it is necessary to carefully study the structural deformation caused by horizontal loads. Under the horizontal loads, the structure bending deformation causes the floor rigid rotation. The deformation caused by rigid rotation has no direct relevance to the structural mechanical behaviour, which can be called harmless deformation. Directly causing the stress of structure component is the building shear deformation and rotational deformation, which can be called harmful deformation, also can be called physical deformation [13]. Generally, the harmless deformation for the low-rise and mid-rise structure is negligible. The shear deformation of frame structure is dominant, and the bending deformation accounts for a small proportion. The bending deformation of the high-rise shear wall structure is dominant, and the shear deformation accounts for a small proportion. So the physical deformation of the high-rise shear wall structure cannot be ignored [14-16]. The frame-diagrid structure is a dual system, which has both bending and shear deformation. Therefore, under the horizontal loads, the structural deformation of the frame-diagrid structure needs further study.

In this paper, the bending and shear deformation of frame-diagrid structure is analysed. The storey drift composition of the structural system is analysed. The calculation method for the physical storey drift is given.

FRAME-DIAGRID STRUCTURE DEFORMATION THEORETICAL DERIVATION

The horizontal loads of the frame-diagrid structure mainly include wind loads and seismic loads. The simplified analysis model of the frame-diagrid structure is shown in Figure 1. All the diagrid components are merged into a total diagrid, and all the frame components are merged into a total frame. The total diagrid and total frame deformation are uniform at any floors. The structure is subjected to arbitrary horizontal load $q(x)$. The continuous interaction force between the total diagrid and the total frame is $p(x)$. The total frame stiffness is the sum of the shear stiffness of all beam and column components. Introducing C_F is the shear stiffness of the total frame, it can be calculated from the literature [16]. The diagrid stiffness can be calculated by literature [17]. K_D and C_D are the equivalent bending stiffness and shear stiffness of the total diagrid, respectively.

The diagrid structure is regarded as a cantilever beam considering both bending and shear deformation. The relationship among bending moment, shear force and load relationship are as follows [18]:

$$M_D = K_D \frac{dw_M^2(x)}{dx^2} \quad (1)$$

$$V_D = C_D \frac{dw_V(x)}{dx} = -K_D \frac{dw_M^3(x)}{dx^3} \quad (2)$$

$$p_D(x) = p(x) - q(x) = K_D \frac{dw_M^4(x)}{dx^4} \quad (3)$$

where $w_M(x)$ is the deformation caused by the bending deformation, and $w_V(x)$ is the deformation caused by shear deformation. The total deformation $w(x)$ is as follows:

$$w(x) = w_M(x) + w_V(x) \quad (4)$$

According to the definition of the shear force, differentiating with respect to x , we get $dV_F/dx = -q(x)$. Combined with Equation (3), we get:

$$\begin{aligned} p(x) &= K_D \frac{dw_M^4(x)}{dx^4} - \frac{dV_F}{dx} = K_D \frac{dw_M^4(x)}{dx^4} - C_F \left(\frac{d^2 w_M}{dx^2} + \frac{d^2 w_V}{dx^2} \right) \\ &= \left(K_D + \frac{K_D C_F}{C_D} \right) \frac{dw_M^4(x)}{dx^4} - C_F \frac{d^2 w_M}{dx^2} \end{aligned} \quad (5)$$

Introducing $\lambda = \sqrt{\frac{H^2 C_D \cdot C_F}{K_D (C_D + C_F)}}$ and $\xi = x/H$. Equation (5) can be written as follows:

$$\frac{d^4 w_M(\xi)}{d\xi^4} - \lambda^2 \frac{d^2 w_M(\xi)}{d\xi^2} = \frac{H^4 C_D}{K_D (C_D + C_F)} p(\xi) \quad (6)$$

This equation is a bending deformation differential equation for structures. $w_V(\xi)$ and $w_M(\xi)$ can be obtained by Equation (2).

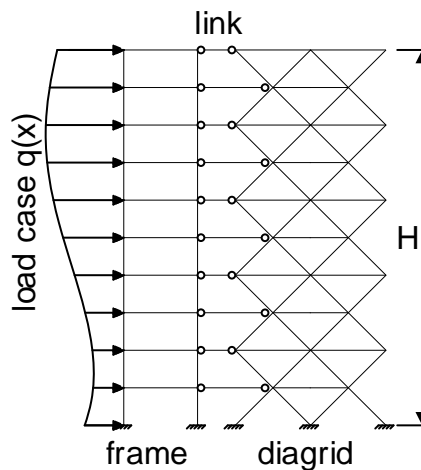


Fig.1 - Simplified analysis model for the frame-diagrid structure

PROPOSED PHYSICAL STOREY DRIFT

The deformation of the structure usually consists of the shear deformation and the bending deformation. The bending deformation consists of the bending rotational deformation and the floor rigid rotational deformation. The floor rigid rotational deformation is caused by the bending deformation of the lower floor. For the frame structure the shear deformation is dominant [1]. However, for the structure with bending deformation, the structural damage is directly related to the maximum bending rotational deformation, which can be called physical deformation [13]. The lateral deformation of the high-rise frame-diagrid structure is shown in Figure 2.

The lateral bending deformation value of the frame-diagrid structure can be obtained by the above Equation (6), and the structural i^{th} storey deformation u_i can be written as follow:

$$u_i = W_i - W_{i-1} \quad (7)$$

where W_i is the i^{th} storey bending deformation; W_{i-1} is the $i-1^{\text{th}}$ storey bending deformation.

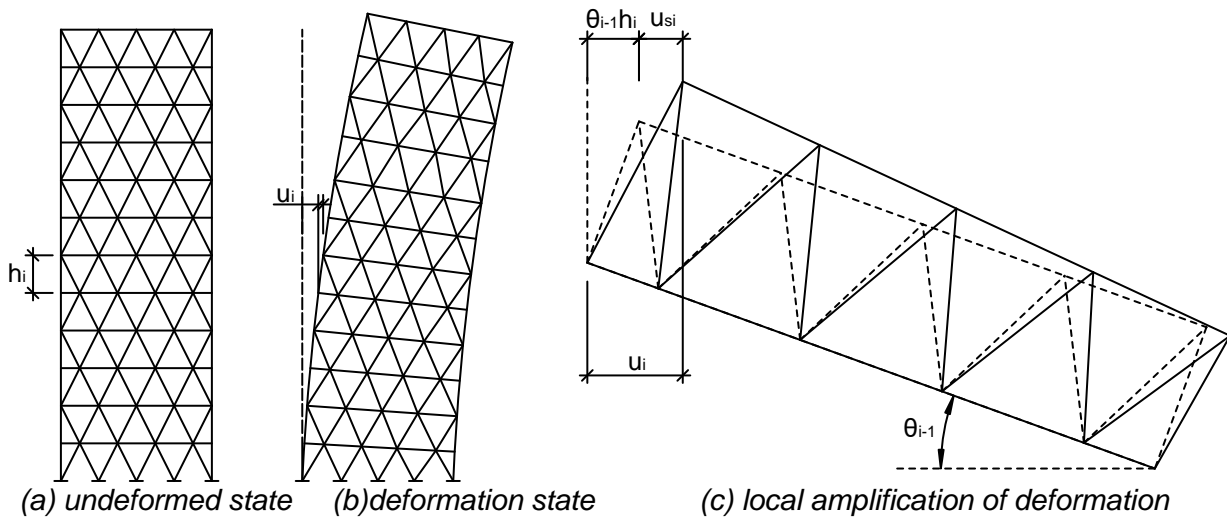


Fig.2 - High-rise frame-diagrid structure lateral deformation

Under the horizontal load, the frame-diagrid structure lateral storey deformation is caused by the shear storey deformation and the bending storey deformation. u_i can be derived as follows:

$$u_i = u_{Vi} + u_{Mi} = u_{Vi} + (u'_{Mi} + \tilde{u}_{Mi}) \quad (8)$$

$$u_{Si} = u_i - \tilde{u}_{Mi} \quad (9)$$

$$\tilde{u}_{Mi} = \theta_{i-1} h_i \quad (10)$$

where u_{Vi} 、 u_{Mi} 、 u'_{Mi} 、 \tilde{u}_{Mi} is the i^{th} storey deformation caused by the shear deformation, the i^{th} storey deformation caused by the bending deformation, the i^{th} storey deformation caused by the bending rotational deformation, and the i^{th} storey deformation caused by the floor rigid rotational deformation. u_{Si} is the storey deformation deducting the floor rigid rotational drift.

$\theta_{i-1} = dw_{Mi-1}(x) / dx$ is floor rigid rotational angle. h_i is the i^{th} storey height of the structure.

In the high-rise buildings \tilde{u}_{Mi} is caused by the floor rigid rotational deformation. The floor rigid rotational deformation does not cause damage of the structure. \tilde{u}_{Mi} can be called harmless storey deformation.

u_{Si} is caused by the shear deformation and bending rotational deformation, which is the directly causing damage of the structural components. u_{Si} can be called harmful storey deformation, also can be called physical storey deformation.

The storey drift is defined as storey deformation divided by storey height. The frame-diagrid structure has both bending deformation and shear deformation. By studying the frame-diagrid structure physical storey drift, the damage location along the height of the structure can be determined quickly.

VERIFICATION EXAMPLE AND DISCUSSION

A 40-storey frame-diagrid structure with rectangular floor plan was designed for a verification example, as shown in Figure 3. The width of the structure is 43.2m; the storey height is 4.5m; the angle of diagonal column θ is 68.2 degree; the total height H is 180m. All the structural material is steel material. The elastic modulus of the material is 200Gpa. The cross section of the components is given in Table 1. The horizontal loads are three commonly used loads Case1-3 in the design of high-rise structure [16]. In Case 1, the top point lateral load is 90kN ; in Case 2, the uniform distributed lateral load 1 kN/m , in Case 3, the reverse triangle distribution lateral load 1.636kN/m. The lateral deformation of the structure is calculated by using the method proposed in the Section 1 of this paper and the finite element method(FEM). The calculated results are compared, as shown in Figure 4. The lateral deformation Case 1 error is 3.4%, the Case 2 error is 4.1%, and the Case 3 error is 3.7%. The shear deformation and bending deformation can be further calculated by proposed method. The ratio of structural shear deformation to bending deformation is different under different cases. The storey drift of the structure under three cases conditions can be calculated by above Equation (7). The results are shown in Figure 5. It can be seen that the storey drift of the frame-diagrid structure is related to the load types. Under the horizontal uniform load, the storey drift increases with the increase of the height of the structure. However, under reverse triangle distribution lateral load or the top point lateral load, the storey drift first increases and then decreases with the increase of the height of the structure.

In order to verify whether the maximum storey drift and physical storey drift are in the same height of the structure, the elastic-plastic model is used for further discussion. The structural arrangement, material and the component section area are the same as the example above Figure 3. This model is named 4FFD6. The dead load is 6.5 kN/m² , including the weight of the floor slab. The live load is 3.5 kN/m² . The Perform-3D software program [19] was used to simulate the linear and nonlinear behaviour of the diagrid structure. The strain-hardening bilinear model is adopted for steel material, and the strain-hardening coefficient is 0.01. The nonlinear structural element used herein fiber element, and takes into account the interaction between the axial force and bending moment of the diagonal column [20]. According to Chinese Code for Seismic Resistance of Buildings [11], GB50011-2010, assuming the building is located in Class II site, the design seismic group is Group 2, and the design basic ground acceleration is 0.20g. Using ATC-40 Pushover capability spectrum method [21], the seismic performance spectrum and the capability spectrum are used to determine the performance points of the structure to evaluate the seismic performance of the structure. The demand spectrum parameters are determined by the horizontal seismic influence coefficient specified by GB50011-2010. The horizontal seismic coefficient is 0.16 for frequently earthquakes, 0.45 for local fortification earthquakes and 0.9 for rarely earthquakes. In this paper, Pushover analysis is performed along the height distribution according to the structure first mode in the horizontal direction.

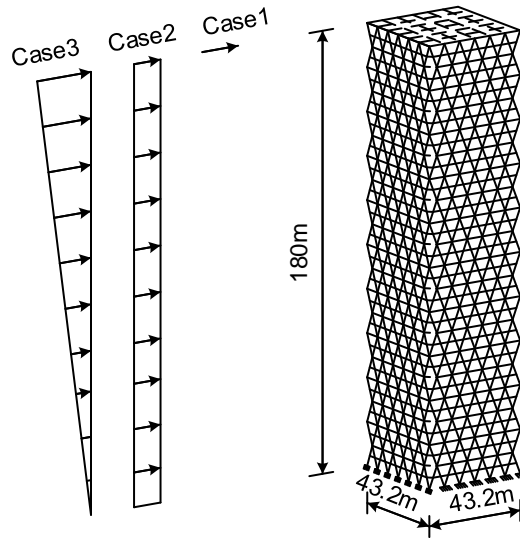


Fig.3 - Example model

Tab. 1 - Model 4FFD6 component cross sections

Storey	Diagonal column section /mm	Frame column section /mm	Ring beam and frame beam section /mm
1-8	Tube 1000×30	Tube 1000×30	Tube 300×800×20
9-16	Tube 750×25	Tube 750×25	
17-24	Tube 650×20	Tube 650×20	
25-40	Tube 550×18	Tube 550×18	

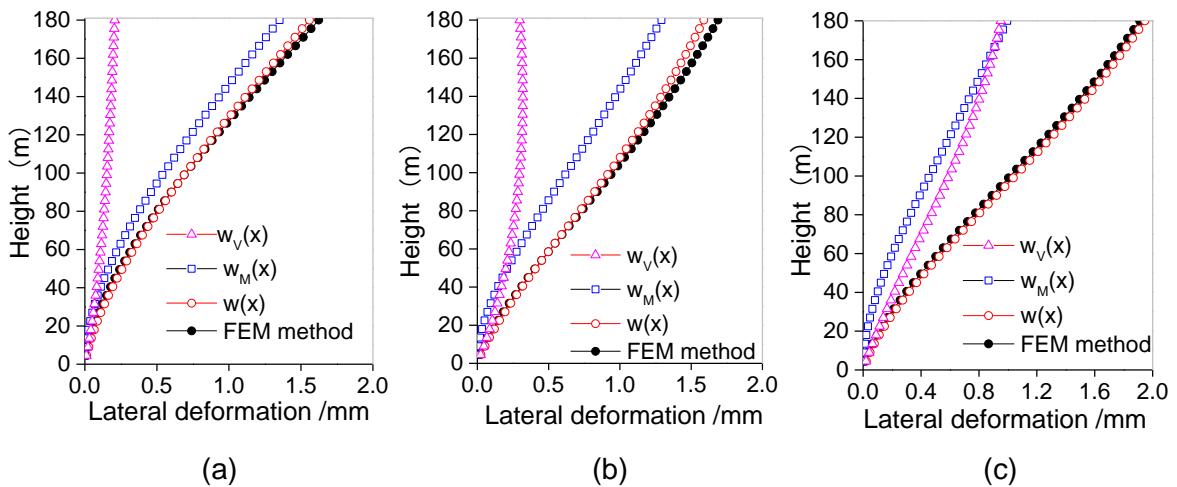


Fig. 4 - Result of lateral deformation. (a) Case 1: Top point lateral load (b) Case 2: Uniform distributed lateral load and (c) Case 3: Reverse triangle distributed lateral load

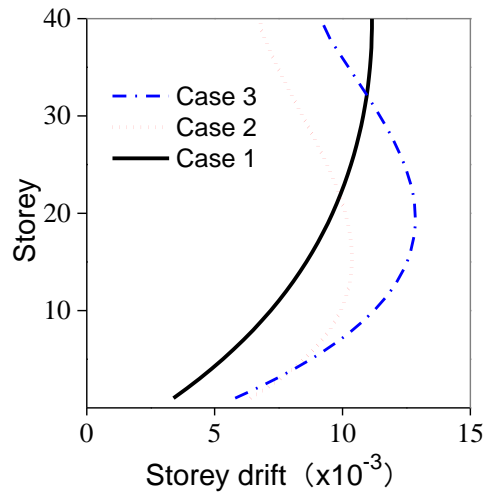


Fig.5 - The storey drift under 3 cases

The curve of the storey drift of the model 4FFD6 during frequently earthquakes and rarely earthquakes are shown in Figure 6, respectively. During frequently earthquakes, the structure maximum storey drift is 1/352, which is on the 25th floor; in this floor the physical storey drift is 1/4471, which accounts for 7.9% of the storey drift. During rarely earthquakes, the structure maximum storey drift is 1/144, which is on the 25th floor; in this floor the physical storey drift is 1/1582, which accounts for 9.1% of the storey drift. The maximum storey physical drift is 1/544 on the 17th floor, which accounts for 34.3% of the storey drift. It can be seen that the structure maximum storey drift and maximum physical storey drift are in different positions under different seismic loads. It is recommended to use both storey drift and physical storey drift as structural deformation limitation criteria.

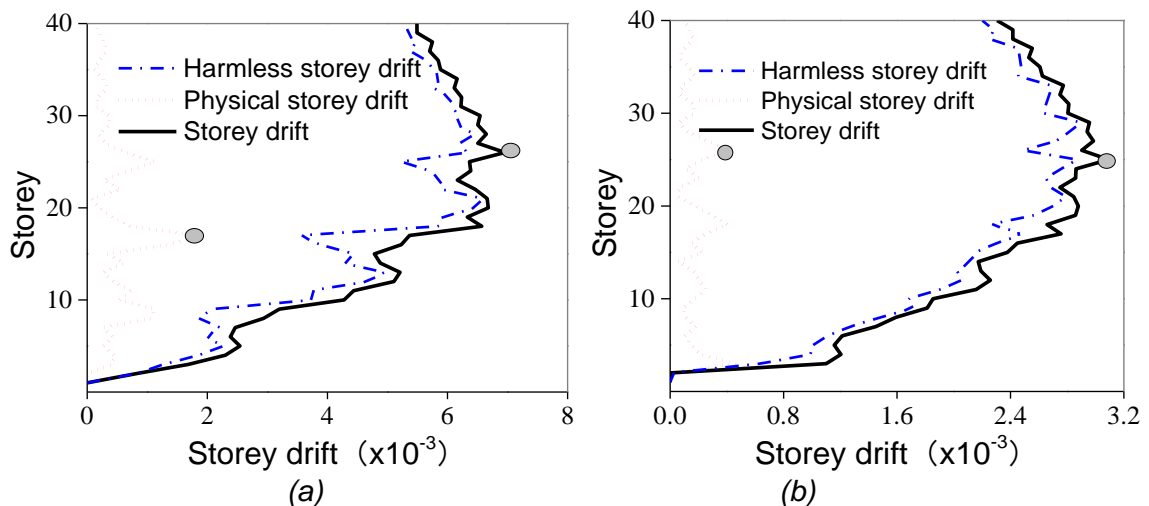


Fig. 6 - Storey drift of model 4FFD6 (a) during frequently earthquakes (b) during rarely earthquakes

STRUCTURAL PARAMETERS ANALYSIS USING STOREY DRIFT

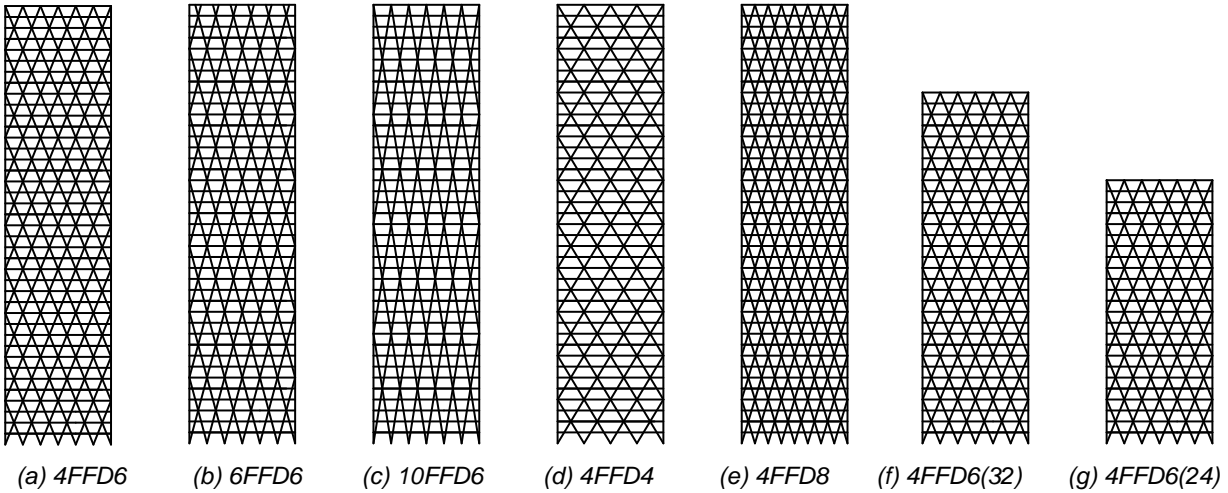


Fig. 7 - Vertical view of structural model

As mentioned above, the physical storey drift is directly related to the structural damage. It is suggested using both storey drift and physical storey drift as structural deformation limitation criteria. The parameters of high-rise frame-diagrid system are analysed by the method proposed in this paper during rarely earthquakes.

On the basis of the model 4FFD6, as shown in Figure 7, by adjusting the parameters such as the diagonal column section, the diagonal column angle, the main ring beam span and structure aspect ratio, nine comparative calculation models are designed, which are: 4FFD6, 4F15FD6, 4F20FD6, 6FFD6, 10FFD6, 4FFD8, 4FFD4, 4FFD6 (32), 4FFD6 (24). For example, model 4FFD6 is 4 stories and 6 spans with each diagrid module. Model 4F15FD6 indicates that the diagonal column section area is 1.5 times that of model 4FFD6. Model 4FFD6 (32) indicates that the model is 32 stories.

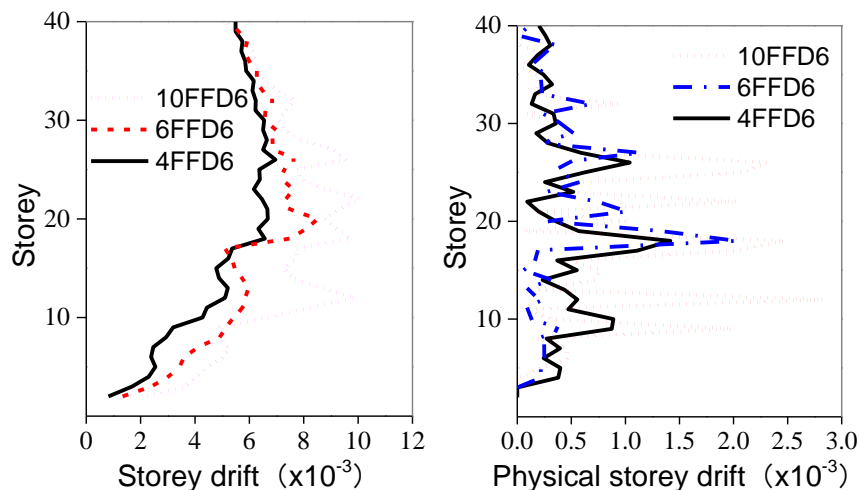


Fig.8 - Storey drift and physical storey drift under different diagonal column angles (The angles of the diagonal columns of 4FFD6, 6FFD6 and 10FFD6 is 68°, 75° and 81°, respectively)

Diagonal column angle

The angles of the diagonal columns of model 4FFD6, 6FFD6 and 10FFD6 are 68°, 75° and 81°, respectively. The storey drift and the physical storey drift are shown in Figure 8. It can be seen that the storey drift of the structure first increases and then decreases along the height direction of the floor, and the angle between the structural diagonal column and the horizontal angle is larger, the storey drift is larger. The physical storey drift increases first and then decreases along the height of the floor, and the larger the angle between the structural diagonal column and the horizontal, the larger the physical storey drift and the larger the variation. Therefore, in the structural design, the structural stress and deformation can be made more reasonable by reasonable adjustment of the angle of the diagonal column, which is beneficial to improve the seismic performance of the structure.

Diagonal column section

The diagonal columns section area of the model 4FFD6, 4F15FD6 and 4F20FD6 are 1x, 1.5x and 2x, respectively, of the model 4FFD6. The storey drift and the physical storey drift curve of each structure are shown in Figure 9. It can be seen that the storey drift of the structure and the physical storey drift first increase and then decrease along the height direction of the floor. The larger the diameter and wall thickness of the inclined column steel tube, the smaller the storey drift and the physical storey drift, the position of the physical storey drift the maximum value rises along the floor. Therefore, in the structural design, the structural stress and deformation can be made more reasonable by reasonable adjustment of the diagonal column section, which is beneficial to improve the seismic performance of the structure.

Main ring beam span

The structural main ring beam spans of the model 4FFD4, 4FFD6 and 4FFD8 are 4 spans, 6 spans and 8 spans. The storey drift and the physical storey drift curve of each structure are shown in Figure 10. The storey drift and the physical storey drift increase first and then decrease along the height direction of the floor. The larger the span number of the main ring beam is, the smaller the storey drift between the layers is, the lower the position of the most value is. But the physical storey drift is not changed greatly. There is a significant difference between the storey drift and the physical storey drift. In the structural design, the structural force and deformation can be made more reasonable by reasonable adjustment of the main ring beam span, which is beneficial to improve the seismic performance of the structure.

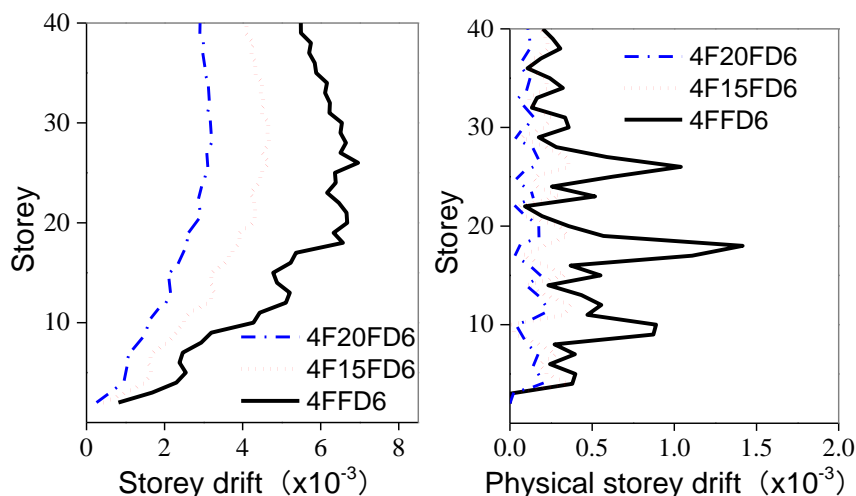


Fig.9 - Storey drift and physical storey drift under different diagonal column section (The diameters and wall thicknesses of the diagonal columns of the models 4FFD6, 4F15FD6 and 4F20FD6 are 1x, 1.5x and 2x, respectively, of the model 4FFD6)

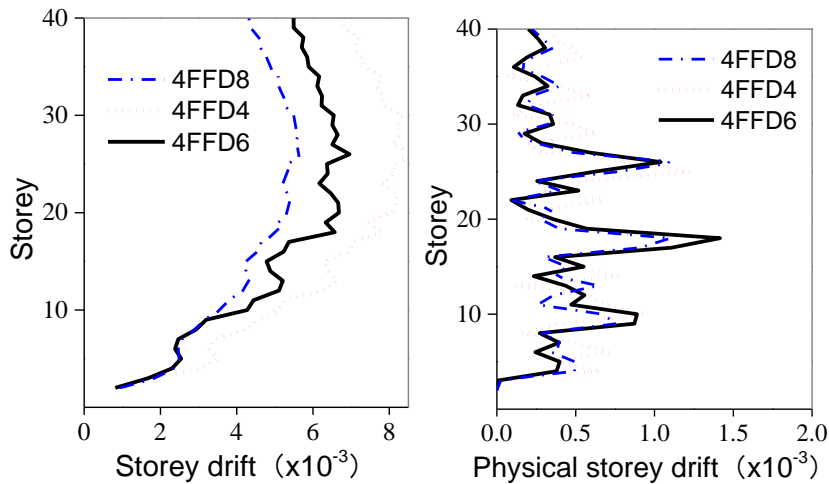


Fig.10 - Storey drift and physical storey drift under different main ring beam span (The structural main ring beam spans of the models 4FFD4, 4FFD6 and 4FFD8 are 4 spans, 6 spans and 8 spans)

Structure aspect ratio

The structural aspect ratios of the model, 4FFD6(24), 4FFD6(32) and 4FFD6 are 2.67, 3.56 span and 4.44, respectively. The storey drift and the physical storey drift of the structure are shown in Figure 11. The storey drift of the structure and the physical storey drift increase first and then decrease along the height direction of the floor. The larger the aspect ratio of the structure, the larger the storey drift and the physical storey drift. In the structural design, the structural strength and deformation can be rationalized by reasonable adjustment of the aspect ratio of the structure, which is beneficial to improve the seismic performance of the structure.

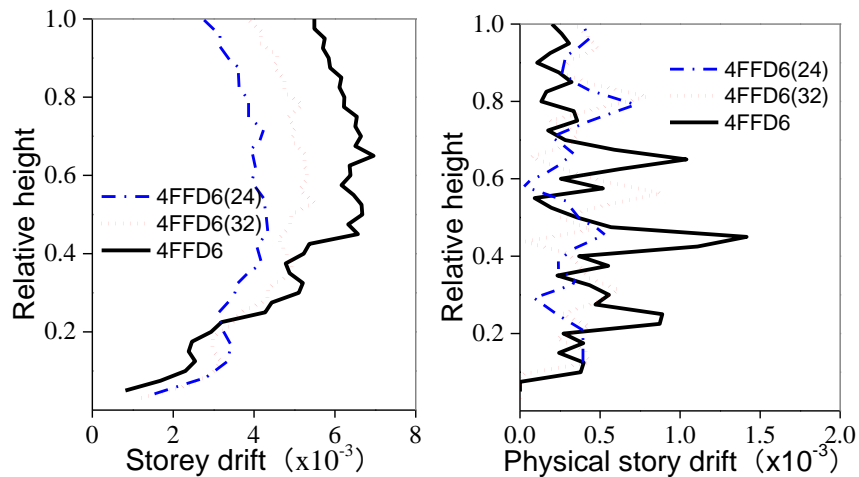


Fig.11 - Storey drift and physical storey drift under different structure aspect ratio (The structural aspect ratios of the model, 4FFD6(24), 4FFD6(32) and 4FFD6 are 2.67, 3.56 span and 4.44, respectively)

CONCLUSION

The frame-diagrid structure has obvious advantages in the structure selection. The storey drift of the structure is analyzed in detail, and we obtained the following main conclusions.

The lateral deformation formula for the high-rise frame-diagrid structures is derived. The bending deformation of the structure is divided into the bending rotational deformation and the floor rigid rotational deformation. The calculation method of the physical storey drift of the frame-diagrid structure system is obtained. The physical storey drift is directly related to the structural damage. When the structure is in the plastic state, the structure maximum storey drift and maximum physical storey drift are in different positions. It is recommended to use both storey drift and physical storey drift as structural deformation limitation criteria. The proposed method is used to structural parameters analysis for the high-rise frame-diagrid structure. The angle of the diagonal column, the cross section area of the diagonal column, the span of the main ring beam and the aspect ratio of the structure in the frame-diagrid structure have a influence on the storey drift of the structure; however, for the physical storey drift, the diagonal column angle and the diagonal column section have a great influence on it, and the main ring beam space and the structural aspect ratios have a little influence on it.

ACKNOWLEDGEMENTS

The work presented in this paper was supported by the National Natural Sciences Foundation of China (No. 51878540, 51478382).

REFERENCES

- [1] Aydin R, Gönen H. Lateral stiffness of frames and effective length of framed columns[J]. *Journal of Structural Engineering*, 1994, 120(5): 1455-1470.
- [2] Ali M M, Moon K S. Structural developments in tall buildings: current trends and future prospects[J]. *Architectural science review*, 2007, 50(3): 205-223.
- [3] Moon K S, Connor J J, Fernandez J E. Diagrid structural systems for tall buildings: characteristics and methodology for preliminary design[J]. *The Structural Design of Tall and Special Buildings*, 2007, 16(2): 205-230.
- [4] Asadi E, Adeli H. Diagrid: An innovative, sustainable, and efficient structural system[J]. *The Structural Design of Tall and Special Buildings*, 2017, 26(8): e1358.
- [5] Liu C, Li Q, Lu Z, et al. A review of the diagrid structural system for tall buildings[J]. *The Structural Design of Tall and Special Buildings*, 2018, 27(4): e1445.
- [6] Boake T M. Diagrid structures: systems, connections, details[M]. Walter de Gruyter, 2014.
- [7] Bruneau M, Uang C M, Whittaker A. Ductile design of steel structures[M]. New York: McGraw-Hill, 2011.
- [8] Naeim F. The seismic design handbook[M]. Springer Science and Business Media, 2003.
- [9] UBC 1997. Structural engineering design provisions. International conference of building officials, 1997.
- [10] IBC 2009. International building code : 2009. International Code Council, 2009.
- [11] GB50011, Code for Seismic Design of Buildings. National Standard of P. R. China, China Architecture & Building Press, Beijing, China, 2010.
- [12] JGJ 3-2010, Technical specification for concrete structures of tall building. National Standard of P. R. China, China Architecture & Building Press, Beijing, China, 2010.
- [13] Hui Z, Lianping Y, Wenxing Z. Discussion on Storey Drift Limit of SuperHigh-rise Reinforced Concrete Buildings [J]. *Journal of Building Structures*, 1999, 3: 001.
- [14] Jiang Huanjun, Hu Lingling, YING Yong. Study on Relationship Between Storey Drift and Element Deformation for RC Shear Wall Structures[J]. *Structural Engineers*, 2011, 27(6): 26-33.

- [15] Deng Mingke, Liang Xingwen, Wang Qinglin, et al. Research on calculating methods of story drift for reinforced concrete shear wall structures[J]. Journal of Earthquake Engineering and Engineering Vibration, 2008, 28(3) : 95-103.
- [16] Stafford S B, Coull A. Tall Building Structures: Analysis and Design[J]. John Wiley and Sons, 1991.
- [17] Qingxuan Shi, Feng Zhang. Simplified calculation of shear lag effect for high-rise diagrid tube structures[J]. Journal of Building Engineering, <https://doi.org/10.1016/j.jobbe.2019.01.009>.
- [18] Timoshenko, Goodier. Theory of Elasticity[M]. McGraw-Hill book Company, 1951.
- [19] CSI (2006), Perform 3D, Nonlinear Analysis and Performance Assessment for 3D Structures User Guide, Version 4, Computers and Structures Inc., Berkeley, CA.
- [20] Papachristidis A, Fragiadakis M, Papadrakakis M. A 3D fibre beam-column element with shear modelling for the inelastic analysis of steel structures[J]. Computational Mechanics, 2010, 45(6):553-572.
- [21] Applied technology council. ATC-40 Seismic evaluation and retrofit of concrete buildings. Volume 2, Appendices[M]. Seismic Safety Commission, 1996.

INFLUENCE ANALYSIS OF ROCK MECHANICAL PARAMETERS ON THE TBM PENETRATING RATE

Jin Lu¹, Xiaofan Liao²

1. *Chengdu Aeronautic Polytechnic, Department of Civil Engineering, Chengdu, China; youha917@163.com*
2. *Sichuan Electric Power Design and Consulting Co., Ltd., Chengdu, China; 47926831@qq.com*

ABSTRACT

To study the influences of rock mechanical parameters on the penetrating rate of a tunnel boring machine (TBM), a 3D discrete element model, namely, 3D distinct element code (3DEC), was used to build simulated models on rock fragments using a TBM cutter based on the geological conditions of the west route of the South-to-North Water Transfer Project. The change rule of the TBM penetrating rate caused by different rock mechanical parameters was analyzed. The line graph of the relationship between the TBM penetrating rate and rock mechanical parameters was fitted using the least squares method. Results show that the TBM penetrating rate will decrease with an increase in uniaxial compressive strength and elastic modulus. By contrast, it will increase with an increase in rock Poisson's ratio. This finding is in accordance with the result of the finished project. A numerical foundation was provided for the TBM tunneling of diversion tunnels in the west route of the South-to-North Water Transfer Project.

KEYWORDS

TBM; Penetrating rate; Rock mechanical parameters; Discrete element model; Least squares method

INTRODUCTION

The tunnel boring machine (TBM) has been widely used in domestic and overseas deep tunnels (hereafter referred to as the TBM construction method) because of its high construction efficiency, good forming construction, and impact on the safety and small operation of the surrounding environment^[1-3]. Many geological factors affect the TBM tunneling rate due to the geological conditions in front of the construction area that result in poor TBM adaptability. These factors can be mainly divided into three categories: lithology, rock hardness difference, and geological disasters^[4-5]. Rock mechanical parameters are important factors that affect the TBM tunneling rate. In recent years, numerous local and overseas scholars have analyzed factors that influence the TBM tunneling rate via geological field surveys, laboratory rock mechanical tests, and numerical simulations. Li discussed the relationship of rock uniaxial compressive strength (UCS) and hardness to the TBM penetration rate^[6]. Wang described the relationship between the tunneling rate and geological factors of tunnel excavation^[7]. Luo utilized the function fitting model to investigate the UCS and abrasion value of rocks and their correlation^[8]. Vicente et al. used the Monte Carlo-backpropagation neural network method to predict the TBM tunneling rate^[9]. Qin studied the characteristics of rock excavation using TBM when the decision problem of^[10]. He discussed the classification method for the TBM construction of tunnel surrounding rock under the condition of^[11]. However, the aforementioned studies on TBM have not conducted a systematic numerical analysis of the relationship between the TBM tunneling rate and rock mechanical

parameters. In the current study, a 3D discrete element program, namely, 3D distinct element code (3DEC), is used to simulate the rock-breaking process of a TBM hob. The influences of rock mechanical parameters on the TBM tunneling rate are also analyzed.

ROCK MECHANICAL PARAMETERS THAT AFFECT THE TBM TUNNELING RATE

Rock mechanical parameters related to the TBM tunneling rate can be expressed using indexes of rock UCS, elastic modulus, and Poisson's ratio. The tool penetration depth factor is the most important mechanical behavior of rocks under uniaxial compression conditions. A rotary tool must exert a force that is greater than the strength of rock stress to effectively cut into the rock; hence, the TBM tunneling rate and rock UCS are closely related. Existing engineering experience indicates that rock UCS is low within a certain range, and the TBM driving rate is high. When rock UCS increases, the TBM driving rate is decreased. However, when rock UCS is too low, the self-stability of the surrounding rock decreases, collapse can easily occur, and the TBM penetration rate is reduced. When TBM is driven into hard-wearing rocks, tool wear and tool circle consumption are fast, which seriously affects the TBM tunneling rate. Therefore, when rock hardness is low, the TBM tunneling rate is high; when rock hardness is high, the TBM tunneling rate is significantly reduced. However, when rock hardness is too low, the surrounding rock easily becomes unstable, which affects the TBM tunneling rate.

3D SIMULATION OF THE TBM ROCK-BREAKING PROCESS

The west route of the South-to-North Water Transfer Project, such as in the Niqu–Du Ke River water diversion line, according to the rock mechanical parameters used in the model selection of rock mechanical parameters obtained by rock test chamber, the TBM tool-breaking process simulation and analysis. The Niqu–Du Ke River water diversion line, which is located in the territories of Sichuan County in Ganzi Province and Rangtang County, is deeply buried into the long tunnel selection line of the main project. The average depth is generally 300–800 m; the maximum depth is 1190 m. The line area of the lithology of outcropping strata that are composed of Triassic metamorphic sandstone and slate, the degree of fracture development influenced by lithology, lithology, rock thickness, generally larger than sandstone slate, thin than thick layer, with an increase in depth, the degree of fracture development is weakened. In this study, the discrete element method 3DEC is used to simulate the rock-breaking process of TBM. The influence rule of rock mechanical parameters on the TBM tunneling rate is also determined.

BASIC ASSUMPTIONS IN ESTABLISHING THE 3D SIMULATION MODEL

To reasonably simulate the breaking force of TBM and the joints in a rock mass, certain parameters were assumed in the calculation of the discrete element. The joints are linear elastic materials. The rock materials did not swell when the surrounding rock was subjected to shear action. The cutter head and the cutter were assumed as linear elastic materials. An excavation area of 100 m x 100 m x 100 m was selected according to the influence of TBM excavation. To analyze the rock-breaking process of the TBM cutter, a smaller model (10 m x 10 m x 10 m) was used within the tunnel excavation scope. Figure 1 shows a 3D simulation of the TBM tunnel excavation model.

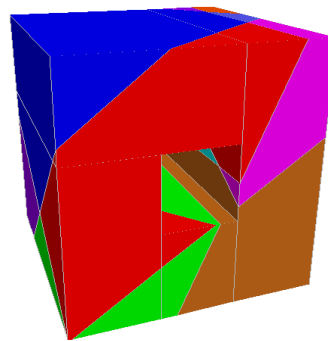


Fig. 1 - 3D simulation model of tunnel excavation using TBM

SELECTION OF ROCK MECHANICAL PARAMETERS

A total of 15 groups of rock mechanical parameters were selected from the experiment (Table 1). The joint spacing was assumed as 30 mm, with a joint and tunneling direction angle of 60°. The 3D simulation model of the TBM cutter rock-breaking process was established, which modified the rock mechanical parameters in the model for discrete element calculation and analysis.

Tab. 1 - Selected rock mechanical parameters

Group	Rock UCS/MPa	Elastic modulus/GPa	Poisson's ratio
1	31.5	13.3	0.51
2	33.1	15.7	0.46
3	43.6	23.6	0.45
4	45.7	30.1	0.43
5	51.6	35.3	0.38
6	55.7	39.1	0.35
7	58.3	41.2	0.29
8	67.3	43.5	0.26
9	78.5	46.5	0.22
10	92.7	47.5	0.21
11	101.5	49.3	0.21
12	105.6	51.2	0.18
13	107.1	60.3	0.16
14	111.3	71.8	0.16
15	117.0	84.1	0.15

Calculation formula for drilling rate:

$$V = 60Pn/1000 \quad (1)$$

$$T = 1800/Pn \quad (2)$$

$$N = 9000 \quad (3)$$

$$\omega = 4.5 \quad (4)$$

$$d = 4.53 \quad (5)$$

where V denotes the drilling rate, m/h; P indicates penetration, mm/r; n signifies the rotation rate of the cutter head, r/min; T is the drilling time of each route, mm/min; N is pressure at face, kN; ω is the rotation rate of the cutterhead, r/min; d is the cutterhead diameter, m.

The difference in TBM penetration into rock depth under varying joint directions is obtained according to 3D simulation. The TBM tunnelling rate under different rock mechanical parameters is calculated using the formula.

Some of the 3DEC codes in the 3D simulation model of TBM penetration are as follows.

```
new
poly brick -35,35 -35,35 -50,50
jset dd 270 dip 60 origin 0.3,0,0
jset dd 230 dip 30 oorigin 0,0,-0.3
jset dd 320 dip 15 origin 0,0,0.3
plot hold dip 70 dd 200 color mat
ret
tunnel a (-16.3,-16.3,-30.5) (-16.3,16.3,-30.5) (16.3,16.3,-30.5) (16.3,-16.3,-30.5) &
      b (-16.3,-16.3,30.5) (-16.3,16.3,30.5) (16.3,16.3,30.5) (16.3,-16.3,30.5)
remove -16.3,16.3 -16.3,16.3 -30.5,30.5
plot hold dip 70 dd 200 color mat
plot hold exc joint
ret
gen edge 1.0
prop mat=1 dens 2630 bulk 1.5e7 g 0.7e8
prop mat=2 dens 2760 bulk 1.5e7 g 0.2e8
prop jmat=1 kn 1e9 ks 1e9 coh 1e9 ten 1e9
ret
bound -10,10 60,30 -10,10 stress 0.0 -1e6,0.0 0,0,0
bound -10,-60 -10,10 -10,10 xvel 0.0
bound 60,30 -10,10 -10,10 xvel 0.0
bound -10,-60 -10,10 -10,10 zvel 0.0
bound -10,-60 -10,10 60,30 zvel 0.0
bound -10,-60 -60,-30 -10,10 yvel 0.0
grav 0,-10,0
insitu stress -0.5e6 -1.5e6 -0.5e6 0 0 0
ret
hist unbal
hist ydis 30,30,0
hist ty 1
step 500
save tun0.sav
ret
rest tun0.sav
```

ANALYSIS OF THE RELATIONSHIP BETWEEN ROCK MECHANICAL PARAMETERS AND THE TBM TUNNELING RATE

Rock mechanical parameters that affect the TBM tunnelling rate include rock UCS, elastic modulus, and Poisson's ratio. Within a certain range, when rock UCS is low, the TBM tunnelling rate is high; when rock UCS is high, the TBM tunnelling rate is low. However, when rock UCS is too low, the self-stability of the surrounding rock decreases, collapse can easily occur, and the TBM tunnelling rate is reduced. When TBM is driving into hard-wearing rocks, tool wear and tool circle consumption are fast, which seriously affects the TBM tunnelling rate. Therefore, when rock hardness is low, the TBM tunnelling rate is high; when rock hardness is high, the TBM tunnelling rate is low. However, when rock hardness is too low, the surrounding rock easily becomes unstable, which affects the TBM tunnelling rate. Table 2 presents the change in the TBM tunnelling rate with the rock mechanical parameters when the joint condition in the rock mass obtained by the 3D simulation calculation is constant. Figure 2 shows the relationship of the TBM tunnelling rate to rock UCS, elastic modulus, and Poisson's ratio.

Tab. 2 - Excavation rate of TBM change with rock mechanical parameters

TBM drilling rate/(m/h)	Triaxial compressive strength/MPa	Elastic modulus/GPa	Poisson's ratio
2.43	33.1	15.7	0.46
2.36	43.6	23.6	0.45
2.11	45.7	30.1	0.43
2.12	51.6	35.3	0.38
2.09	55.7	39.1	0.35
1.83	58.3	41.2	0.29
1.81	67.3	43.5	0.26
1.71	78.5	46.5	0.22
1.56	92.7	47.5	0.21
1.13	101.5	49.3	0.21
0.91	105.6	51.2	0.18
0.91	107.1	60.3	0.16
0.73	111.3	71.8	0.16
0.63	117	84.1	0.15

As shown in the Figure 2 to Figure 4, the TBM tunnelling rate decreases with an increase in rock UCS and elastic modulus within a certain range and increases with an increase in rock Poisson's ratio. The curves in Figures 2 and 3 are similar to the straight line with a negative slope, whereas the curve in Figure 4 is similar to the straight line with a positive slope. Therefore, the least squares method can be used to synthesize the three curves.

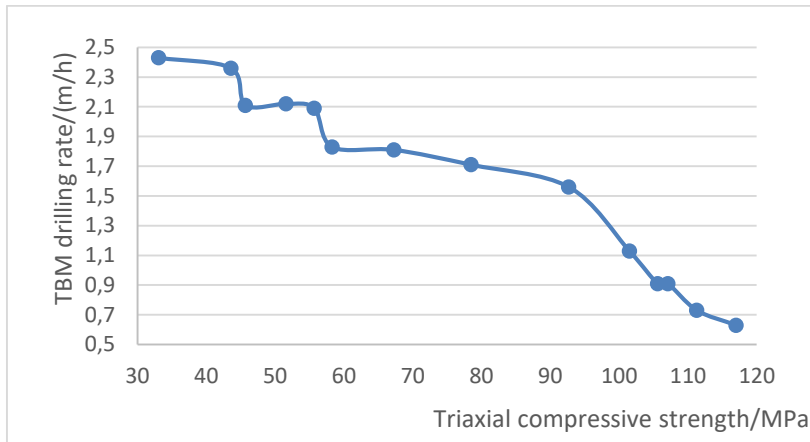


Fig. 2 - Relation diagram between the TBM driving rate and Triaxial compressive strength

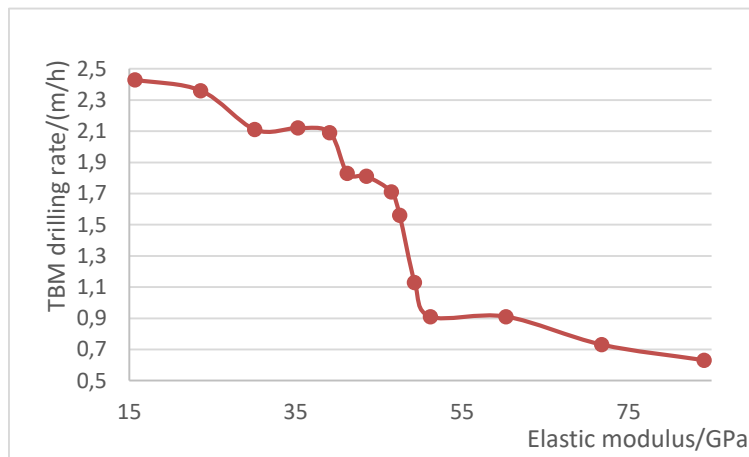


Fig. 3 - Relation diagram between the TBM driving rate and Elastic modulus

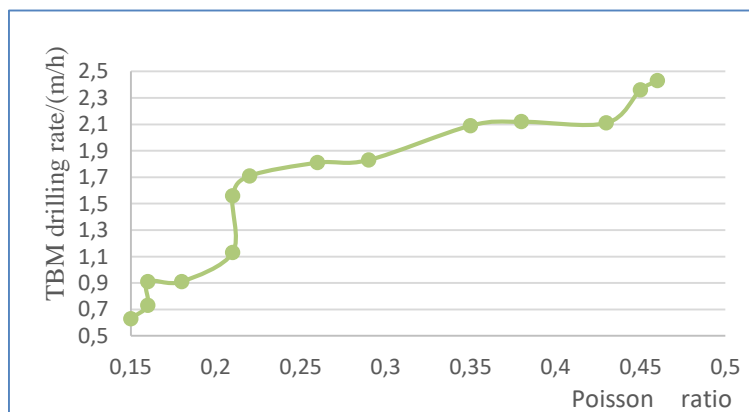


Fig. 4 - Relation diagram between the TBM driving rate and Poisson's ratio

CONCLUSION

In the construction example of the west route of the South-to-North Water Transfer Project, the 3D discrete element method was used to simulate the rock-breaking process of a TBM hob, and the influences of rock mechanical parameters on the driving speed of TBM was analyzed. The following conclusions were obtained. The physical and mechanical properties of the surrounding rock in the tunnel influence the driving speed of the TBM. When the strength of the surrounding rock is low, the driving speed of TBM is high. When the strength of the surrounding rock is high, TBM tunnelling will experience difficulties, and driving speed will be reduced. The linear map of the relationship between the TBM driving rate and the rock mechanical parameters fitted using the least squares method is similar to the data obtained using the existing TBM construction monitoring method. Therefore, the analysis in this study can play a guiding role in the construction of the west route of the South-to-North Water Transfer Project.

REFERENCES

- [1] Science and Technology Extension Center of the Ministry of water resources. Tunnel Boring Machine[M]. Beijing. Petroleum Industry Press. 2005:1-2.
- [2] Mengshu Wang, Dianhuang Li. Construction and engineering example of rock tunnel boring machine[M]. China Railway Press. 2015:131-132.
- [3] Jinying Qu. The present situation and future development of TBM tunnel construction[J]. Tunnel construction. 2002, 22(4): 60-63.
- [4] Qiu ming GONG, Jian ZHAO, Yu-yong JIAO. Numerical modeling of the effects of joint orientation on rock fragmentation by TBM cutters[J]. Tunneling and Underground Space Technology, 2005, (20):183 – 191.
- [5] Lijun Su, Jinshan sun. Numerical simulation of rock breaking process of TBM based on particle flow model[J]. Geotechnical Mechanics. 2016, 20(9) : 2823-2829.
- [6] Weibing Li, Bin Liu. Analysis of geological factors affecting the selection of TBM[J]. Hydroelectric Power Generation. 2009, 35(8) : 25-27.
- [7] Faliang He, Shichun Wang. Research and development of classification method for surrounding rock of railway tunnel[J]. Journal of Railway Engineering Society. 2015 : 392-397.
- [8] Hua Luo, Tao Feng. Correlation analysis between rock abrasion resistance and rock strength based on TBM construction[J]. Geotechnical engineering. 2008, 28(1) : 104-105.
- [9] Sen Wen, Yanxi Zhao. Prediction of TBM driving speed based on Monte Carlo-BP neural network[J]. Geotechnical Mechanics. 2009, 30(10) : 3127-3132.
- [10] Songjun Qin. Determination of rock characteristics during tunneling of tunnel boring machine[J]. 2016, (8) : 2-4.
- [11] Faliang He, Shichun Wang. Research and development of classification method for surrounding rock of railway tunnel[J]. Journal of Railway Engineering. 2005, 12 : 392-397.

RESTRICTED ZONE OF SUPERPAVE MIX DESIGN AND ITS IMPACT ON RESILIENT MODULUS AND PERMANENT DEFORMATION

Arshad Hussain, Fazal Haq, Nauman Javaid and Muhammad Bilal Khurshid

Department of Transportation, National Institute of Transportation, National University of Sciences and Technology, Islamabad, Pakistan; emails: drarshad@nit.nust.edu.pk; fhaq.tn15@nit.nust.edu.pk; nauman.javaid@nit.nust.edu.pk; bilal-nit@nust.edu.pk

ABSTRACT

Back in 1993, Strategic Highway Research Program introduced new mix design method known as SUPERPAVE that is an acronym of Superior Performing Asphalt Pavement. Superpave caters field performance of bituminous mixes and Superpave gradation chart includes 0.45 power line, restricted zone and control points. In Superpave, the gradation that compliance with the restricted zone was considered less rut resistant as compared to gradation passing outside the restricted zone. This study targets three types of gradations that passed above, below and through the restricted zone. The results show that the gradation passing through the restricted zone not only satisfy Superpave volumetric requirements but also performs better against rutting as compared to gradation passing outside the restricted zone. Resilient modulus (M_R) measured through indirect tensile strength setup that defines the elastic properties of bituminous mix under repeated load test. Laboratory study was conducted to find factors that affect the gradation. Two-way factorial design was carried out by using Minitab-15 statistical software and the results reflected that the individual factor i.e. loads duration and temperature as well as interaction of factors has significant effect on the performance of HMA.

KEYWORDS

Resilient Modulus; Permanent Deformation; Hot Mix Asphalt (HMA); Restricted Zone; Superpave

INTRODUCTION

Asphalt concrete is composed of binder and aggregate. In asphalt pavement 94% to 95% is aggregate whereas remaining portion is binder that acts as gluing agent. In hot mix asphalt the aggregate provides strong aggregate skeleton to resist each application of load. When load is applied the rough and angular aggregates tightly lock with each other and offer a single elastic mass with larger size thus enhancing the shear strength of asphalt mixtures. Therefore, gradation is an influential characteristic of aggregate that affects the performance of HMA like fatigue cracking and permanent deformation. Mixes having different gradation have different stability and rutting potential. To encounter permanent deformation issues SHRP introduced new mix design method named as SUPERPAVE and specifications for aggregate gradation chart. The gradation chart has maximum density line, control points and restricted

zone. Maximum density line splits coarse gradation with finer one, control point serves as master range through which gradation must pass whereas the restricted zone restricts the gradation to pass through the restricted zone. In this study three gradations passing Above the Restricted Zone (ARZ), Below the Restricted Zone (BRZ) and Through the Restricted Zone (TRZ) are considered.

Resilient modulus test is carried out on laboratory fabricated specimen by employing repeated load indirect tension test according to ASTM standard D4123. The test is performed on cylindrical specimen that is subjected to compressive loads and the results are shown in haversine or triangular waveform. The recoverable horizontal deformation of each cylindrical specimen is measured with assumed poisson's ratio and resilient modulus is calculated. Resilient modulus M_R is defined as ratio of applied deviator stress to recoverable strain as shown in below Equation 1.

$$M_R = \frac{\sigma_d}{\varepsilon_r} \quad (1)$$

where, σ_d is defined as deviator stress i.e. vertical or axial stress whereas ε_r is defined as recoverable strain. Small portion of deformation may be recoverable or resilient whereas remainder will be plastic or unrecoverable. Large amount of plastic strains are present at initial stage of test whereas plastic strain starts to diminish as load increases under the action of repeated load test. It is said that after 100 to 200 load cycles of repetition, the strain is mostly recoverable [1].

Three gradation band (upper gradation band, lower gradation band and middle gradation band) of one NMAS (19mm) was selected to find the rutting potential of the HMA mixtures. It can be determined that the gradation of aggregate plays significant role in rutting propensity and this fact proves that structure of aggregate is the main load carrying factor of bituminous mixes. The skeleton provided by middle gradation in mixture has the lowest deformation and its resilient modulus value is the highest whereas the skeleton provided by mixture with lower gradation showed highest deformation and the lowest resilient modulus value [2].

Two wearing and one base asphalt concrete mixtures were taken (ACW14, ACW20 and ACB28), resilient modulus was analysed by varying bitumen content by interval of 0.5% and at two different temperatures. With the increasing bitumen content and temperature, resilient modulus decreased because strength of the mixture reduces with the increase in bitumen content. On the other hand higher grading (ACB 28) give higher resilient modulus [3].

Effect of resilient modulus on specimen thickness, diameter and aggregate NMAS and three loading factor including load, waveform and strain level was computed. It was believed that resilient modulus decreases as load duration increases because plastic strain becomes higher [4].

Indirect tensile strength, dynamic modulus, uniaxial creep and flexural fatigue test are carried out for surface mix 9.5mm and base mix 25.0 mm and results were analysed at different temperatures. The results derived show that increase in temperature decreases the resilient modulus and IDT strength of 9.5mm surface are higher than 25.0mm base mix [5].

Another literature review of thirteen published papers to study the SUPERPAVE restricted zone and its impact on the performance of aggregate gradation was carried out. The literature review included extensive range of aggregates, gradations, NMAS, and performance testing. The results obtained by reviewing the papers are that the gradations passing TRZ

perform better as compared to gradation passing outside the restricted zone. It is indicated clearly by the reviewed research that mixtures with fine graded gradations which either passes above the restricted zone or that passes through the restricted zone perform the best and thus these gradations perform better than mixtures with gradations that passes below the restricted zone. The recommendations obtained suggested that the concept of restricted zone should be eliminated from the specifications of Superpave because several research pointed that satisfactory results could be achieved with gradations ranging from BRZ to ARZ and no interaction were seen between the fatigue and rutting performance of hot mix asphalt and the restricted zone of Superpave mix design [6].

Hot mix asphalt designed by superpave mix design procedure with gradation passes ARZ typically showed least amount of rutting unlikely for mixtures with gradation passes BRZ which typically showed high level of rutting [7].

For limestone and granite, asphalt wearing course mix with gradation passing below the restricted zone typically showed the lowest rut resistance, mixes with gradation passing through the restricted zone typically showed the highest rut resistance, and mixes with gradation passing above the restricted zone typically showed an intermediate rut resistance. While for gravel mixtures with gradations passing below the restricted zone typically showed the highest rut resistance, gradation passing above the restricted zone typically showed the lowest rut resistance, and mixtures with gradation passing through the restricted zone typically showed an intermediate rut resistance. [8].

It is confirmed that in the theory of SHRP – Superpave the volumetric and composition correlate up to some extent i.e. mixes with gradation passing TRZ may have higher value of voids filled with asphalt and lower value of void in mineral aggregate. Mixes containing gradation passes TRZ cannot be characterized with worst mechanical properties [9].

Mixes having gradations passes TRZ will give results somewhat comparable or even better than the mixes with gradations that pass either ARZ or BRZ. This result was concluded from the experiments conducted on mixes with gradations having maximum aggregate size of 12.5 mm, 19 mm and 25 mm applying gyrations of 50, 70 and 100 at N design value. Also the mixtures having aggregate gradations passes BRZ appears to be more affected by aggregate properties than that of the mixes with gradations passes either TRZ or ARZ [10].

The asphalt mixtures with gradations passes TRZ, Hump through the restricted zone and Crossover through the restricted zone with the three Nominal Maximum Aggregate Size of (9.5, 12.5, and 19.0 mm) were resulted with higher value of air voids than the asphalt mixes with aggregate gradation passes ARZ and BRZ, and hence could be more susceptible to rutting [11].

RESEARCH METHODOLOGY

Aggregates were procured from Margalla quarry site whereas the 60/70 grade binder was procured from Attock Oil Refinery. Sieve analysis was done and aggregates were stored in respective bins. Aggregates were then procured from respective bins to achieve the required gradation blend. Optimum bitumen was calculated for each gradation blend (ARZ, TRZ and BRZ) by compacting the specimen in Superpave gyratory compactor (SGC). The resilient modulus of each gradation was carried by UTM-25 at two different temperatures (25 °C and 40 °C) according to ASTM standard D4123 and conclusions were drawn for the ARZ, TRZ and BRZ.

Mixtures Description

Superpave gradation consists of 0.45 power line enveloped by control points and restricted zone. Control points define the maximum and nominal maximum aggregate size as well as the dust proportion. On the other hand restricted zone restricts the gradation that passed TRZ because it was believed that the gradation passes TRZ will produce the tender mix. This study is based on three Superpave gradations that are named as ARZ, BRZ and TRZ. Figure 1 shows the 19.0mm NMAS Superpave gradation blend (ARZ, TRZ and BRZ).

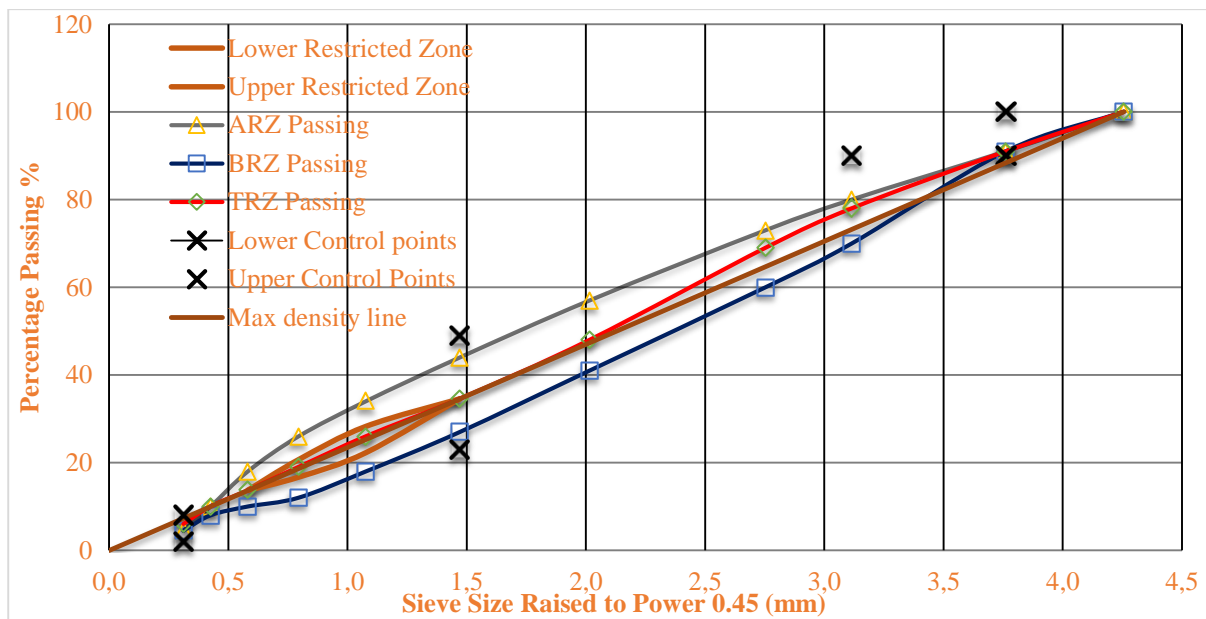


Fig. 1 – Gradation Chart with 19.0mm NMAS

Asphalt Mixtures Preparation

Three gradations (ARZ, TRZ and BRZ) of 19.0mm NMAS were prepared in laboratory by using Superpave design method. The specimens were compacted by employing SGC that compacts each gradation at 125 numbers of gyrations. The optimum bitumen content and volumetric was determined for each gradation as shown in below Table 1.

Tab.1 - Volumetric of Superpave Gradations

Gradation	% VMA	%G _{mm} @ N _{ini}	Design P _b %	Design P _{be} %	P ₂₀₀ /P _{be}
TRZ	13.21	85.60	4.00	3.97	1.13
BRZ	13.48	84.20	4.20	4.10	1.46
ARZ	13.40	87.90	4.30	3.82	1.17

- VMA= Voids in Minerals Aggregate
- G_{mm} = maximum specific gravity of paving mixture (no air voids)
- P_b = Asphalt, percent by total weight of mixture
- P_{be}= Percent Effective Bitumen
- P₂₀₀ = Aggregate content passing the 0.075-mm sieve, the percent by mass of aggregate.

All the specimens were processed through core cutting for the diameter of 100 mm. Saw cutting was performed to cut samples with height of 50 mm and 100 mm in diameter. Figure 2 shows sample for IDT and Resilient Modulus Tests whereas Figure 3 shows the specimen for wheel tracker test.



Fig. 2 – Specimens for IDT and MR Tests



Fig. 3 - Specimens for HWT Test

Input Parameters

Following Input parameters were selected as shown in Table 2 and fed into the testing software and specimens were subjected to Resilient Modulus test as per ASTM D4123:

Tab.2 - Input parameters

Parameters	Selected Values
Peak Loading Force	20% of IDT strength
Searing Force	10% of Peak Loading Force
Poisson's Ratio (assumed)	0.4
Conditioning Pulses	100
M _R Data Collection Pulses	5
Temperature	25 and 40 Degree C
Loading Duration	100 and 300 ms

RESULTS AND DISCUSSIONS

The tests were conducted on the prepared samples using the input parameters as defined. Since tests were performed on two temperatures and two loading durations, plots were plotted for ARZ, TRZ and BRZ as shown in below Figure 4 and 5.

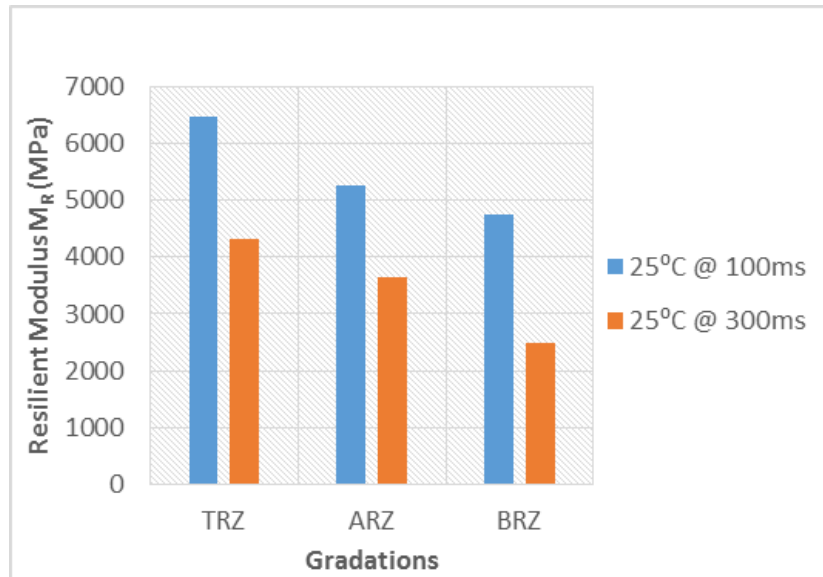


Fig. 4 – Resilient Modulus of Gradation at 25 °C

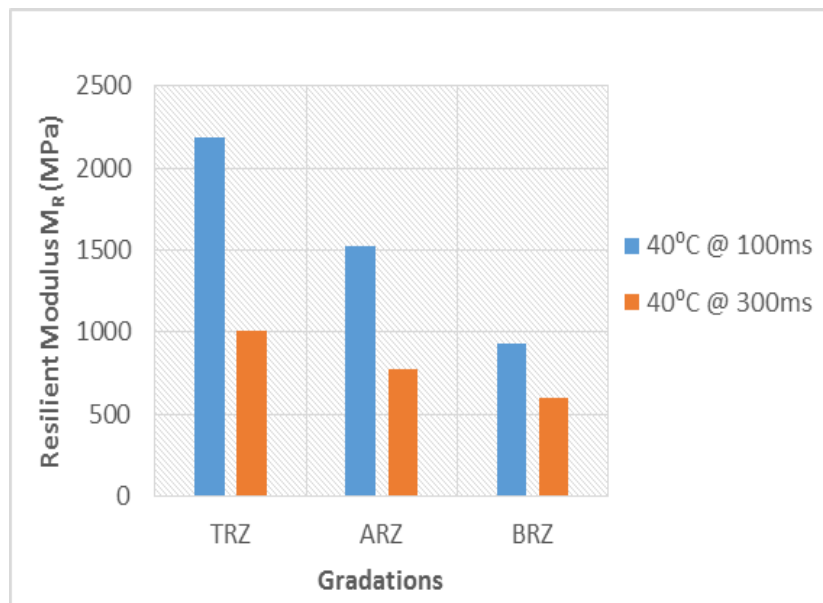


Fig. 5 – Resilient Modulus of Gradation at 40 °C

Figure 6 shows the effect of gradation on rutting. Gradation passing BRZ has marginally higher rut depth as compared to gradation passing ARZ and TRZ. Gradation passing TRZ that was considered as rut prone performs best as compare to rest of gradations.

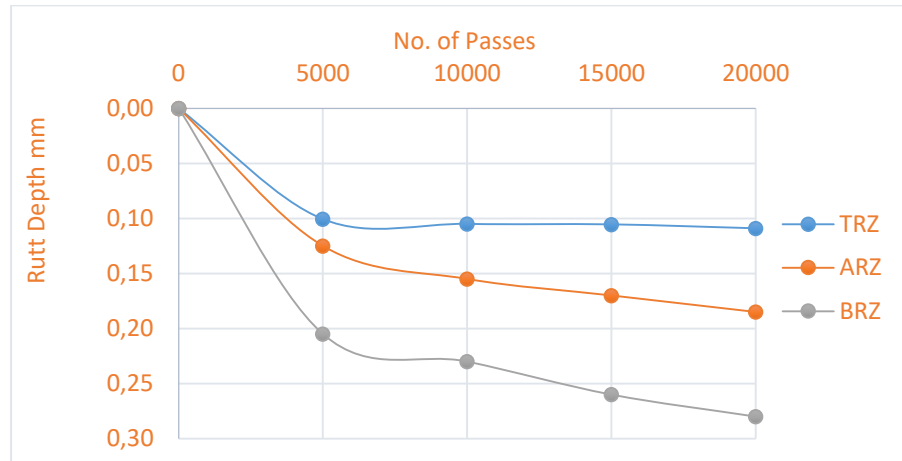


Fig. 6 - Gradation effect on Rut Depth

Analysis of rut depth was evaluated by conducting one way ANOVA. Table 3 shows the ANOVA conducted on HWT test results. Which clarify that the gradation has significant effect on rutting propensity.

Tab. 3 - Analysis of Variance of Rut Depth

Source	DF	SS	MS	F	P
Gradation	2	0.029108	0.014554	205.47	0.001
Error	3	0.000212	0.000071		
Total	5	0.029321			

Analysis of Resilient Modulus Test Results

In this research, two factors were considered and are presented in Table 4 with their respective abbreviations including high and low levels. Design of experiments was carried out using Minitab-15 statistical software separately for ARZ, TRZ and BRZ.

Tab. 4 - Factors for ARZ, TRZ and BRZ

Acronyms	Factors	Levels	Units
A	Temperature	100 and 300	ms
B	Load Duration	25 and 40	°C

In Analysis of Variance ANOVA, three F-tests are made and level of significance (α) was chosen to be 0.05. To evaluate these five tests, the probability results are given as shown in Table 5, 6 and 7.

Tab.4 - Analysis of Variance for ARZ

Source	DF	Sequential Sum of Squares	Adjusted Sum of Squares	Adjusted Mean Squares	F-Test	P-Test	Significance at 95%
Main Effects	2	36696327	36696327	18348163	880.47	0.000	Yes
2-Way Interactions	1	563767	563767	563767	27.05	0.001	Yes
Residual Error	8	166713	166713	20839			
Pure Error	8	166713	166713	20839			
Total	11	37426807					

Tab.5 - Analysis of Variance for TRZ

Source	DF	Sequential Sum of Squares	Adjusted Sum of Squares	Adjusted Mean Squares	F-Test	P-Test	Significance at 95%
Main Effects	2	51458190	51458190	25729095	1189.71	0.000	Yes
2-Way Interactions	1	672133	672133	672133	31.08	0.001	Yes
Residual Error	8	173011	173011	21626			
Pure Error	8	173011	173011	21626			
Total	19	52303334					

Tab.6 - Analysis of Variance for BRZ

Source	DF	Sequential Sum of Squares	Adjusted Sum of Squares	Adjusted Mean Squares	F-Test	P-Test	Significance at 95%
Main Effects	2	29551222	29551222	14775611	14831.23	0.000	Yes
2-Way Interactions	1	2818821	2818821	2818821	2829.43	0.000	Yes
Residual Error	8	7970	7970	996			
Pure Error	8	7970	7970	996			
Total	11	32378013					

Interactions

The hypothesis that is carried out by Minitab-15 software has its inherently capability to carry out interaction as explained below:

Null Hypothesis: H_0 = Interactions are Insignificant

Alternative Hypothesis: H_a = Interactions are Significant

According to results displayed in tables above, the 2-way interactions have P-test value less than level of significance (LOS; $\alpha=0.05$), so we concluded that reject the null hypothesis in the favour of alternative hypothesis. So, two way interactions are statistically significant.

Significant Effects and Interaction Plots

The factors and interactions of factors affecting the resilient modulus of asphalt concrete specimen are shown in Pereto Chart of Standardized effect by using Minitab-15 Statistical Software. Pareto plot shows the absolute values of effect whereas reference line drawn shows t-distribution. The result drawn from the plot shows that individual factors and interactions of the factors are significant for all the three gradation shown in Figure 5, 6 and 7.

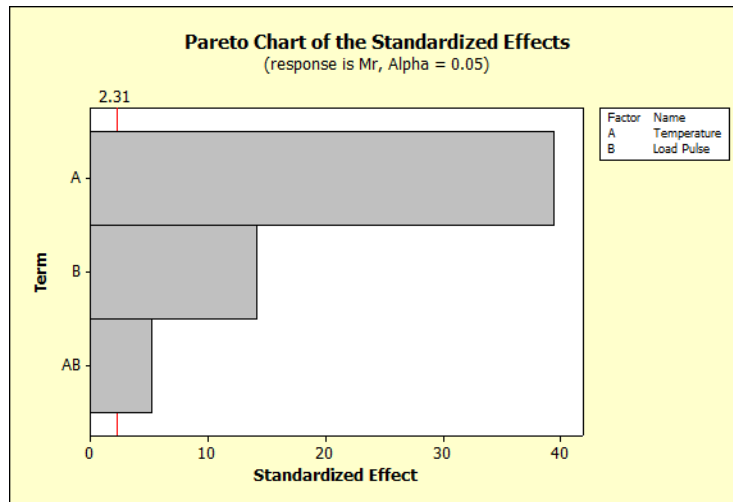


Fig. 5 – Pareto Chart for TRZ

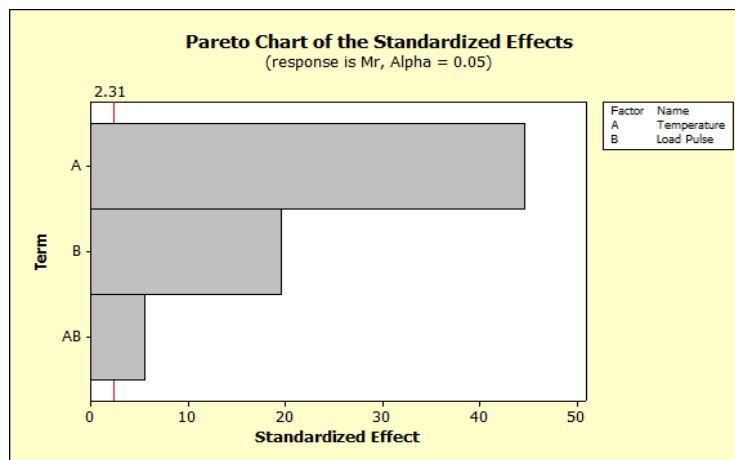


Fig. 6 – Pareto Chart for ARZ

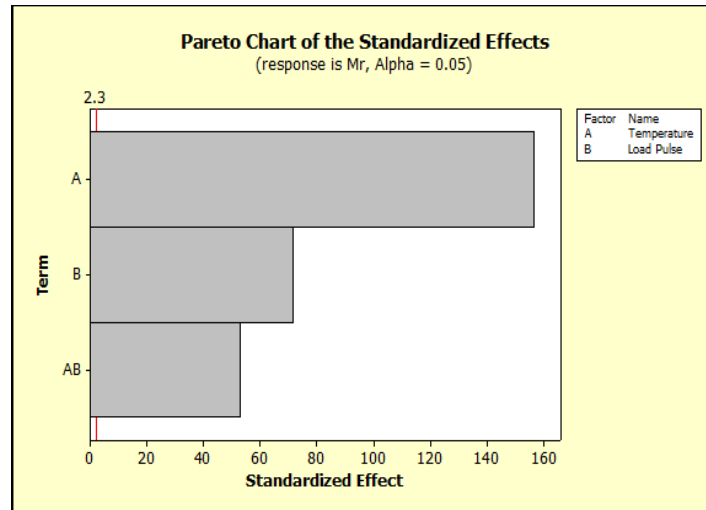


Fig. 7 – Pareto Chart for BRZ

Factorial Plots

The significant effect and the interaction obtained through Pareto will be discussed with the help of factorial plots. The individual factors are shown with main effect plots whereas two way interactions are explained through interaction matrix.

Main Effect Plots:

Main effect plots of ARZ, TRZ and BRZ are shown in Figure 8 below.

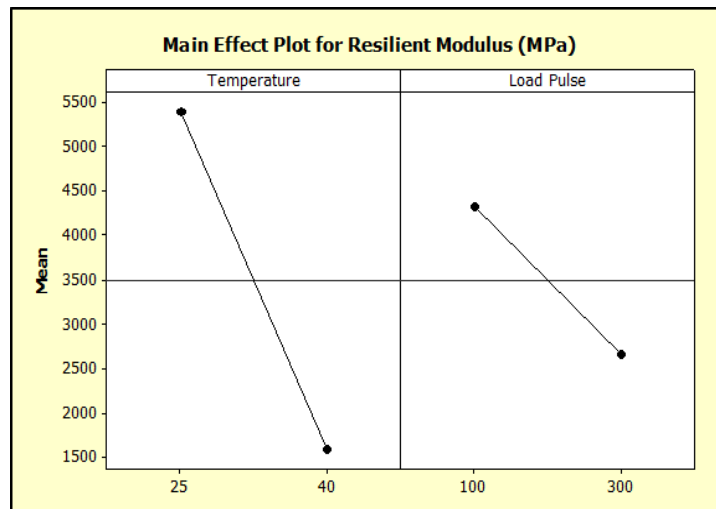


Fig. 8 – Main Effect plot for ARZ, TRZ and BRZ

The conclusion derived from the temperatures plot is that the M_r value of the asphalt concrete specimen is decreased with the increase of the temperatures from 25 °C to 40 °C. The decrease in resilient modulus is due to softening of asphalt concrete that in return reduces the stiffness of the specimen and increasing the recoverable strains and results in the reduction of M_r .

The inference drawn from the load duration plot shows that longer load duration lowers the resilient modulus for ARZ, TRZ and BRZ. This was obvious because due to longer load duration asphaltic concrete specimen experiences higher strain for long period of time and in return reduces the M_r . Reduction in resilient modulus at longer load duration can be explained by the viscoelastic nature of asphalt concrete. It can be concluded that slow moving traffic has more adverse effect on pavement surface resulting in permanent deformation of pavement.

Interaction Plots

Figure 9 presents the interaction plot of different factors (load durations and temperatures) on ARZ, TRZ and BRZ.

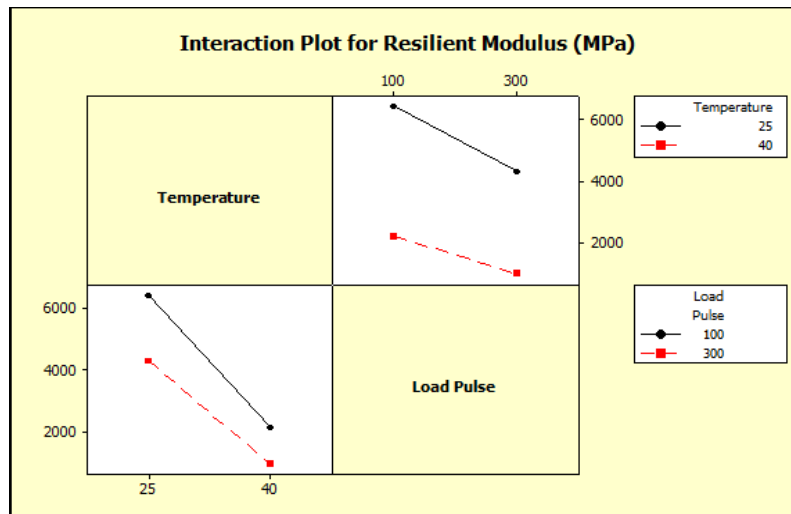


Fig. 9 – Interaction plot for ARZ, TRZ and BRZ

The conclusions derived from the interactions plots of ARZ, TRZ and BRZ are described below.

The interaction of Temperature and Load pulse vs. resilient modulus of the mixtures shows that at low temperature and smaller loading duration resilient modulus is higher whereas at high temperature and longer duration resilient modulus decreases. This is due to the reason when load is applied for smaller duration (due to slow moving traffic or static loaded traffic) at low temperature, asphaltic concrete mixture behave stiffer and the pavement surface is less prone to rutting. This HMA specimen is having high resilient modulus. But when a load is applied for longer duration and at high temperatures the scenario is totally different. The asphaltic concrete specimen becomes less stiff at higher temperature and results in lower resilient modulus.

SUMMARY AND CONCLUSION

Factorial Design was conducted to find the effect of the variable that influences the resilient modulus. The important aspect of factorial design was testing the existence of interaction among the factors. Loading Duration and temperature effect was found to be the most effectual factor on resilient modulus of asphaltic concrete. Loading pulse has significant effect on ARZ, TRZ and BRZ. Increasing the loading duration from 100 ms to 300 ms results in decrease of resilient modulus on average for ARZ, TRZ and BRZ. The decrease in resilient modulus is due to the fact that specimens experienced strains for longer period of time. Temperature has pronounced effect on ARZ, TRZ and BRZ. Increasing temperature from 25 °C to 40 °C decrease the resilient modulus significantly. The drop down in resilient modulus emphasized on the fact that asphalt concrete is temperature dependent. At higher temperature asphalt becomes viscous and aggregates contribution becomes more significant. Two ways interaction results obtained through statistical analysis depicts that resilient modulus of ARZ, TRZ and BRZ are sensitive to load pulse and temperature interactions. It can be easily stated from the performance testing results that TRZ that was considered as rut prone performs better as compared to gradation that are passing ARZ and BRZ and ANOVA conducted on HWT test results clarify that the gradation has significant effect on rutting propensity.

REFERENCES

- [1] Mallick RB, El-Korchi T. Pavement engineering: principles and practice. CRC Press; 2017 Oct 16.
- [2] Golalipour A, Jamshidi E, Niazi Y, Afsharikia Z, Khadem M. Effect of aggregate gradation on rutting of asphalt pavements. *Procedia-Social and Behavioral Sciences*. 2012 Oct 3;53:440-9.
- [3] Puzi A, Azura M, Hassan T, Rafidah TN. The effect of state factors on resilient modulus of bituminous mixture.
- [4] Ghaffarpour Jahromi S, Khodaii A. Investigation of variables affecting resilient modulus in asphalt mixes. In *Road Pavement Material Characterization and Rehabilitation: Selected Papers from the 2009 GeoHunan International Conference 2009* (pp. 56-64).
- [5] Flintsch GW, Al-Qadi IL, Loulizi A, Mokarem DW. Laboratory tests for hot-mix asphalt characterization in Virginia. Virginia Center for Transportation Innovation and Research; 2005 Jun 1.
- [6] Hand, A., & Epps, A. (2001). Impact of gradation relative to Superpave restricted zone on hot-mix asphalt performance. *Transportation Research Record: Journal of the Transportation Research Board*, (1767), 158-166.
- [7] Chowdhury A, Button JW, Grau JD. Effects of Superpave restricted zone on permanent deformation. 2001.
- [8] Kandhal PS, Mallick RB. Effect of mix gradation on rutting potential of dense-graded asphalt mixtures. *Transportation Research Record*. 2001;1767(1):146-51.
- [9] Praticò FG. A theoretical and experimental Study of the effects on mixes added with RAP caused by Superpave restricted zone violation. *Road materials and pavement design*. 2004 Jan 1;5(1):73-91.
- [10] Zhang J, Cooley Jr L, Hurley G, Parker F. Effect of Superpave defined restricted zone on hot-mix asphalt performance. *Transportation Research Record: Journal of the Transportation Research Board*. 2004 Jan 1(1891):103-11.
- [11] Al-Khateeb GG, Ghuzlan KA, Al-Barqawi MO. Effect of Superpave restricted zone on volumetric and compaction properties of asphalt mixtures. *International Journal of Pavement Research and Technology*. 2017 Nov 1;10(6):488-96.

INFLUENCE OF STRAINING BEAMS ON THE SEISMIC FRAGILITY OF DOUBLE-COLUMN BRIDGE PIERS

Yuye Zhang, Feng Xiao and Jahangir Badar

*Department of Civil Engineering, Nanjing University of Science and Technology,
Nanjing 210094, China; zyy@njust.edu.cn*

ABSTRACT

The piers of girder bridges have a very important role on the safety of the structural system to earthquakes. This paper addresses the seismic fragility of double-column (DC) bridge piers by focusing on the influence of the straining beams and the direction of seismic waves. The seismic capacity of eight DC piers with different number and position of straining beams is first studied by pushover analyses. These results are used to derive empirical formulas for the seismic capacity of general DC piers and to define damage indices for prescriptive damage states. Finite element models of typical girder bridges with the different piers are carried out next to assess the seismic demand of these piers and to generate fragility curves by comparing their seismic demand and damage indices at the defined damage states. Results indicate that: (1) DC piers are more vulnerable when subjected to longitudinal ground motions compared with the case of transverse inputs; (2) the damage probability of the piers for transverse seismic inputs decreases with the increasing relative height of the straining beams; and (3) DC piers with two straining beams have enhanced performance in the transverse direction compared with those with a single straining beam.

KEYWORDS

Girder bridges; Double-column piers; Straining beams; Seismic fragility; Damage index

INTRODUCTION

Bridge structures are particularly vulnerable to damage under earthquakes and this may be responsible for significant human and economic losses [1-3]. Since the piers are one of the most susceptible components in girder bridges [4,5], the development of predictive models and design methods to account for their seismic performance is of great interest. In this paper, focus is given to the influence of the straining beams on the widely used double-column (DC) piers.

Seismic fragility analysis is an effective method available to estimate the damage level and damage probability of a bridge when subjected to potential ground motions [6,7]. The empirical fragility method is based on actual damage data from previous earthquakes [8,9], although it may not be appropriate to estimate the damage probability for specific bridge structures [10,11]. Analytical fragility curves for bridge structures where the variation of ground motions is considered as input in numerical simulations were developed for this purpose [12-14]. This method was used in recent research on bridge components and structures [15-17], and is a very promising method for assessing the seismic fragility of DC piers, particularly under transverse ground motions.

For DC piers there are significant differences on the plastic hinge mechanism that develops under longitudinal and transverse ground motions. The seismic fragility analysis is also more evolved if considering the influence of the straining beams. This paper therefore presents an evaluation method that can be used to assess the structural safety of DC piers under earthquakes

and the contribution of the straining beams to their seismic vulnerability. A typical girder bridge is selected for analysis by varying both number and position of the straining beams. The influence of the beams on the seismic fragility of the DC piers subjected to transverse seismic waves is investigated using a simplified method based on a displacement failure criterion. The damage indices for the DC piers are obtained for each seismic input direction by performing non-linear time history analyses, which are used to construct the fragility curves for five damage states and to obtain the damage probabilities. The method and results obtained in this paper could provide guidance for seismic performance assessment studies and for the seismic design of DC piers in girder bridges.

FRAGILITY ANALYSIS METHODOLOGY

The basic theory of fragility analysis

The seismic fragility analysis is based on the comparison between the seismic capacity and demand to assess if the seismic capacity of the structure is exceeded beyond a specified damage level, for a given ground motion intensity. The probability of such event can be expressed as:

$$P_f = P\left(\frac{D_d}{D_c} \geq 1 | IM\right) \quad (1)$$

where P_f is the failure probability, D_d is the seismic demand on the structures, D_c is the capacity of the structure, and IM is the ground motion intensity measure.

To obtain the fragility curves, both demand and capacity of the structure need to be assessed. For this purpose, the Bayesian probabilistic seismic demand model (PSDM) can be used to obtain the structural demand, as presented by Gardoni *et al.* [18] and Ahmad *et al.* [19]. Limit states are defined as the thresholds of prescriptive damage states for the structural capacity (e.g., slight, moderate, extensive and complete damage – more details ahead) [20,21]. In this paper, the PSDM of the DC bridge piers is developed using nonlinear time-history analyses to establish a relationship between the seismic demand and the ground motion intensity. The displacement ductility ratio of the piers is selected as the engineering parameter for the limit state capacity.

Fragility analysis procedure for DC piers

The fragility analysis procedure herein proposed considers the structural characteristics of the DC piers and the different responses under longitudinal and transverse seismic inputs. It is described as follows: (1) A nonlinear model of the bridge is first established by considering the interaction between pile and soil; (2) 100 seismic records are selected from the Pacific Earthquake Engineering Research Center (PEER) – which are suitable for the type of sites considered – to formulate series of "bridge-ground motion" samples; (3) The damage indices of bridge piers for different damage states are determined based on the displacement responses corresponding to the failure states obtained by a pushover analysis. These responses are also used to assess the pier capacity and damage indices; (4) The seismic demand is then obtained by a nonlinear time history analysis using the finite element model established in Step 1; (5) The probability function of the structural response exceeding a specific damage state under different levels of ground motion is calculated; and (6) the fragility curves of DC bridge piers are plotted as a function of the selected ground motion intensities.

ANALYTICAL MODELING AND SIMULATION

Description of the bridge model

The elevation and components of the selected bridge are shown in Figure 1. The bridge has five equivalent spans of 30 m each. A continuous structural system is adopted for the bridge deck. The girders are supported by four DC piers of 30 m height and two abutments. C50 concrete, with standard compressive strength of 29.6 N/mm², is applied to the girders, while C40 concrete (with standard compressive strength of 26.8 N/mm²) is applied to both DC piers and straining beams. The longitudinal reinforcement ratio of the column and straining beam is 0.852% and 0.485%, respectively. A fixed bearing is arranged on the middle pier, as shown in Figure 1, and movable bearings are arranged on the other piers and the abutments.

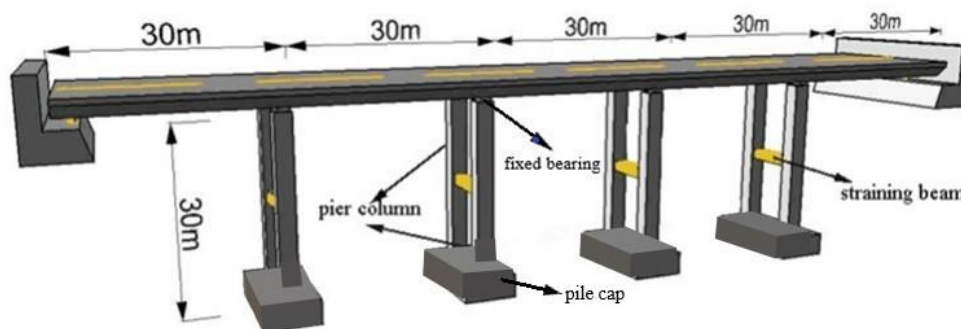


Fig. 1 -Structural layout of the bridge

The numerical model of the bridge is developed using SAP2000 software. The bridge girder is simulated using linear elastic beam elements, since the superstructure remains elastic when subjected to the seismic actions considered in this study. Elasto-plastic fiber column-beam elements are used to simulate the pier columns and straining beams. Both piers and superstructure are connected using the bearings. The piers are fixed on rigid pile caps, which in turn are connected to elements with six degrees of freedom placed under the pile cap to simulate the soil-pile-superstructure seismic interaction, as recommended by Zhang and Dias-da-Costa [3].

Details of different types of DC piers

Eight models of DC piers with different number and layout of straining beams, and direction of seismic input are herein used to assess the seismic fragility. A typical representation of the DC piers is shown in Figure 2, whereas the different variations are listed in Table 1. Figure 3 shows the cross sections of pier columns and the steel bar arrangement, in which ϕ represents the diameter of the steel bar in millimetre. The longitudinal and transverse steel bars all have a yielding strength of 335 MPa.

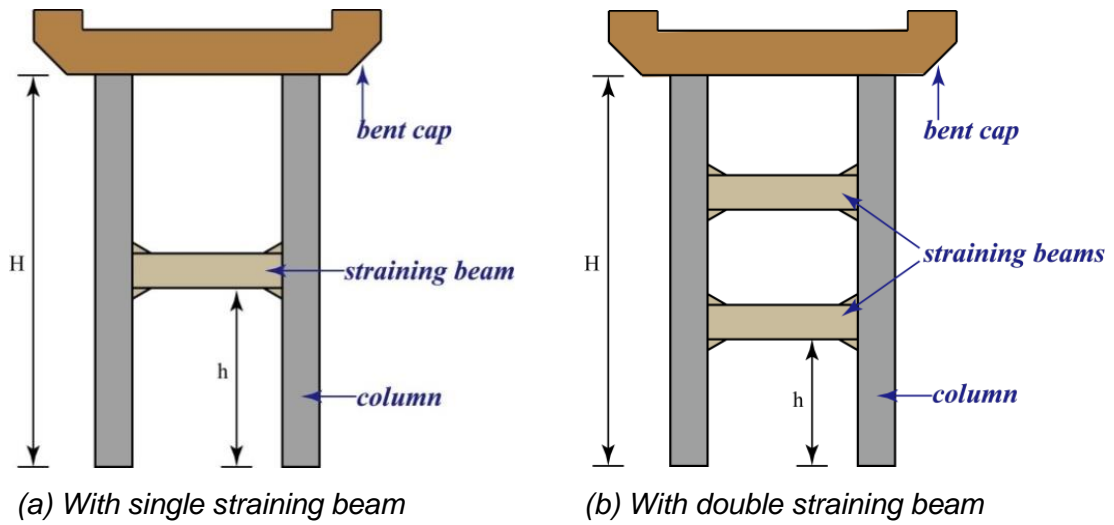


Fig. 2 - Typical DC piers

Tab. 1 - Types of models for the DC piers

Model	Number of straining beams	Position of Straining beams (h/H)*	Seismic input direction
1	1	0.3	longitudinal
2	1	0.5	longitudinal
3	1	0.7	longitudinal
4	1	0.3	transverse
5	1	0.5	transverse
6	1	0.7	transverse
7	2	0.5 and 0.8	transverse
8	2	0.5 and 0.8	longitudinal

Notes: H is the height of pier column; h is the distance from the bottom of the straining beam to the bottom of the pier column.

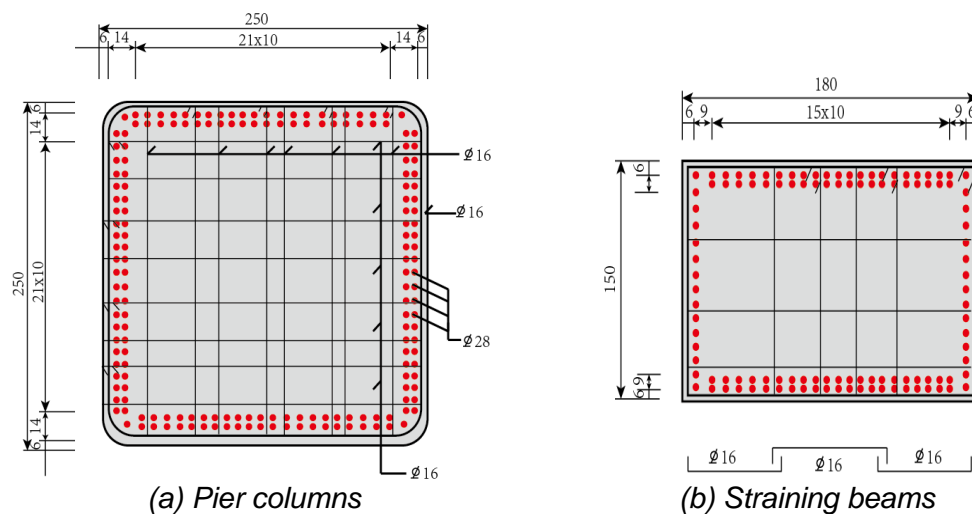


Fig. 3 – Cross sections and steel bar arrangement of components (unit: cm)

Ground motion input

A total of 100 near-fault strong ground motion records are selected to conduct the seismic fragility analyses of the DC bridge piers. These records cover a wide range of values and are available from the PEER strong earthquake database. All selected ground motions have the PGA ranging from 0 to 0.8 g with epicentral distances less than 20 km. The PGA distribution and corresponding spectral accelerations are shown in Figure 4.

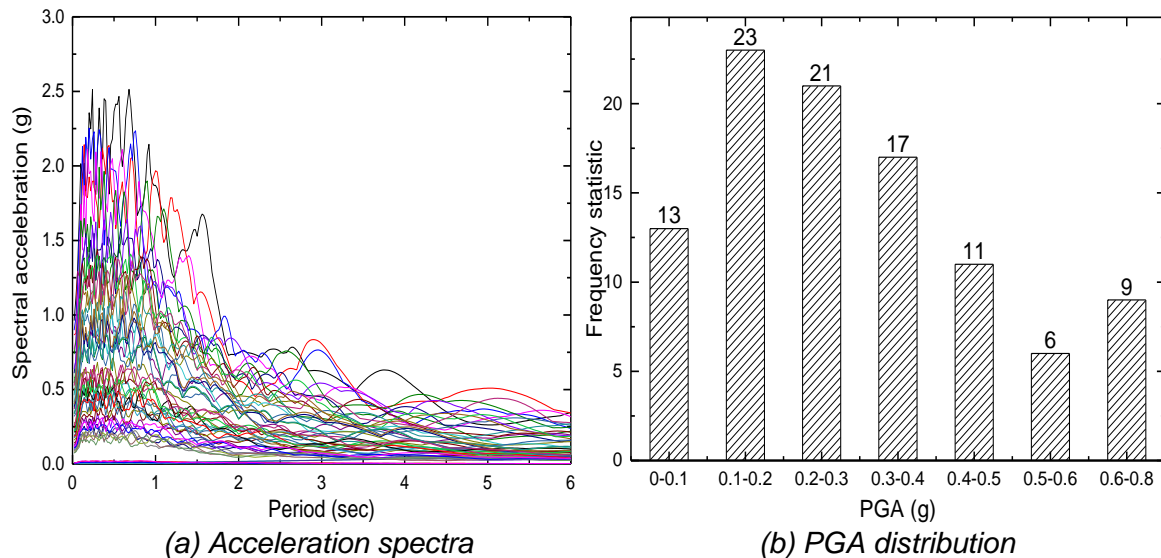


Fig. 4 -Selected ground motions

CHARACTERISATION OF DAMAGE STATES

To estimate the seismic fragility of the bridges, the damage states of the structure are determined in terms of performance level by considering the relationship between the damage index and the structural capacities or limit states. In the present work, the displacement ductility of the bridge piers is used to determine five damage states, as suggested by Hwang *et al.* [22], Padgett *et al.* [23] and Zhang and Huo [24].

In the following sections, the damage index for DC bridge piers is defined using a displacement failure criterion in the longitudinal direction. The displacements corresponding to each damage state is obtained from pushover analyses carried out to assess the structural capacities of the DC bridge piers.

Damage index in the longitudinal direction

The damage indices suggested by Hwang *et al.* [22] are herein adopted for the longitudinal DC bridge piers. A relative displacement ductility ratio is used to define the following five damage states according to FEMA [20]: no damage, slight damage, moderate damage, extensive damage and complete damage. Table 2 summarises the definition of the damage states based on the displacement ductility ratio, μ_d . This parameter represents the ratio between the maximum relative displacement (Δ) and the initial yield displacement (Δ_{cy1}) according to the equation below:

$$\mu_d = \frac{\Delta}{\Delta_{cy1}} \tag{2}$$

Tab. 2 - Bridge damage states in the longitudinal direction

Damage state	Damage index	Description
No damage	$\mu_d \leq \mu_{cy1}^*$	No damage
Sight damage	$\mu_{cy1} < \mu_d \leq \mu_{cy}$	Longitudinal reinforcement first yields
Moderate damage	$\mu_{cy} < \mu_d \leq \mu_{c4}$	Protective layer of concrete peels partly; longitudinal steel yielding; remaining components in normal use
Extensive damage	$\mu_{c4} < \mu_d \leq \mu_{cmax}$	Core concrete severely cracked; reinforcement exposed
Complete damage	$\mu_d > \mu_{cmax}$	Bridge collapses

Notes: μ_{cy1} is the displacement ductility ratio when the steel first yields; μ_{cy} is the yielding displacement ductility ratio; μ_{c4} is the displacement ductility ratio when the concrete compressive strain reaches 0.004; μ_{cmax} is the maximum displacement ductility ratio.

Damage index in the transverse direction

The method proposed above cannot be directly applied to the definition of the damage index in the transverse direction due to the dynamic axial force of the straining beams. For this purpose, 30 DC bridge piers OpenSees models with straining beams of different location are used to obtain the capacity of the pier. The location ranges in evenly incremental steps from $0.2H$ to $0.7H$, where H is the height of the pier column. Models with double straining beams are also considered with their location selected between $0.5H$ and $0.7H$. In both types of models, the displacement for which the steel bars first yield and the ductility ratio when the concrete strain reaches 0.004 are obtained.

Both pier columns and straining beams are simulated using nonlinear fiber column-beam elements. The cross-sections of the pier columns are divided into core and cover areas due to the confinement of the stirrups. Elastic elements simulate the bent-cap and the vertical load of each column is 5,600 kN, which corresponds to the weight of the superstructure above the piers.

The formula applicable to the calculation of the displacement at the top of a single column pier is given by:

$$\Delta_{cy1} = \frac{\phi'_y H^2}{3} \tag{3}$$

where ϕ'_y is the yield curvature of the section, H is the height of pier column, and Δ_{cy1} is the displacement at the top of the pier when the steel within the plastic hinge region first yields.

A simplified method to obtain the elastic-plastic displacement capacity of the bent pier was proposed by Shen *et al.* [24] based on the single-column pier relation. For DC piers with one or more straining beams, a reduction factor β related with the relative position of straining beam (h) can account for the contribution of the straining beams to the displacement. This reduction factor can be expressed as:

$$\beta = \frac{\Delta'_{cy1}}{\Delta_{cy1}} \tag{4}$$

where β is the reduction factor, Δ'_{cy1} is the top displacement of DC pier, and Δ_{cy1} is the top displacement of single-column pier.

The reduction factor can be calculated from the relationship between the top displacement of the DC piers and the single-column piers provided by pushover analyses. A summary of the analytical results (6 of 30 cases for DC pier) are listed in Table 3 and the regression analysis made based on these results is represented in Figure 5.

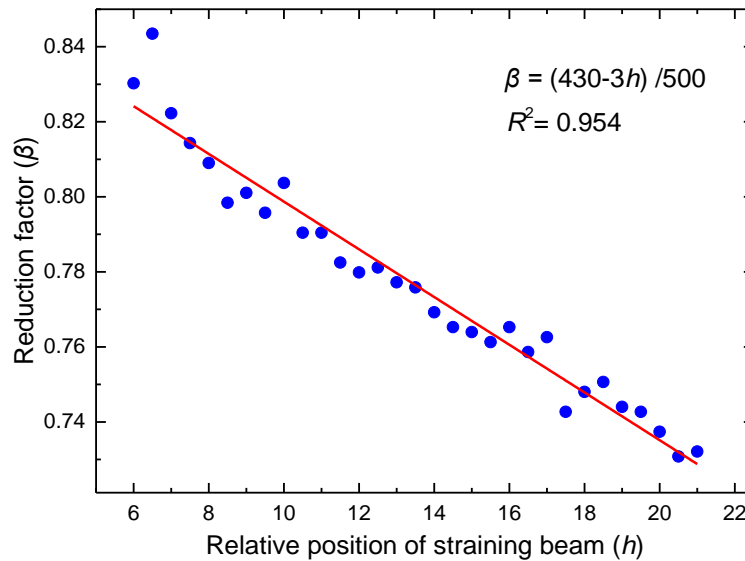


Fig. 5 -Regression analysis of the relationship between the reduction factor and straining beam Position

Tab. 3 - Displacement at the top of the pier obtained by pushover analyses (mm)

Stress state	Single-column pier	DC pier					
		0.2H	0.3H	0.4H	0.5H	0.6H	0.7H
Steel first yields	377	313	302	294	288	282	276
Concrete strain when compression reaches 0.004	1011	438	429	420	414	408	402

The regression analysis equation relates the displacement at the top of DC piers with the yielding of the steel reinforcement and the relative position of the straining beam:

$$\Delta_{cy} = \beta \Delta_{cy} = \left(\frac{430 - 3h}{500} \right) \frac{\phi'_y H^2}{3} \tag{5}$$

where ϕ'_y is the yield curvature of the section, H is the height of pier column (m), and h is the distance from the bottom of the straining beam to the bottom of the pier column (m).

To predict the plastic displacement capability of the pier, it is necessary to have a reasonable estimate of the equivalent plastic hinge length. The equation suggested by Priestley *et al.* [26] is herein recovered. Accordingly:

$$L_p = 0.08H + 0.022 f_y d_s \geq 0.04 f_y d_s \tag{6}$$

where L_p is the length of the plastic hinge, and f_s is the characteristic strength, and d_s the diameter of the longitudinal bar.

The plastic rotation of the DC pier can then be calculated by:

$$\theta_u = L_p (\phi_u - \phi_y) / K \tag{7}$$

where θ_u is the plastic rotation, ϕ_u is the limit curvature of the cross section, ϕ_y is the equivalent yield curvature, and K is the security ductility coefficient, usually taken as 2.

Finally, the formula to calculate the capacity at the top of the DC pier is proposed as follows:

$$\Delta_u = \beta \frac{\phi'_y H^2}{3} + \theta_u \left(h - \frac{L_p}{2} \right) \quad (8)$$

Determination of the damage indices

The pushover model with two straining beams (the relative height of the straining beams are $0.5H$ and $0.8H$) has nearly the same displacements as the model with a single straining beam, when the relative height of the straining beam is $0.5H$. Therefore, the displacement at the top of the DC pier in the first case can also be approximated by the expression for a pier with a single straining beam.

The probabilistic characteristics of the structural capacity of the bridge expressed in terms of ductility ratios can be described using a lognormal distribution [9,14]:

$$\mu_c = Ln(\tilde{\mu}_c, \beta_c) \quad (9)$$

where $\tilde{\mu}_c$ is the medium value of the structural capacity, and β_c is the logarithmic standard deviation. The median values of the structural capacity for the different damage state are listed in Table 4.

Tab. 4 - Median values for the structural capacity under different damage states

Damage state	Model 1,2,3 and 7	Model 4	Model 5	Model 6	Model 8
μ_{cy1}	1	1	1	1	1
μ_{cy}	1.23	1.23	1.23	1.23	1.23
μ_{c4}	2.69	1.42	1.44	1.47	1.44
μ_{max}	5.69	4.42	4.44	4.47	4.44

Notes: parameter definition is the same as in Table 2.

SEISMIC FRAGILITY ANALYSIS OF DC BRIDGE PIERS

Probability analysis of structural responses

The probabilistic characteristic of the structural demand can also be described by a lognormal distribution as:

$$\mu_d = Ln(\tilde{\mu}_d, \beta_d) \quad (10)$$

where $\tilde{\mu}_d$ is the medium value of the structural demand, and β_d is the logarithmic standard deviation. Both are determined from the regression of the simulated response date.

The regression analysis of the displacement ductility ratio versus PGA are shown in Figure 6 and the regression functions for all models are summarized in Table 5. It should be noted that the time history analysis are conducted using SAP2000.

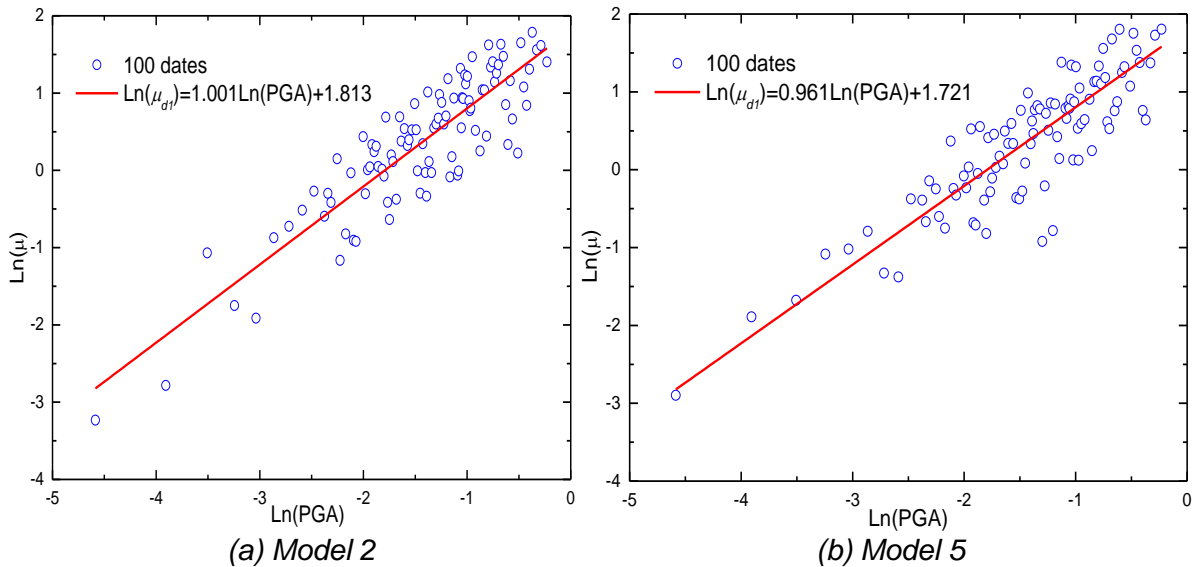


Fig. 6 -Regression analysis of displacement ductility ratio versus the PGA

Tab. 5 - Regression function for all pier models

Model	Seismic input	Fitting function	R ²
1	longitudinal	Ln(μ _{d1})=1.0107(PGA)+1.8129	0.8256
2	longitudinal	Ln(μ _{d2})=0.9337(PGA)+1.8037	0.7765
3	longitudinal	Ln(μ _{d3})=0.9124(PGA)+1.7769	0.8133
4	transverse	Ln(μ _{d4})=0.9724(PGA)+1.705	0.8021
5	transverse	Ln(μ _{d5})=0.9614(PGA)+1.7208	0.7854
6	transverse	Ln(μ _{d6})=0.9267(PGA)+1.6549	0.7821
7	transverse	Ln(μ _{d7})=0.9233(PGA)+1.7811	0.8377
8	longitudinal	Ln(μ _{d8})=0.9759(PGA)+1.7438	0.8189

Notes: PGA is the peak ground acceleration; R² is the variance.

Fragility curves of DC piers

The probability of the structure demand μ_d exceeding the capacity μ_c is described by the following equation:

$$P_f = P\left(\frac{\mu_c}{\mu_d} \leq 1\right) = P\left[\ln\left(\frac{\mu_c}{\mu_d}\right) \geq 0\right] \quad (11)$$

It is highlighted that Equation (10) can be transformed into a standard normal distribution since μ_d and μ_c both follow a lognormal distribution. The equation is written as:

$$P_f = \Phi\left(\frac{-\ln(\mu/\mu_d)}{\sqrt{\beta_c^2 + \beta_d^2}}\right) \quad (12)$$

where (β_c²+β_d²)^{1/2} is equal to 0.5 when the PGA is selected as the intensity measure. The median values of the capacities of the components corresponding to the different failure states are listed in Table 4, whereas, the median values for the seismic demand on the piers corresponding

to the different seismic waves are shown in Table 5. The failure probability of the piers in the different conditions can be obtained from Equation (11) and the corresponding fragility curves are shown in Figure 7.

To allow more clearly comparisons of the fragility of the bridge piers in different categories, the damage probabilities of the piers along with the relative difference, \mathcal{E} , according to the damage likelihood of the eight models at the four damage states under 0.5 g seismic waves, are presented in Table 6. The eight piers are divided into three groups in Table 6: Group 1 consists of three piers with single straining beam subjected to longitudinal seismic waves; Group 2 consists of three piers with single straining beam subjected to transverse seismic waves; and Group 3 consists of two piers with double straining beams. It should be noticed that 'ref' identifies the pier model from each group used as reference in the calculation of the relative differences for the other piers in the same group.

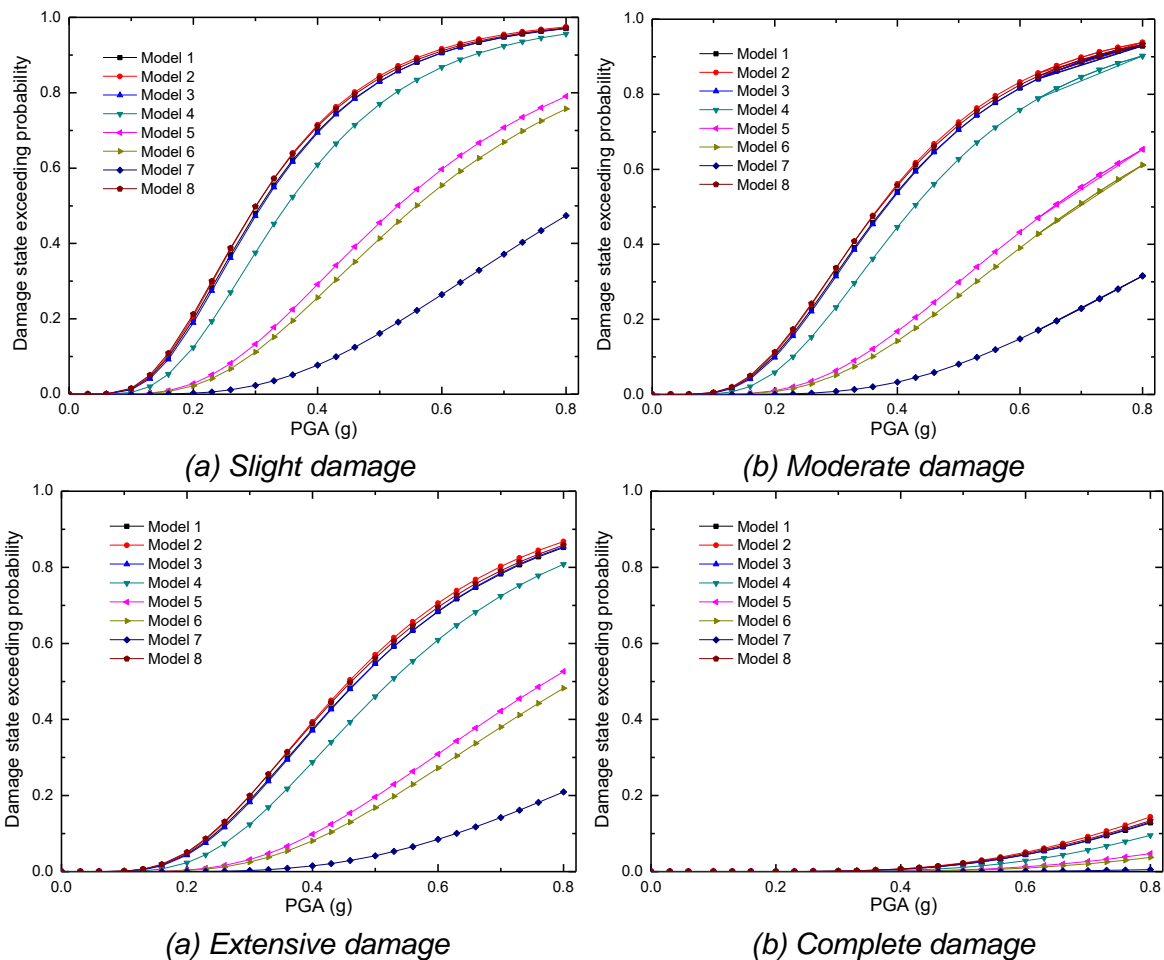


Fig. 7 -The fragility curves of DC piers for each damage state

Tab. 6 - Damage probabilities of the piers at 0.5 g

Group	Model	Damage state							
		Slight damage		Moderate damage		Extensive		Complete	
		P^*	\mathcal{E}	P	\mathcal{E}	P	\mathcal{E}	P	\mathcal{E}
Group 1	1	83.0%	ref	70.6%	ref	54.7%	ref	1.9%	ref
	2	84.5%	0.018	72.6%	0.028	57.0%	0.042	2.3%	0.211
	3	83.0%	0	70.5%	-0.001	54.6%	-0.002	2.0%	0.053
Group 2	4	77.0%	ref	62.7%	ref	46.1%	ref	11.0%	ref
	5	45.5%	-0.409	29.9%	-0.523	19.6%	-0.575	0.5%	-0.955
	6	41.3%	-0.464	26.3%	-0.581	16.9%	-0.633	0.4%	-0.964
Group 3	7	16.2%	-0.807	8.0%	-0.889	4.2%	-0.925	0.2%	-0.905
	8	83.9%	ref	71.8%	ref	56.1%	ref	2.1%	ref

Notes: P is the damage probabilities of the piers; \mathcal{E} is the relative differences in each group.

As can be donated from Figure 7, the probabilities of failure for the DC piers under transverse seismic inputs are smaller than those under longitudinal seismic inputs. For example, in Table 6, the damage probabilities of Models 4, 5 and 6 for the extensive damage state under transverse waves ranging from 16.9% to 46.1% are significantly smaller than those of Models 1, 2 and 3 under longitudinal waves ranging from 54.6% to 57.0%. Also from Figure 7, it can be concluded that the bridge piers with double straining beams have lower probabilities of damage under a given level of transverse earthquake intensity in comparison to a single straining beam. Taking Models 5 and 7 for example, the probabilities of slight damage of the former model is 45.5% (see Table 6), whereas the 16.2% is found in the latter. This represents a reduction of 64.4% relatively to Model 5 under 0.5 g transverse seismic input.

Regarding the influence of the position of straining beams, it is obvious from Table 6 that the damage probabilities of the piers under transverse seismic inputs decrease with the increasing relative height of the straining beams. Taking Group 2 for instance, it is observed that the moderate damage probabilities of Models 4, 5 and 6 (with h/H of 0.3, 0.5 and 0.7) are 62.7%, 29.9% and 26.3%, respectively, with the probability reducing 52.3% for Model 5 and 58.1% for Model 6, compared with that of Model 4. For the seismic fragility of DC pier under the longitudinal seismic input, it can be seen from Figure 7 that the fragility curves of Models 1, 2, 3, and 8 almost overlap. Taking the moderate damage state as example, the probabilities of Models 1, 2, 3 and 8 are 70.6%, 72.6%, 70.5% and 71.8%, respectively, in which case the maximum difference is only 2.1%. This confirms that the straining beam has reduced influence over the seismic fragility of DC piers in the longitudinal direction.

CONCLUSIONS

This paper adopts an analytical method to assess the seismic fragility of DC bridge piers with straining beams varying in number and relative position for different seismic input directions. Simplified formulas are proposed to calculate the capacity of the DC bridge piers under transverse seismic waves.

The fragility curves of DC piers with different straining beams are constructed for five damage states. Based on the obtained results, it is clear that DC bridge piers are more vulnerable to longitudinal seismic inputs than to transverse seismic inputs. The damage probability for DC piers with single straining beam under transverse seismic inputs decreases with the increasing relative location of the straining beams, with the relative position of straining beam between $0.3H$ and $0.7H$ (H is the height of pier column). When two straining beams are used, there is a

significant improvement of the seismic performance of DC piers in the transverse direction. These observations are particularly relevant to the design and improvement of the seismic capacity of girder bridges with DC piers, as well as to better predict their seismic performance.

ACKNOWLEDGEMENTS

The research described in this paper was supported by the National Natural Science Foundation of China (Grant No.: 51508276), and the Fund of National Engineering and Research Center for Mountainous Highways (Grant No.: GSGZJ-2017-02).

REFERENCES

- [1] Nielson B.G., DesRoches R., 2007. Analytical seismic fragility curves for typical bridges in the central and southeastern united states. *Earthquake Spectra*, vol. 23(3): 615–633
- [2] Wu F., Zhang Q., Feng B., et al., 2016. Research on the aseismic behavior of long-span cable-stayed bridge with damping effect. *The Civil Engineering Journal*, vol. 8: 1-9
- [3] Zhang Y., Dias-da-Costa D., 2017. Seismic vulnerability of multi-span continuous girder bridges with steel fibre reinforced concrete columns. *Engineering Structures*, vol. 150: 451–464
- [4] Ramanathan K., Desroches R., Padgett J.E., 2012 A comparison of pre- and post-seismic design considerations in moderate seismic zones through the fragility assessment of multispan bridge classes. *Engineering Structures*, vol. 45: 559–573
- [5] Zhang K., Sun Q., 2017. Strengthening of a reinforced concrete bridge with prestressed steel wire ropes. *The Civil Engineering Journal*, vol. 3: 267–285
- [6] Tavares D.H., Padgett J.E., Paultre P., 2012. Fragility curves of typical as-built highway bridges in eastern Canada. *Engineering Structures*, vol. 40: 107–118
- [7] Biglari M., Ashayeri I., Bahirai M., 2016. Modeling, vulnerability assessment and retrofitting of a generic seismically designed concrete bridge subjected to blast loading. *International Journal of Civil Engineering*, vol. 14:379–409
- [8] Yamazaki F., Motomura H., Hamada T., 2000. Damage assessment of expressway networks in Japan based on seismic monitoring. *Proceedings of the 12th World Conference on Earthquake Engineering*, Auckland, New Zealand
- [9] Shinozuka M., Feng M.Q., Kim H.K., et al., 2000. Nonlinear static procedure for fragility curve development. *Journal of Engineering Mechanics-ASCE*, vol. 126(12):1287–1295
- [10] Mander J.B., Basoz N., 1999. Seismic fragility curve theory for highway bridges, *Proceedings of the 5th United States Conference on Lifeline Earthquake Engineering*, Seattle, USA.
- [11] Hwang H., Jernigan J.B., Lin Y.W., 2000. Evaluation of seismic damage to Memphis bridges and highway systems. *Journal of Bridge Engineering*, vol. 5:322–330
- [12] Karim K.R., Yamazaki F., 2001. Effect of earthquake ground motions on fragility curves of highway bridge piers based on numerical simulation. *Earthquake Engineering and Structural Dynamics*, vol. 30(12):1839–1856
- [13] Padgett J.E., DesRoches R., 2008. Methodology for the development of analytical fragility curves for retrofitted bridges. *Earthquake Engineering and Structural Dynamics*, vol. 37(8):1157–1174
- [14] Choi E., DesRoches R., Nielson B., 2004. Seismic fragility of typical bridges in moderate seismic zones. *Engineering Structures*, vol. 26: 187–199
- [15] Nielson B.G., DesRoches R., 2007. Seismic fragility methodology for highway bridges using a component level approach. *Earthquake Engineering and Structural Dynamics*, vol. 36(6): 823–839
- [16] Ramirez C.M., Miranda E., 2012. Significance of residual drifts in building earthquake loss estimation. *Earthquake Engineering and Structural Dynamics*, vol. 41(11): 1477–1493
- [17] Zhang Y., Fan J., Fan W., 2016. Seismic fragility analysis of concrete bridge piers reinforced by steel fibers. *Advances in Structural Engineering*, vol. 19(5):837–848
- [18] Gardoni P., Mosalam K.M., Kiureghian A.D., 2003. Probabilistic seismic demand models and fragility estimates for RC bridges. *Journal of Earthquake Engineering*, vol. 7(S1):79–106
- [19] Ahmad S., Kyriakides N., Pilakoutas K., et al., 2015. Seismic fragility assessment of existing sub-standard low strength reinforced concrete structures. *Earthquake Engineering and Engineering Vibration*, vol. 14(3):439–452

- [20] FEMA, 2005. HAZUS-MH software, Federal Emergency Management Agency, Washington D.C., USA
- [21] Noori H.Z., Amiri G.G., Nekooei M., Zakeri B., 2016. Seismic fragility assessment of skewed MSSS-I girder concrete bridges with unequal height columns. *Journal of Earthquake and Tsunami*, vol. 10(1):1550013
- [22] Hwang H., Liu J.B., Chiu Y.H., 2001. Seismic fragility analysis of highway bridges. Mid-America Earthquake Center report: project MAEC RR-4, University of Illinois at Urbana-Champaign, USA.
- [23] Padgett J.E., Nielson B.G., DesRoches R., 2008. Selection of optimal intensity measures in probabilistic seismic demand models of highway bridge portfolios. *Earthquake Engineering and Structural Dynamics*, vol. 37(5):711–725
- [24] Zhang J., Huo Y.L., 2009. Evaluating effectiveness and optimum design of isolation devices for highway bridges using the fragility function method. *Engineering Structures*, vol. 31(8): 1648–1660.
- [25] Shen X., Ye A., Wang X., 2014. Simplified calculation method of elastic-plastic displacement capacity for double-column bent. *Journal of Tongji University*, vol. 42(4): 513–519 (In Chinese)
- [26] Priestley M.J.N., Seible F., Calvi G.M., 1996. *Seismic design and retrofit of bridges*. John Wiley & Sons, Inc., New York

EVALUATION ON COMPREHENSIVE BENEFIT OF LARGE-SCALED CONSTRUCTION PROJECT BASED ON FUZZY THEORY: A CASE STUDY OF GUANGZHOU IN CHINA

Jianfeng Li^{1,2}, Yousong Wang¹, Chiyu Luo², Fengwei Cai², Hui Yan^{1}*

- 1. South China University of Technology, School of Civil Engineering and Transportation, Department of Architecture and Civil Engineering, Room 7205, Building No.7, 381st Wushan Road, Tianhe District, Guangzhou 510641, China; cthyan@scut.edu.cn, ljfeng@gdadri.com*
- 2. Architectural Design and Research Institute of Guangdong Province, 97st Liuhua Road, Liwan District, Guangzhou 510010, China*

ABSTRACT

With the implementation of “The Belt and Road” policy and increasing investment, there will be a large number of large-scaled construction projects (LSCP) in China. However, the comprehensive benefit of most LSCP is not satisfactory because of concerning more about the economic benefits. It makes the sustainability of LSCP concerned about. In order to ensure the sustainable development, the evaluation of the comprehensive benefit of LSCP should be carried out. Based on comprehensive literature review and content analysis, 30 influence factors of comprehensive benefit evaluation for LSCP are identified. The evaluation index system of 17 factors containing three subsystems of social, economic and environmental benefit is established through factor analysis. Entropy method is used to determine weights of each indicator, and then synthetic evaluation model is put up. This paper selects a practical case, Lieder Village reconstruction in Guangzhou, to calculate the synthetic evaluation value using fuzzy theory. The evaluation results are satisfactory and in line with reality. It shows that the evaluation index system and synthetic evaluation model has a certain reference value for analysis of comprehensive benefit and can help for enhancing the construction and management level of LSCP and promoting the sustainable development of LSCP.

KEYWORDS

Comprehensive benefit; Large-scaled construction project; Index system; Fuzzy synthetic evaluation; Construction management; Case study

INTRODUCTION

With more than 30 years of opening-up, Chinese economy experienced rapid development. It is the material base for the investment and construction of large-scaled projects. In recent year, with the implementation of “The Belt and Road” policy and increasing investment, it can be foreseen that there will be a large number of large-scaled construction projects (LSCP) in China.

However, LSCP is often a sacrifice of precious ecosystems and land losses to meet the needs of urban development, which will make our cities face serious social, economic and environmental problems [1]. Moreover, most of LSCP only focus on economic benefit and ignore the social or environmental factors. The construction management model of high input, low efficiency and high energy consumption is often formed, which makes the sustainability of LSCP more concerned. Therefore, combined with the concept of sustainable development, the objective of this paper tries to establish a scientific and comprehensive evaluation index system of comprehensive benefit and construct a fuzzy synthetic evaluation model to analyse the comprehensive benefit of LSCP.

LITERATURE REVIEW

The concept of sustainable development was put forward in the 1970s, but it was not used in LSCP until the 1990s [2]. Some researchers believed that sustainable development had three pillars: society, economy and environment [3]. One of the key features of LSCP is that the costs are far more than normal projects because they are built at one time, with huge and long-term impact [4]. LSCP is regarded as a good way to solve social problems, environmental impact and economic development [5-7]. More studies are trying to research LSCP from different perspectives. Tam believed that sustainable building should take into consideration three aspects of society, economy and environment, and integrated it into the practice of construction industry [8]. Wang pointed out that in order to promote the sustainable development of projects, engineering construction projects should strengthen sustainable standards in the scheme selection, green technologies used in construction and operation phases, public participation mechanism of project [9]. Abidin believed that sustainable development of LSCP was an important component of sustainable development of construction industry and it was an important way to achieve sustainable development of construction industry [10]. Tang analyzed the distribution of the benefit in a LSCP of PAZHOU Village reconstruction [11]. Catalina analyzed some factors influencing sustainable development of LSCP [12].

The sustainability of LSCP can be reflected by the comprehensive benefit of project. The specific performance is to realize the harmony of social repercussions, the rationality of economic benefit and the adaptability of the natural environment. It has been widely acknowledged on the importance of evaluating comprehensive benefit of LSCP [13]. Adopting appropriate evaluation methods and constructing reasonable evaluation model can effectively evaluate and promote the decision-making for sustainable development of LSCP [14]. There are some researches on assessing the LSCP. Hemphill put forward a hierarchical model, used Delphi method to evaluate and analyze the sustainability of large-scaled public project [15]. Tam put forward a sustainability assessment approach for environmental problems based on organizational behavior [16]. Lee used AHP method and constructed an evaluation model to evaluate sustainable development of some LSCP in Hong Kong [17]. Deng constructed a hierarchical model of urban renewal sustainability evaluation, and applied it to case study [18]. Liu designed a comprehensive assessment system of sustainable LSCP and put forward five measures to obtain the comprehensive benefit of sustainable development [19].

After researching LSCP, many scholars advocated using index system as the dominant evaluation method, because indicators are the most common and popular tools to measure sustainability and comprehensive benefit [20]. To evaluate the comprehensive benefit, some sustainability indicators should be chosen. Some international organizations proposed a large number of sustainability indicators. UN Commission on Sustainable Development(CSD), United Nations(UN) and Ministry of Housing and Urban-Rural Development of the People's Republic of China(MOHURD) [21-23] published most indicators, covering many aspects of sustainable development such as society, economic development, ecological environment, institution, public security and resource conservation, etc. Shen [3] integrated those different sets of indicators and proposed a new list of sustainability indicators, which contains 37 categories of 115 indicators. Singh [24] found that there were 12 categories and more than 60 indicators reflecting sustainable development from different perspectives. Many evaluation indicators were proposed by some other researchers [19-20] [25-26]. These have been used as references for many countries and communities to develop their own evaluation index systems. The selection of indicators should not be the collection of information about all indicators, but rather the selective analysis of those which are more basic in nature [3]. Scholars agree that the evaluation indicators need to be more representative and more in line with the values of the local people [24]. After conducting the literature review and content analysis, through consulting many scholars and professionals, 30 influence factors of comprehensive benefit evaluation associated with LSCP are identified, see Table1.

Tab. 1 - Influence factors of comprehensive benefit evaluation associated with LSCP

NO.	Factors	CSD [21]	UN [22]	MOHU RD[23]	Shen [3]	Singh [24]	Tasaki [25]	Zhao [26]	Liu [19]	Total Number
L01	Traffic improvement status	*	*	*	*	*	*		*	7
L01	Social harmony and stability	*		*	*	*	*	*	*	7
L03	Clean, safe and belonging community	*		*		*	*		*	5
L04	The inheritance of history, culture and urban styles	*	*	*	*	*	*		*	7
L05	Improvement of living and recreation	*	*	*	*	*	*		*	7
L06	Improvement of living conditions	*	*	*	*	*	*	*	*	8
L07	Social welfare improvement	*	*	*	*	*	*	*	*	8
L08	Improvement of public infrastructure	*		*	*	*	*	*	*	7
L09	Development potential after project construction		*	*			*	*	*	5
L10	The degree of public participation	*		*	*	*	*		*	6
L11	Improvement of									

	reputation and income of corporate		*				*	*	*	4
L12	Project construction cycle			*			*	*	*	4
L13	Project construction cost					*	*	*	*	4
L14	Land revenue status		*		*			*	*	4
L15	Per capita disposable income	*	*	*	*	*	*	*		7
L16	Compensation and resettlement cost			*			*	*	*	4
L17	The level of rental income				*	*		*	*	4
L18	Cultural and educational improvement	*	*	*	*		*	*	*	7
L19	Financial internal rate of return (FIRR)				*		*	*	*	4
L20	Dynamic Investment Payback Period		*	*				*	*	4
L21	Financial Net Present Value (FNPV)		*		*		*	*		4
L22	Rate of return on investment (ROR)		*		*		*	*		4
L23	Loan repayment period			*			*	*	*	4
L24	Environmental quality improvement status	*	*	*	*	*	*		*	7
L25	Land use rate	*	*	*	*	*	*		*	7
L26	Land use intensity		*	*	*	*		*	*	6
L27	The impact on ecological environment	*	*	*	*	*	*	*	*	8
L28	Urban landscape function improvement	*	*	*	*	*	*	*	*	8
L29	Building energy efficiency level	*	*	*	*	*	*			6
L30	The coordination degree of new and old buildings	*		*	*		*		*	5

METHODS

The method employed in this research was based on questionnaire survey, factor analysis, entropy method, fuzzy theory and case study. Questionnaire survey is a systematic method of collecting data based on sample. For this study, a questionnaire survey was carried out to investigate the importance of various factors affecting comprehensive benefit of LSCP. Most of evaluation method are expert-driven and need for a greater inclusion of citizen's opinion in the application of evaluation indicators [27]. The questionnaire involved government, enterprises

and institutions, stakeholders, the public, experts and scholars.

Factor analysis

Factor analysis (FA) is a reducing dimension method to simplify the data. It refers to a variety of statistical techniques whose common objective is to represent a set of variables in terms of a smaller number of hypothetical variables [28]. Factor analysis model is as follows:

$$C_i = l_{i1}F_1 + l_{i2}F_2 + \dots + l_{im}F_m + \varepsilon_i \quad (1)$$

C_i is the comprehensive factor, l_{ij} is the factor load, F_j is the common factor, ε_i is the unique factor.

Entropy method

Entropy method is an objective method to calculate the weight of evaluation factors for multi-objective decision-making and it acquires the effective and available information by measuring the data [29]. The basic calculating steps are as follows:

- 1) To construct matrix $X = (x_{ij})_{m \times n}$ of the original evaluation data according to evaluation objects and indicators;
- 2) To normalize matrix X . The original evaluation data can be normalized by:

$$y_{ij} = \frac{\max_j(x_{ij}) - x_{ij}}{\max_j(x_{ij}) - \min_j(x_{ij})} \quad (2)$$

$$y_{ij} = \frac{x_{ij} - \min_j(x_{ij})}{\max_j(x_{ij}) - \min_j(x_{ij})} \quad (3)$$

For small indicators, it can use Equation 2. For maximum indicators, it can use Equation 3.

- 3) To calculate the entropy value E_j of each indicator, if $p_{ij} = 0$, $\lim_{p_{ij} \rightarrow 0} p_{ij} \ln p_{ij} = 0$

$$E_j = -\frac{1}{\ln(m)} \sum_{i=1}^m p_{ij} \ln p_{ij} \quad (4)$$

Where m is the number of evaluation objects, n is the number of evaluation indicators,

$$p_{ij} = \frac{y_{ij}}{\sum_{i=1}^m y_{ij}} \quad (5)$$

- 4) To calculate the weight and obtain entropy weight vector $W = \{w_1, w_2, \dots, w_m\}$.

$$W_j = \frac{1 - E_j}{k - \sum_{j=1}^k E_j} \quad (6)$$

Fuzzy synthetic evaluation

Fuzzy theory has been proven to be an effective multi-criteria decision-making method, which is one of the most popular methods because of its ease use and taking uncertainty into account. It has been adopted in many fields, such as in engineering, economic, environmental, social, medical, and management applications [30-33]. These previous studies demonstrate that fuzzy synthetic evaluation has the advantage of handling complicated evaluation with multiple factors and layers. In fact, the use of the fuzzy methodology helps to capture the ambiguity of human appraisal when uncertain and imprecise data is used. Fuzzy synthetic evaluation method is considered as an effective method for the evaluation of comprehensive benefit of LSCP. It requires the following four elements:

- 1) A set of basic factors $U = \{u_1, u_2, \dots, u_m\}$, u_i standing for the evaluation factor i ;
- 2) A set of grades alternatives $V = \{v_1, v_2, \dots, v_n\}$, v_j being the evaluation grade j ;
- 3) A set of weight vectors $W = \{w_1, w_2, \dots, w_m\}$, w_i denoting the weighting of evaluation factor i ;
- 4) A fuzzy evaluation matrix $Q = (q_{ij})_{m \times n}$, $q_{ij} (i=1,2,\dots,m; j=1,2,\dots,n)$ represents the percentage of respondents who choose v_j for their satisfaction level concerning the factor u_i .

Determination of the membership function for each common factor

Given that the set of grade alternatives for selection are defined as $V = \{1,3,5,7,9\}$, where “1” = very dissatisfied; “3” = dissatisfied; “5” = basically satisfied; “7”= satisfied; and “9” = very satisfied. For each common factor u_{ik} , the membership function can be computed by[33] :

$$\begin{aligned}
 Z_{u_{ik}} &= \frac{P1_{u_{ik}}}{\text{very dissatisfied}} + \frac{P3_{u_{ik}}}{\text{dissatisfied}} + \frac{P5_{u_{ik}}}{\text{basically satisfied}} + \frac{P7_{u_{ik}}}{\text{satisfied}} + \frac{P9_{u_{ik}}}{\text{very satisfied}} \\
 &= \frac{P1_{u_{ik}}}{1} + \frac{P3_{u_{ik}}}{3} + \frac{P5_{u_{ik}}}{5} + \frac{P7_{u_{ik}}}{7} + \frac{P9_{u_{ik}}}{9}
 \end{aligned} \tag{7}$$

Where u_{ik} represents the k^{th} evaluation factor i ; $Z_{u_{ik}}$ denotes the membership function of the evaluation factor u_{ik} ; and $Pt_{u_{ik}}$ ($t=1,3,5,7,9$) is the percentage of respondents who choose t for their satisfaction level concerning the factor u_{ik} . Alternatively, the membership function

of u_{ik} can also be written as $(P1_{u_{ik}}, P3_{u_{ik}}, P5_{u_{ik}}, P7_{u_{ik}}, P9_{u_{ik}})$, where $0 \leq Pt_{u_{ik}} \leq 1$ and $\sum_1^9 Pt_{u_{ik}} = 1$.

RESULTS

Data statistics

The statistics come from 202 participants selected from government departments, the public around the Lieder Village, people participating in the reconstruction, relevant stakeholders as well as the experts who have urban renewal experience. In Table 2 is shown that the 30 to 49 years old account for 73.26%, university degree and above account for 83.66%, people with construction and management experience account for 84.8%. It shows that participants who filled out questionnaires have higher education and rich work experience.

Tab. 2 - Background information of the respondents

1) Age of survey respondents					
Category	20~29 years old	30~39 years old	40~49 years old	50~59 years old	Above 60 years old
Percentage	9.41	42.08	31.18	11.39	5.94
2) Education level of survey respondents					
Category	Below bachelor	Bachelor		Master and above master	
Percentage	16.34	58.42		25.24	
3) Work unit of survey respondents					
Category	Administrative departments	Enterprise	Higher school	Research institutions	other
Percentage	22.77	32.18	13.86	15.35	15.84
4) Urban renewal experience of survey respondents					
Category	None	1~2 years	3~4years	5~6years	Above 6 years
Percentage	15.2	26.3	22.7	17.2	18.6

Data analysis

Before adopting FA for the calculated impact, several tests were conducted to determine the appropriateness of using it.

(1) Reliability analysis was performed to evaluate the internal consistencies of the extracted factors. The value of Cronbach coefficient of social benefit, economic benefit and environmental benefit were calculated to be 0.908, 0.887 and 0.854 respectively, indicating that the questionnaires had a high level of uniformity [34].

(2) Bartlett test of Sphericity (Table3): the value of Bartlett Test of Sphericity was calculated to be 5561.960, 4857.940 and 5503.496 with an associated significance level of 0.000. This suggested that the correlation matrix is not an identity matrix [35].

(3) Kaiser–Meyer–Olkin (KMO): the value of KMO was calculated and shown in Table 3, a value above 0.8 indicating that the collected data would be suitable for factor analysis [35].

(4) Explained variance (EV): to determine how many factors were required to represent 30 evaluation factors, the total percentage of variance explained by each factor was examined. In this study, principal factor extraction with varimax rotation was performed through the SPSS to generate factor loadings for the number of factors to be exacted from a sample of 202 respondents, see Table 4.

Tab. 3 - Cronbach's Alpha coefficient and KMO test analysis of various dimensions' benefit

Aim	Dimension	Question number	Cronbach's Alpha	A sufficient degree of sampling KMO	Bartlett's spherical test		
					Approximate chi-square distribution	DOF	Significance
Comprehensive Benefit	Social Benefit	1-30	0.908	0.890	5561.960	435	0.000
	Economic Benefit	1-30	0.887	0.868	4857.940	435	0.000
	Environmental Benefit	1-30	0.854	0.820	5503.496	435	0.000

Extracting common factor and construction of evaluation index system

According to the results of FA in max orthogonal rotation, the common factors of social benefit, economic benefit and environmental benefit were extracted. The details of the extracted factors, their factor loading and variables contained in each common factor are shown in Table 4. According to Tabachnick [36], maximum load factor (MLF) could be considered to represent the vast majority of the information about the integrated factor. So selecting the factor with maximum load in each principal component to represent the common factors can build the synthetic evaluation index system of LSCP, which contains three levels of target layer, criterion layer and index layer, see Table 4.

Tab. 4 - Synthetic evaluation index system of social, economic, environmental benefit

Target Layer	Criterion layer	Index Layer (common factors)	Load (MLF)	Percentage of EV	Including Variable factor(number)
Comprehensive Benefit	Social Benefit	Improvement of public infrastructure	0.796	46.426	L20,L19,L14,L13,L16,L21,L23
		The degree of public participation	0.838	11.035	L12,L02,L22,L17,L15,L06
		The inheritance of history, culture and urban styles	0.852	5.645	L05,L03,L11,L18,L07
		Urban landscape function improvement	0.777	4.821	L24,L27,L01
		Development potential after project construction	0.678	3.969	L30,L29,L25,L26
	Economic Benefit	Traffic improvement status	0.809	40.865	L30,L28,L24,L08,L27,L23,L26
		Project construction cost	0.739	10.093	L12,L19,L21,L22,L16
		Land use rate	0.739	6.830	L14,L15,L29,L20
		Social welfare improvement	0.857	4.975	L17,L05,L10
		Social harmony and stability	0.762	4.341	L03,L09,L06
		Improvement of reputation and income of corporate	0.704	3.981	L18,L04
	Environmental Benefit	Land revenue status	0.818	44.246	L13,L16,L21,L20,L19,L23
		Improvement of living conditions	0.835	9.551	L15,L17,L22,L07
		Clean, safe and belonging community	0.668	6.477	L29,L09,L08,L02
		Environmental quality improvement	0.779	4.940	L28,L27,L30,L25
		Land use intensity	0.681	4.576	L12,L01,L10
		Cultural and educational improvement	0.707	3.590	L04,L05,L11

Development of weighs for social, economic and environmental benefit

This research selected sixty-three experts with rich experience in LSCP to judge the importance of society, economy and environment for comprehensive benefit by using a five-point Likert scale ("1"= least important, while "5"=most important). Original results evaluation matrix of each index is as follows:

$$X = \begin{bmatrix} 0 & 5 & 16 & 23 & 19 \\ 2 & 5 & 16 & 22 & 18 \\ 1 & 4 & 15 & 25 & 18 \end{bmatrix}^T \quad P_{ij} = \begin{bmatrix} 0.000 & 0.079 & 0.254 & 0.365 & 0.302 \\ 0.302 & 0.079 & 0.254 & 0.349 & 0.286 \\ 0.016 & 0.063 & 0.238 & 0.397 & 0.286 \end{bmatrix}^T$$

To calculate the entropy and weights of social, economic and environmental benefit:

$$E = [0.79 \quad 0.86 \quad 0.81] \quad W = [0.39 \quad 0.26 \quad 0.35]$$

Determine the weight of indicators in index layer

The data was collected from 202 questionnaires. It was to assess the importance of each

factor in index layer for comprehensive benefit of LSCP from social, economic, environmental benefit. By using Equation 2 to 6, the weight of each indicator was calculated and then a synthetic evaluation models can be obtained, as shown in Figure 1.

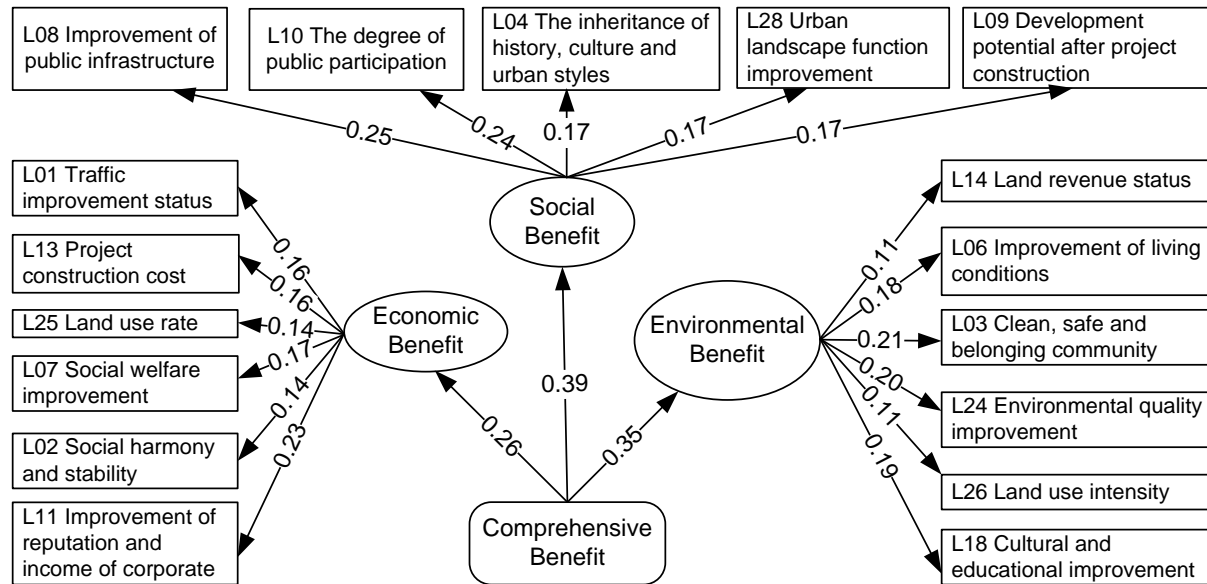


Fig. 1- Synthetic evaluation model of social, economic, environmental benefit

CASE STUDY AND ANALYSIS

With the rapid pace of urbanization, city of Guangzhou continues to expand and produces a large number of urban renewal projects. All urban renewal projects cover an area of about 399.52 square kilometers, in which the area of urban village is about 219.59 square kilometers. To solve the problem of urban village determinate whether urbanization can be carried out successfully and whether can achieve urban sustainable development.

Project background

Lieder Village has a history of over 800 years, which is located in the CBD of Guangzhou. The reconstruction of Lieder Village is the first pilot project of urban village renewal in Guangzhou and it is also a first successful case of urban village renewal by selling land for getting the reconstruction money. According to statistics, Lieder Village land area for reconstruction is about 235,000 m², the building floor area of 600,000 m². The Lieder Village is divided into three areas to implement the reconstruction program: Eastern land is for resettlement of residents. There are 37 high buildings which is about 5662 set house to meet the villagers living themselves and nearly 4,000 sets can be rented; Southwestern land is mainly for the construction of star hotel, creating collective economic income; Western land is sold to developers of 4.6 billion Yuan, equivalent to the floor price of 8095.3 Yuan/m², for the construction of commercial and office. It can be said Lieder Village reconstruction is a LSCP.

Determination of the membership function

As mentioned earlier, a total of 17 common factors were identified for assessing the comprehensive benefit of LSCP. Eighty-nine evaluators participating in the Lieder Village

reconstruction, stakeholders, and experts or scholars were invited to assess each indicator of synthetic evaluation model through a questionnaire. For example, the survey results on the Improvement of public infrastructure of social benefit indicated that 0% of the respondents opined the importance of this common factor for social benefit as very dissatisfied, 0% as dissatisfied; 18% as basically satisfied; 28% as satisfied; 54% as very satisfied. Therefore, the membership function of Improvement of Public Infrastructure is given by Equation 7.

$$\begin{aligned}
 Z_{c1} &= \frac{0.00}{\text{very dissatisfied}} + \frac{0.00}{\text{dissatisfied}} + \frac{0.18}{\text{basically satisfied}} + \frac{0.28}{\text{satisfied}} + \frac{0.54}{\text{very satisfied}} \\
 &= \frac{0.00}{1} + \frac{0.00}{3} + \frac{0.18}{5} + \frac{0.28}{7} + \frac{0.54}{9}
 \end{aligned}$$

It can also be written as (0.00, 0.00, 0.18, 0.28, 0.54). Similarly, the membership functions of all common factors can be derived in the same way, see Table 5.

Tab. 5 - The membership function of all common factors for LSCP

No.	Common factors	Weight	Membership function of Level 3	Membership function of Level 2
C1	Improvement of public infrastructure	0.25	(0.00, 0.00, 0.18, 0.28, 0.54)	(0.01, 0.01, 0.19, 0.27, 0.52)
C2	The degree of public participation	0.24	(0.00, 0.01, 0.20, 0.28, 0.51)	
C3	The inheritance of history, culture and urban styles	0.17	(0.01, 0.02, 0.21, 0.29, 0.46)	
C4	Urban landscape function improvement	0.17	(0.00, 0.01, 0.18, 0.23, 0.58)	
C5	Development potential after project construction	0.17	(0.01, 0.02, 0.20, 0.26, 0.51)	
C6	Traffic improvement status	0.16	(0.00, 0.01, 0.15, 0.21, 0.63)	(0.01, 0.02, 0.16, 0.28, 0.53)
C7	Project construction cost	0.16	(0.01, 0.03, 0.14, 0.28, 0.54)	
C8	Land use rate	0.14	(0.00, 0.02, 0.17, 0.26, 0.55)	
C9	Social welfare improvement	0.17	(0.00, 0.02, 0.16, 0.30, 0.52)	
C10	Social harmony and stability	0.14	(0.02, 0.03, 0.17, 0.37, 0.41)	
C11	Improvement of reputation and income of corporate	0.23	(0.00, 0.01, 0.17, 0.27, 0.55)	(0.01, 0.01, 0.17, 0.30, 0.51)
C12	Land revenue status	0.11	(0.01, 0.02, 0.19, 0.29, 0.48)	
C13	Improvement of living conditions	0.18	(0.01, 0.00, 0.11, 0.29, 0.60)	
C14	Clean, safe and belonging community	0.21	(0.00, 0.00, 0.14, 0.31, 0.55)	
C15	Environmental quality improvement	0.20	(0.00, 0.01, 0.14, 0.29, 0.56)	
C16	Land use intensity	0.11	(0.02, 0.04, 0.21, 0.35, 0.38)	
C17	Cultural and educational improvement	0.19	(0.00, 0.02, 0.24, 0.30, 0.44)	

Taking the social benefit as an example, its membership function is as follows.

$$(0.25 \times 0.00 + 0.24 \times 0.00 + 0.17 \times 0.01 + 0.17 \times 0.00 + 0.17 \times 0.01, 0.25 \times 0.00 + 0.24 \times 0.01 + 0.17 \times 0.02 + 0.17 \times 0.01 + 0.17 \times 0.02, 0.25 \times 0.18 + 0.24 \times 0.20 + 0.17 \times 0.21 + 0.17 \times 0.18 + 0.17 \times 0.20, 0.25 \times 0.28 + 0.24 \times 0.28 + 0.17 \times 0.29 + 0.17 \times 0.23 + 0.17 \times 0.26, 0.25 \times 0.54 + 0.24 \times 0.51 + 0.17 \times 0.46 + 0.17 \times 0.58 + 0.17 \times 0.51) = (0.01, 0.01, 0.19, 0.27, 0.52)$$

Tab. 6 - The results of fuzzy synthetic evaluation for comprehensive benefit of LSCP

No.	Critical factors	Weight	Membership function of Level 2	Membership function of Level 1
B1	Social benefit	0.39	(0.01, 0.01, 0.19, 0.27, 0.52)	(0.01, 0.01, 0.18, 0.28, 0.52)
B2	Economic benefit	0.26	(0.01, 0.02, 0.16, 0.28, 0.53)	
B3	Environmental benefit	0.35	(0.01, 0.01, 0.17, 0.30, 0.51)	

After deriving the membership function of Level 1, the fuzzy evaluation value (FEV) of social benefit, economic benefit, environmental benefit and comprehensive benefit can be calculated using Equation 7:

$$Z_{B1} = 0.01 \times 1 + 0.01 \times 3 + 0.19 \times 5 + 0.27 \times 7 + 0.52 \times 9 = 7.56$$

$$Z_{B2} = 0.01 \times 1 + 0.02 \times 3 + 0.16 \times 5 + 0.28 \times 7 + 0.53 \times 9 = 7.60$$

$$Z_{B3} = 0.01 \times 1 + 0.01 \times 3 + 0.17 \times 5 + 0.30 \times 7 + 0.51 \times 9 = 7.58$$

$$Z_{A1} = 0.01 \times 1 + 0.02 \times 3 + 0.16 \times 5 + 0.28 \times 7 + 0.53 \times 9 = 7.58$$

To have an in-depth analysis, the fuzzy evaluation value of each common factor can also be calculated using the same method. The results are shown in Table 7.

Fuzzy evaluation analysis

The empirical research finding (Table 7) shows that the fuzzy evaluation value of social, economic and environmental benefits are 7.56, 7.60 and 7.58 respectively. The value is very close, showing that it basically balances the benefit of the three critical factors. So it reflects the comprehensive benefit is 7.58, which can be regarded as between “satisfied” and “very satisfied”. In addition, the survey respondents perceived that “Urban landscape function improvement” in the evaluation index of social benefit is the most CF, with the value equal to 7.76; with “The inheritance of history, culture and urban styles” being the last, with the value

equal to 7.29. In the evaluation index of economic benefit, “Traffic improvement status” is the first, with the value equal to 7.92; “Social harmony and stability” the last, with the value equal to 7.24; For the environmental benefit, “Improvement of living conditions” is the higher, with the value equal to 7.99; and “Land use intensity” the lower, with the value equal to 7.06. These research findings revealed that the LSCP of Lieder Village completed the construction of urban infrastructure, beautified the environment, promoted economic development and inherited cultural heritage. However, the density of new building is too large. On the other hand, during the period of construction, especially for the problem of demolition compensation, some conflicts occurred among different stakeholders. Moreover, although some historical and cultural buildings were rebuilt, it has little regrets for the old buildings in the overall demolition and reconstruction of old Lieder Village. But in whole, the fuzzy results are line with the reality and Lieder Village reconstruction is satisfactory.

Tab. 7 - The membership function of all common factors for LSCP

No.	FEV	No.	Critical factors	FEV	No.	Common factors(CF)	FEV
A1	7.58	B1	Social Benefit	7.56	C1	Improvement of public infrastructure	7.72
					C2	The degree of public participation	7.58
					C3	The inheritance of history, culture and urban styles	7.29
					C4	Urban landscape function improvement	7.76
					C5	Development potential after project construction	7.48
		B2	Economic Benefit	7.60	C6	Traffic improvement status	7.92
					C7	Project construction cost	7.62
					C8	Land use rate	7.68
					C9	Social welfare improvement	7.64
					C10	Social harmony and stability	7.24
					C11	Improvement of reputation and income of corporate	7.72
		B3	Environmental Benefit	7.58	C12	Land revenue status	7.37
					C13	Improvement of living conditions	7.99
					C14	Clean, safe and belonging community	7.82
					C15	Environmental quality improvement	7.80
					C16	Land use intensity	7.06
					C17	Cultural and educational improvement	7.32

CONCLUSIONS

(1) This research has developed a comprehensive, objective, reliable, and practical evaluation model for assessing the comprehensive benefit of LSCP using Entropy method and fuzzy synthetic evaluation approach. In the synthetic evaluation model, the weights of social, economic and environmental benefit are 0.39, 0.26 and 0.35 respectively. It perceives that social benefit is most important. To achieve social benefit of LSCP is the key to maintain social harmony and stability, which can help to complete the LSCP smoothly and successfully.

(2) The synthetic evaluation model this paper constructs reflects the basic elements of sustainable development. The result of using this model to evaluate the Lieder Village reconstruction is satisfactory and in line with reality. The developed model provides an objective basis for assessing the comprehensive benefit of LSCP.

(3) The development of evaluation index system not only enhances the understanding of government and investors in implementing a successful LSCP, but it also provides reference for construction managers to measure, evaluate and improve the current performance of LSCP. It can be seen from the evaluation index system that LSCP should pay attention to the construction of public infrastructure, public participation, the inheritance of historical, cultural and

urban styles, community's cleanliness and safety, environmental quality improvement, the interests of enterprises and social security of residents.

(4) This research enables manager to better understand what the comprehensive benefit should be assessed for LSCP. It also assists manager in planning and control for LSCP. An automated system for the fuzzy comprehensive benefit evaluation model of LSCP could be developed in the future. By doing so, a practical comprehensive benefit evaluation tool for LSCP could be used for benchmarking purposes.

ACKNOWLEDGEMENT

This research is funded by National Natural Science Foundation of China (Grant No. 71501074), Natural Science Foundation of Guangdong Province (2015A030313211).

REFERENCES

- [1] Alcamo J., Bennett E.M., 2003. Ecosystems and human wellbeing: A framework for assessment. *Physics Teacher*, 34 (9), 534-534.
- [2] Bromley R.D.F., Thomas C.J., Tallon, A.R., 2005. City centre regeneration through residential development: Contributing to sustainability. *Urban Studies*, 42 (13), 2407-2429.
- [3] Shen L.Y., Ochoa, J.J., Shah, M.N., Zhang, X.L., 2011. The application of urban sustainability indicators – A comparison between various practices. *Habitat International*, 35 (1), 17-29.
- [4] Ebdon C., Landow P., 2012. The Balancing Act: Using Private Money for Public Projects. *Public Budgeting & Finance*, 32 (1), 58–79.
- [5] Lizarralde G., Root D., 2008. The informal construction sector and the inefficiency of low cost housing markets. *Construction Management & Economics*, 26 (2), 103-113.
- [6] Pheng L.S., Chuan Q.T., 2006. Environmental factors and work performance of project managers in the construction industry. *International Journal of Project Management*, 24 (1), 24-37.
- [7] Gundes S., 2011. Exploring the dynamics of the Turkish construction industry using input–output analysis. *Construction Management & Economics*, 29 (1), 59-68.
- [8] Tam V.W.Y., Tam C.M., 2006. Evaluations of existing waste recycling methods: A Hong Kong study. *Building & Environment*, 41(12), 1649-1660.
- [9] Wang W., Zhao G.J., Bi X., 2008. Sustainability Assessment System of Engineering Project. *Journal of Tianjin University (Social Sciences)*, 10(2),122-125.
- [10] Abidin N.Z., 2010. Investigating the awareness and application of sustainable construction concept by Malaysian developers. *Habitat International*, 34 (4), 421-426.
- [11] Tang T., 2011. The benefit analysis of the villages' reconstruction in Guangzhou City. M. Thesis, South China University of Technology, Guangzhou, China,58-64.
- [12] Catalina T., 2012. Local experiences of urban sustainability: Researching Housing Market Renewal interventions in three English neighborhoods. *Progress in Planning*, 78, 101-150.
- [13] Peng Y., Lai Y., Li X., Zhang X., 2015. An alternative model for measuring the sustainability of urban regeneration: the way forward. *Journal of Cleaner Production*, 109, 76-83.
- [14] Xia B., Chen Q., Skitmore M., Zuo J., Li M., 2015. Comparison of sustainable community rating tools in Australia. *Journal of Cleaner Production*, 109, 84-91.
- [15] Hemphill L., McGreal S., Berry J., 2002. An aggregated weighting system for evaluating sustainable urban regeneration. *Property Research*, 19(4), 353-373.
- [16] Tam V.W., Tam C., Zeng S., Chan K., 2006. Environmental performance measurement indicators in construction. *Building and Environment*,41(2): 164-173.
- [17] Lee G.K.L., Chan E.H.W., 2008. The Analytic Hierarchy Process (AHP) Approach for Assessment of Urban Renewal Proposals. *Social Indicators Research*, 89(1), 155-168.

- [18] Deng K.Q., 2011. The Sustainability Assessment of Different Models for Urban Renewal – A Case of Guangzhou. Ph.D. thesis, Huazhong University of Science and Technology, Wuhan, China, 44-45.
- [19] Liu J.J., 2014. Study on the Comprehensive Evaluation System of the Old City Reconstruction. M. Thesis, Wuhan University of Technology, Wuhan, China, 27-29.
- [20] Boulanger P.M., 2016. Sustainable development indicators: a scientific challenge, a democratic issue. S.A.P.I.EN.S, [Online], Available from internet: <http://sapiens.revues.org/166>, access: 30. September 2016
- [21] Commission on Sustainable Development (CSD), 2001. Indicators of Sustainable Development: Guidelines and Methodologies. [Online], Available from internet: <http://www.un.org/esa/sustdev/natlinfo/indicators/indisd/indisd-mg2001.pdf>
- [22] United Nations (UN), 2007. Indicators of sustainable development: guidelines and methodologies. [Online], Available from internet: <http://www.un.org/esa/sustdev/natlinfo/indicators/guidelines.pdf>
- [23] Ministry of Housing and Urban-Rural Development of the People's Republic of China (MOHURD), 2016. [Online], Available from internet: http://www.mohurd.gov.cn/wjfb/201605/t20160530_227652.html
- [24] Singh R.K., Murty H.R., Gupta S.K., Dikshit A.K., 2009. An overview of sustainability assessment methodologies. *Ecological Indicators*, 9(2), 189-212.
- [25] Tasaki T., Kameyama Y., Hashimoto S., Moriguchi Y., Harasawa H., 2010. A survey of national sustainable development indicators. *International Journal of Sustainable Development*, 13 (4), 337-361.
- [26] Zhao Y.J., 2010. Study of the Games in Urban Village Reconstruction and its benefit evaluation. M. Thesis, Jianshu University, Jinan, China, 34-39.
- [27] Boyle L., Michell K., 2017. Urban facilities management: A systemic process for achieving urban sustainability. *International Journal of Sustainable Development & Planning*, 3, 446-456.
- [28] Xue Z.Y., 2013. The Analysis of Sustainable Development Indicators in 31 Provinces of Mainland China. *Economic Research Guide*, (4), 148-151.
- [29] Cheng Q.Y., 2010. Structure Entropy Weight Method for Weight Determination of Evaluation. *Systems Engineering Theory & Practice*, 30(7), 1225-1228.
- [30] Tesfamariam S., Saatcioglu M., 2008. Seismic Risk Assessment of RC Buildings Using Fuzzy Synthetic Evaluation. *Journal of Earthquake Engineering*, 12 (7), 1157-1184.
- [31] Zhang M. L., Yang W. P., 2012. Fuzzy Comprehensive Evaluation Method Applied in the Real Estate Investment Risks Research. *Physics Procedia*, 24(C), 1815-1821.
- [32] Sadiq R., Rodriguez M.J., 2004. Fuzzy synthetic evaluation of disinfection by-products: a risk-based indexing system. *Journal of Environmental Management*, 73 (1), 1-13.
- [33] Xu Y.L., Yeung J.F.Y., Chan A.P.C., Chan D.W.M., Wang S.Q., Ke Y.J., 2010. Developing a risk assessment model for PPP projects in China – A fuzzy synthetic evaluation approach. *Automation in Construction*, 19(7), 929-943.
- [34] Aron Arthur, Aron Elaine N., 2002. *Statistics for the behavioral and social sciences: A brief course*. New York: Prentice Hall, 176-194.
- [35] Kaiser Henry F., 1974. An index of factorial simplicity. *Psychometrika*, 39(1):31-36.
- [36] Tabachnick B.G., Fidell L.S., 2007. *Using Multivariate Statistics*. Instructor, 43(21), 3867-3877.

EXPERIMENTAL EVALUATION OF CALCIUM CHLORIDE POWDER EFFECT ON THE REDUCTION OF THE PAVEMENT SURFACE LAYER PERFORMANCE

*Seyed Ahmad Almasi and Mohammad Mehdi Khabir**

*Yazd University, Faculty of Civil Engineering, Highway and Geotechnique Department, Yazd, PO Box: 89195-741, Iran; s.a.almasi110@gmail.com; [*mkhabiri@yazd.ac.ir](mailto:mkhabiri@yazd.ac.ir)*

ABSTRACT

Some roads have a gravel layer and most asphaltic roads have gravel shoulder and part of that sand is fine grained soil. Road dust increases in heavy traffic and affects safety, economy, quality and environment. Different stabilizers are used to control the dust in gravel topping roads. One of them is calcium chloride. One of its common uses is the dust control in gravel topping roads. In this research, in order to achieve the optimal mixture procedure after grading the gravel material of pavement surface layer, the effect of calcium chloride salt on the physical properties of the fine grained part was investigated in different percent of calcium chloride samples and different percent of moisture in two dry cases. Results show that increasing the calcium chloride percent in the dry case, the moisture absorption amount of the fine grained part of the gravel topping materials is increased, by contrast, uniaxial tensile and compressive strengths decrease with the increase of calcium chloride more than certain percent. The amount of calcium chloride has a reverse effect on liquid limit, plasticity limit and plastic index, conversely, uniaxial tensile and compressive strengths such that increasing the calcium chloride salt by 6% will increase the plastic limit by 6% and the liquid limit by 12% and plastic index by 25% and also the uniaxial tensile strength is increased by 11% and the uniaxial compressive strength is decreased by 36%.

KEYWORDS

Road pavement; Axial strength; Calcium chloride; Moisture absorption; Gravel surface layer

INTRODUCTION

Land transport systems, especially roads, play an important role in economic and social development. The lowest traffic and rural roads are important roads for some industries and factories, farmers and stockbreeders they can be used for transporting raw materials and products and are made of gravel surface layer. These roads are mostly considered as the lowest level of facilities and most governments provide a cover for these roads in order to provide better services for the villagers. One of these methods is the use of calcium chloride and magnesium chloride solution in roads and passages to reduce dust. Due to the availability of these minerals in the desert, there is the ability to use these materials to avoid the costs imposed on the transportation system, as well as to protect the environment and sustainable development of roads.

The project of roads change has been performed in 27 states of USA. Most of the roads are changed into unpaved ones in these 27 states are subjected to a mean daily traffic volume in a range of 21 to 100 vehicles [1]. Disregarding the problems of the unpaved roads may lead to public dissatisfaction and reduction of exploiting amount and also high costs and cause some problems for creatures from safety aspect [1]. Dust is increased by the increase of traffic that affects the vehicles driving conditions and endangers them [2]. In order to control the dust, stabilizers are used and calcium chloride is one of them. Calcium chloride is the salt of calcium and chlorine that behaves as the halide ion sample and it is in solid state at room temperature. Since this substance is sensitive to moisture, it is kept in containers [3]. Usually calcium chloride is used for snow and

ice melting at passageways and mountainous roads in winter; soil roads dust control, soil stabilization of desert zones, gas and oil industries and accelerating concrete in winter season [4]. Calcium chloride and magnesium chloride are both capable to absorb the air moisture.

Calcium chloride can absorb moisture up to 17 times more than its weight at a relative humidity of 95%. Among the environmental advantages of the use of calcium chloride and magnesium chloride solution, we can mention its capability to control the dust, reduce the respiratory disease, increase visibility and accidents reduction, reduce the road and vehicles maintenance cost (in such a way that has avoided the creation of bump and damage to the roads infrastructure), solve the problems of the road side inhabitants, improve the quality of agricultural products. Thus it is quite natural and the constituents of this solution are not harmful for the environment [4]. Shukla et.al funded that, the mixing of potassium chloride growths the unconfined compressive strength and shrinkage limit of soil. Best quantity of potassium chloride is found to be almost 8-9% of dry soil mass [5]. In previous study, Saberian and Khabiri examined the effect of ordinary Portland cement on the strengths and plasticity of soil contaminated with diesel [6]. The Oil Palm Fronds (OPF), which is a waste material, was used to stabilize the lateritic soil by Nnochiri, and Aderinlewo [6].

Khabiri et al. have investigated in their research the effect of calcium chloride salt on the fine grained physical properties in different percent of calcium chloride and different percent of moisture in two dry cases in order to reach the optimum admixture procedure. Results showed that by increasing the percent of calcium chloride in dry condition, the moisture absorption capability of the fine grained part of the gravel surface layer is increased. This moisture increase can be up to 80%. Furthermore, the amount of calcium chloride has a negative effect on the liquid limit I , plastic limit and plastic index such that increasing the calcium chloride salt by 6%, the plastic limit, liquid limit and plastic index have increased respectively by 6, 12 and 25 percent [8]. Latsford et al. have investigated the road gravel surface layer in the USA in their research. Their study shows that almost 40% of USA roads have gravel surface layers. They used a type of clay stabilizer based on the traffic volume in order to control the dust on the surface of these roads [9].

Echt et al. have investigated the amount of produced dust due to drilling and respiratory problems faced by workers in a research. They have found by measuring the amount of dust in a case study in drilling that the maximum volume of the produced dust is due to quartz. After adding silica additive they have concluded that this additive significantly reduces the ambient dust [10,11]. Wood et al. in their research to control the wastes resulted from hot asphalt recovery and substituting these wastes by sand concluded that calcium chloride reduces the dust that is resulted from the extra addition of sand to asphalt on the roads surface [11,12].

Prasad et al. investigated different types of stabilizers of soils in their study. These stabilizers can be of solid wastes that can improve stability, durability and moisture absorption of soils. They concluded that the grit and calcium chloride waste additive can lead to soil stability [13]. Silac et al. have investigated the effects of plants ash and calcium chloride on the soil stability in a research. They concluded that calcium chloride is very efficient in controlling the dust. Also in researches that were performed in Texas transportation institute, it was shown that the mixture of calcium chloride and plant ash change the physical and chemical nature of this mixture and improves roads performance [14].

One of the problems of gravel surface layer roads, dust stabilizers is that they are rain-washed. In the studies that were performed on stabilizers, the results showed that calcium chloride removes a part of clay. Thus, it avoids its saturation under moisture [15]. More than 50% of USA roads are sand surface layer roads and they know them as a vital section of the transportation system. One of the biggest disadvantages of gravel roads is dust that is imposed to them on the vehicle transportation time. Inhabitants that live near gravel roads surface problems such as dust that is settled on their houses and cars and this decrease their life quality. Dust can also have undesirable effects on the air and environment quality and reduce safety (visibility disturbance) for the drivers. In order to control dust in gravel roads, local organizations use dust stabilizers on their

roads that are usually calcium chloride and magnesium chloride but there are some other substances [16].

There are many ways for soil stabilization that one of their most important ones is the use of electrolytes for the dust control. Venkara performed some tests on electrolytes such as calcium chloride and potassium chloride [17]. Bahari et al. investigated clay nanocomposite material with 1% weight ratio with the considered area soil in their research. By performing uniaxial compressive strength and consolidation tests on the soil, it was observed that by adding Nano clay to the soil, the amount of shear strength, adherence and compressibility of soil are increased [18]. In researches that have been performed under the name of "effectiveness and environmental effects of road protective material" in Colorado State of the USA, the following results are derived:

- The type of stabilizers is effective on the amount of runoff or the road surface affect after raining.
- By increasing the vehicle speed, the produced dust in the road is increased.
- It seems that using Lignum stabilizers in some cases is more effective than calcium chloride and magnesium chloride stabilizers [16,17].

In any cases few researcher have focused on the issue of calcium chloride powder effect on the reduction of dust emissions of the pavement surface layer.

The purpose of this study is to investigate the effect of calcium chloride amount on the soil engineering properties and also this salt effect on the compressive and tensile strength of soil in gravel surface layer roads. Regarding the research process, physical and mechanical tests were carried out on soils containing calcium chloride. These tests include identification of soil plasticity properties and the effect of calcium chloride on these soil characteristics, and since the top granular layer is under the loading of the vehicle's wheel, its resistance to damage were also investigated by laboratory tests.

MATERIALS AND METHODS

Calcium chloride whose natural type is salt is available in sea water and can be extracted from salt bed in nature. Oromiyeh Lake is one of the biggest lakes in the world. The salt of Oromieh Lake is composed of minerals such as potassium, calcium, magnesium and many other minerals [8]. The chemical component and formula of calcium chloride is found in nature in the forms presented in table 1[14].

Tab. 1 - Calcium chloride compounds available in nature and their molar mass [14]

Name	Chemical components	Molar mass(gr/mole)
Calcium dichloride	Cacl ₂	110.99
Calcium chloride dihydrate.	Cacl ₂ .2H ₂ O	147.02
Calcium chloride tetrahydrate	Cacl ₂ .4H ₂ O	183.04
Calcium chloride hexahydrate	Cacl ₂ .6H ₂ O	219.08

Determination of the soil properties

In order to determine the properties of the soil, two tests were performed on the samples:

- a) Plastic limit test is the moisture percent in which sample is at the beginning of plasticity, in other words it is the intermediate point between plastic and semi-solid states (ASTM D4318 - 17 Standard Test Method).

b) Liquid limit test, is the boundary between plastic and liquid states and is the moisture percent in which soil has a little shear strength. In other words, the sample moisture content at the beginning of liquid limit (ASTM D4318 - 17 Standard Test Method).



Fig. 1 - Used calcium chloride salt in the experimental tests

Studies show that calcium chloride salt helps in water absorption by the soil [8]. During the Atterberg limit test, the residual of the soil that was mixed with different percent of calcium chloride salt was wetted after some time that shows the ambient moisture absorption by soil. Also the test showed that calcium chloride salt reduces the tensile and compressive uniaxial strength (ASTM D2166 / D2166M - 16) and also by increasing the percent of calcium chloride salt in the soil, the adherence between the soil particles become less and the unoccupied volume will be more. In order to achieve these results, soil samples with different percent of 0, 2, 4, 6 of calcium chloride was compressed in this study and then was subjected to tensile and compressive uniaxial test.



Fig. 2 - Samples compression and Soil Sampler test



Fig. 3 - Compressed Soil Sample for UCS

Atterberg limit and soil moisture absorption

The Atterberg limits are a simple measure of the critical water fillings of a fine-grained soil, its shrinkage limit (SL), plastic limit (PL), and liquid limit (LL). In Figure 4, the results of the liquid limit and plasticity limits with different percent of calcium chloride salt are presented. Figure 4 shows that there is a reverse proportion between the salt percent and the soil liquid limit and by adding calcium chloride to soil; the liquid limit and plasticity of soil are reduced.

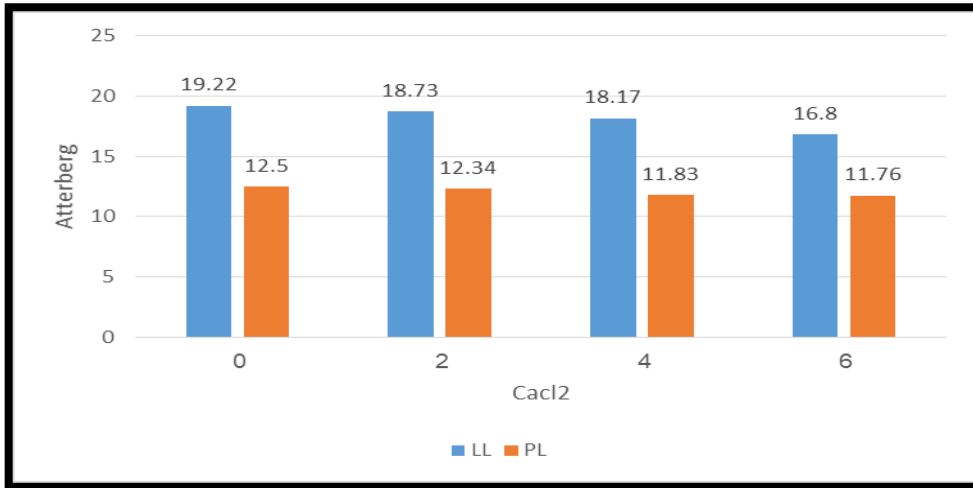


Fig.4 - Comparison of soil liquid limit and plasticity effect for different percent of calcium chloride salt

A definite amount of fine grained soil of road gravel surface layer that has been passed through sieve and combined with different amounts of calcium chloride including 0, 2, 4, 6 weight percent and put for 3 hours in the furnace. After 3 hours, the samples have been taken out of the furnace and the weight of each was measured and the specimens were subjected to ambient moisture for 48 and 72 hours in the laboratory.

The results show that the increase of calcium chloride amount will increase the amount of moisture absorption and also the time increase from 48 to 72 hours lead to a 35% increase in the moisture absorption.

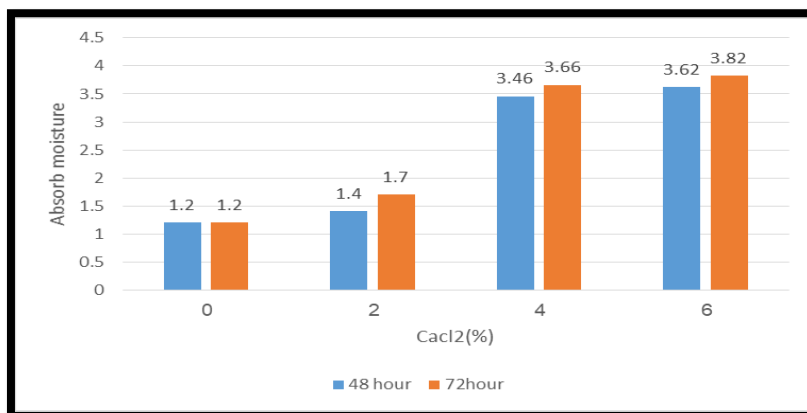


Fig.5 - Results of the soil moisture absorption for different percent of 48 and 72 hours' calcium chloride

Figure 6 shows that there is a direct relation between the moisture absorption and salt increase. By increasing the salt amount, the moisture absorption is increased and this moisture absorption is observable up to 90 percent compared to the typical soil.

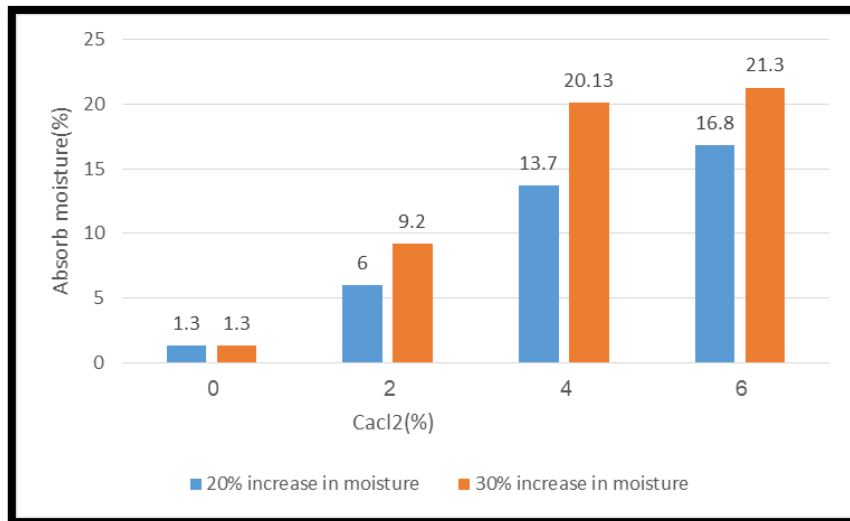


Fig.6 - Results of soil moisture absorption for different percent of calcium chloride

Unconfined compression and indirect tension tests

By increasing the calcium chloride salt percent, the required strength for the vertical and horizontal deformations of specimens is reduced. Thus it can conclude that the increase of calcium chloride salt percent leads to a reduction in the soil strength and accelerates the soil rupture.

Tab. 2 - Comparison of the required strength amount for the soil deformation at different percent of salt

Displacement (0.1 millimeter)	Strength (Kn) Unconfined Compression			
	CaCl ₂ (0%)	CaCl ₂ (2%)	CaCl ₂ (4%)	CaCl ₂ (6%)
5	0.1188	0.066	0.066	0.0396
10	0.2376	0.1188	0.1188	0.066
15	0.3036	0.1518	0.1254	0.0924
20	0.33	0.1716	0.132	0.1188
Strength (Kn) - Indirect Tensile Test				
5	0.0924	0.0396	0.0264	0.0132
10	0.1716	0.1056	0.066	0.0198
15	0.2112	0.1254	0.0792	0.0264
20	0.2376	0.132	0.0792	0.0264

Figure 7 shows that the increase in the calcium chloride salt will reduce the horizontal and vertical uniaxial strengths for the specimen rupture. This decrease in strength can be due to the reduction of adherence amount between the soil particles and the increase of free space (void) in the soil. Such that by an 4% increase of the calcium chloride salt, the vertical strength of the specimen for 0.5mm and 2mm displacements reduced respectively by 40% and 31% and the

specimen horizontal strength in 0.5mm and 2mm displacements reduced respectively by 66% and 80%.

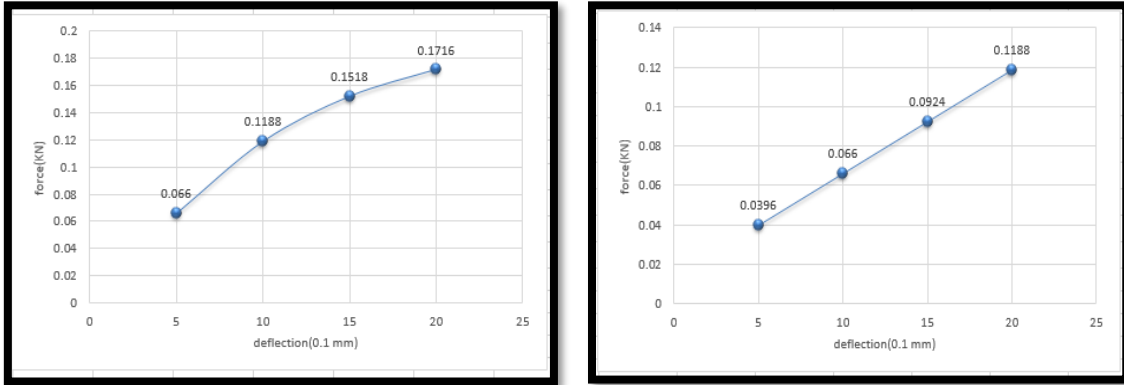


Fig.7 - Uniaxial test of 6% calcium chloride (right) uniaxial test of 2% calcium chloride (left)

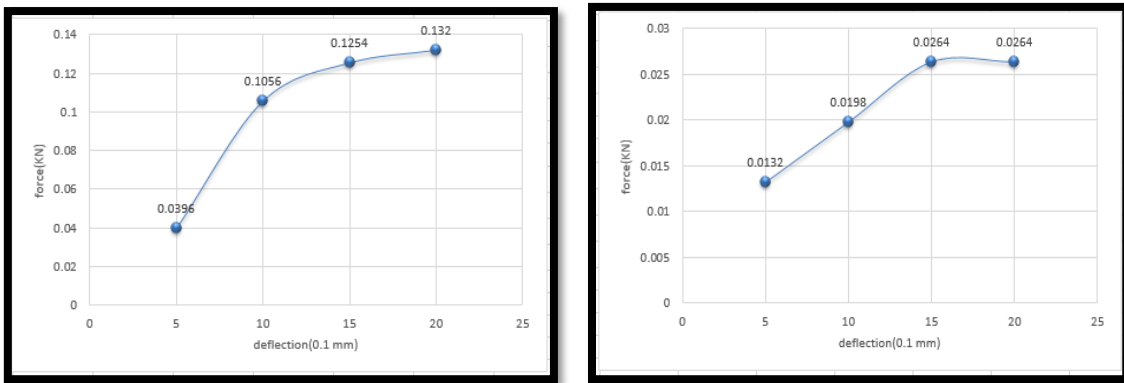


Fig.8: Indirect tension test of 6% calcium chloride (right) Indirect tension test of 2% calcium chloride (left)

Figures 9 and 10 show the results of the vertical and horizontal strength tests at different percent of calcium chloride and different displacements.

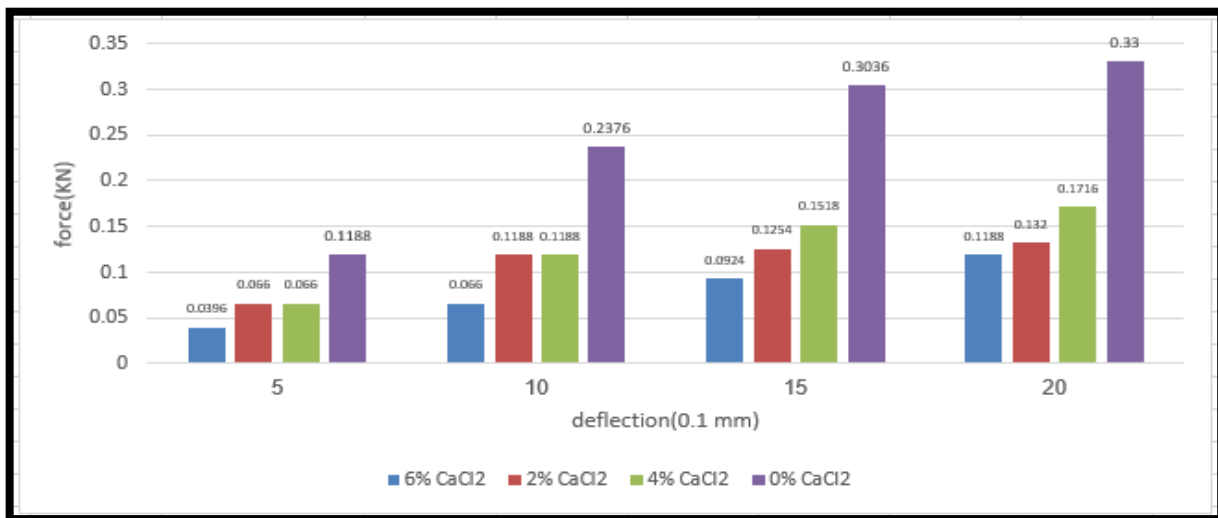


Fig.9 - Comparison of unconfined compression test results

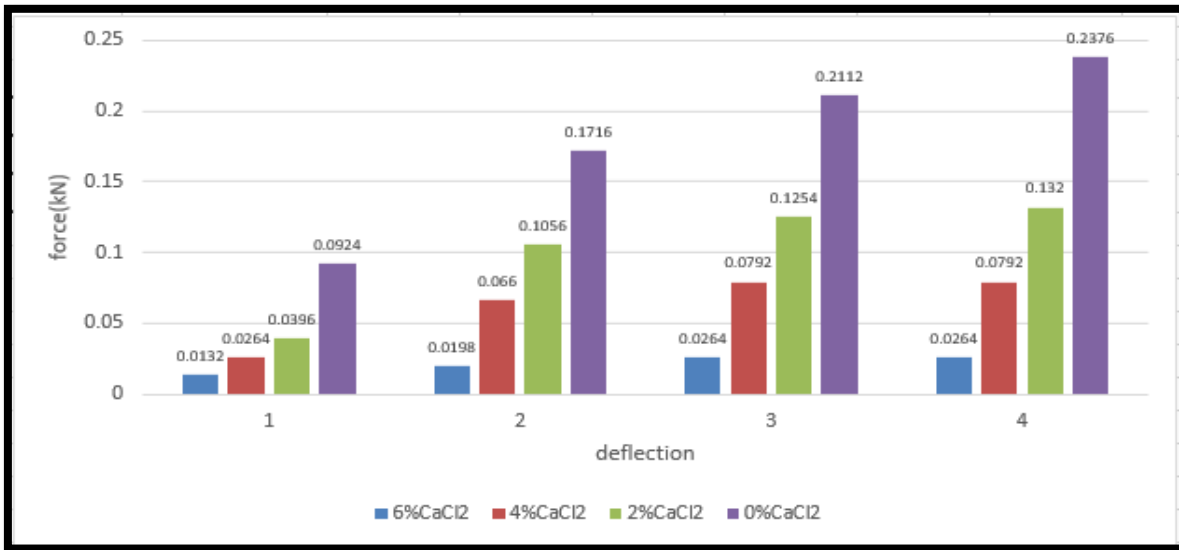


Fig.10 - Comparison of indirect tension test results

Fracture energy in unconfined compression and indirect tension tests

Figures 11 and 12 show that by increasing the percent of calcium chloride in the soil, the area surrounded under the diagram is reduced. Thus the fracture energy has been reduced in the case in which the specimen is subjected under indirect tensile loading and unconfined compression loading. Hence the soil strength is decreased and ruptures at a shorter time and by a small strength.

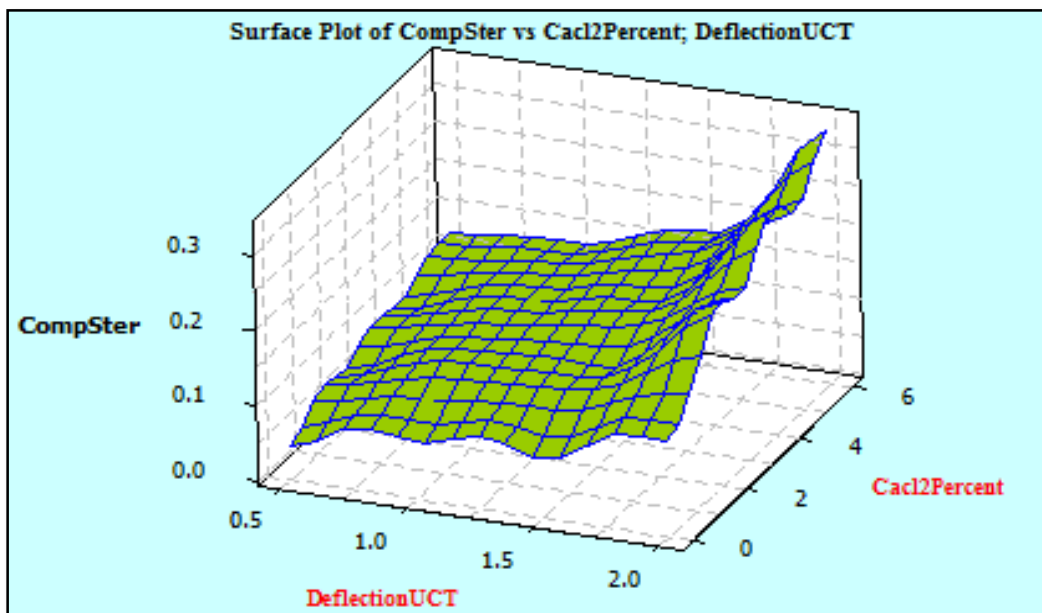


Fig.11 - The area surrounded under diagram for the unconfined Compression test with various percent of calcium chloride

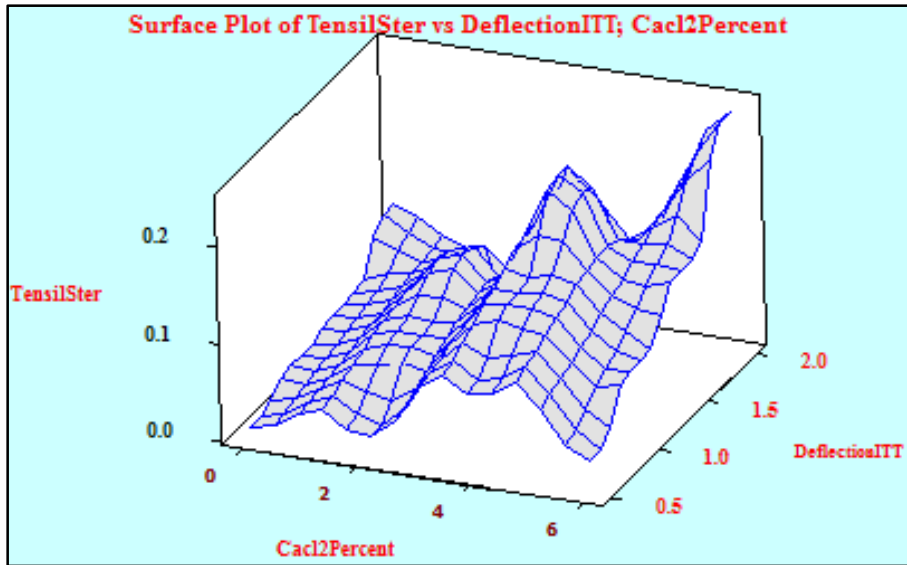


Fig.12 - The area surrounded under diagram for the indirect tension test with various percent of calcium chloride

DISCUSSION OF RESULTS

Large-scale images can display the interior properties of the soil with calcium chloride additive. According to Figure13, by increasing the amount of calcium chloride, as is observable, the amount of adherence between the soil particles is decreased and the void is increased, as calcium chloride leads to greater moisture absorption and adherence between the particles has become unbalanced.

Figure 14 shows propagation of cracks in the soil sample in two different loading conditions. Table 3 shows the comparison between the area below the stress-strain diagrams, as the calcium chloride increases, this area decreases, in other words, the fracture energy decreases. Consequently, it is suggested that this salt be added to the soil with additional mixture such as plant ash.

Tab. 3 - Comparison of the area under the strength-displacement at different percent of calcium chloride

Different percents of Cacl ₂	Integral Of Indirect Tensile Test	Integral Of Unconfined Compression Test
0	2.97	4.17
2	1.68	2.11
4	1.05	1.88
6	0.36	1.28



Fig.13 - Investigation of the free space amount at different percent of calcium chloride



Fig.14 - The style of specimens fracture under indirect tension and unconfined compression test

CONCLUSION

The purpose of this study is to investigate the effect of calcium chloride amount on gravel roads, based on the soil tests, and this previously discussed research. There is a reverse proportion between the salt percent and the plastic limit and liquid and plastic index of soil and adding calcium chloride salt to soil reduces the plastic limit and liquid limit. Such that increasing the salt percent up to 6% the plasticity limit, liquid limit and plastic index are respectively reduced by 6-12-25 percent. The addition of calcium chloride to soil increases the absorption of soil moisture and soil will be wet but test conditions are of high importance in the effect of calcium chloride salt on soil such that if the test is not performed under suitable conditions, there would be a difference of about 80% between the results. Due to the addition of calcium chloride salt in the soil, it decreases soil strength and causes it to rupture under a smaller strength than the regular case. Thus, it is recommended that this salt be added to the soil with another mixture such as plant ash. Also, the addition of calcium chloride salt in the soil causes reduce the area under the strength - displacement curve, in other words, the soil sample has a more restrictive effect.

Civil engineering researchers need to continue conducting full-scale tests to determine the factors that contribute to adding calcium chloride salt performance in unpaved road.

ACKNOWLEDGEMENTS

It is necessary to thank Eng. Alaei, her expert specialized project report in the subject area as the basis for the research and the equipment used. We thank our colleagues Dr.Morshed and Eng. Khajeh who provided insight and expertise that greatly assisted the research. It is also grateful to researchers whose research results have been used in this study.

REFERENCES

- [1] Laura F., Ashley K.,2016 "Converting Paved Roads to Unpaved". Transportation Research Board Blurbs. Recently Released TRB Publications,2016. TRB's National Cooperative Highway Research Program (NCHRP) Synthesis 485,pp:89, DOI 10.17226/21935.
- [2] Trombulak, S.C. and Frissell, C.A., 2000. Review of ecological effects of roads on terrestrial and aquatic communities. *Conservation biology*, 14(1), pp.18-30 ,DOI.10.1046/j.1523-1739.2000.99084.x.
- [3] David R. Lide (Editor),1990, Handbook of Chemistry and Physics, 71st edition, CRC Press,1990, 2392 pages, ISBN-10: 0849304717.
- [4] Bortoluzzi, E.A., Broon, N.J., Bramante, C.M., Felipe, W.T., Tanomaru Filho, M. and Esberard, R.M., 2009. The influence of calcium chloride on the setting time, solubility, disintegration, and pH of mineral trioxide aggregate and white Portland cement with a radiopacifier. *Journal of endodontics*, 35(4), pp.550-554. DOI;/10.1016/j.joen.2008.12.018
- [5] Shukla,R.P. , Parihar,N.S. and GuptaA.K., 2018,Stabilization of expansive soil using potassium chloride, THE CIVIL ENGINEERING JOURNAL, 1-2018, Article no. 3 ,pp:25-33. DOI 10.14311/CEJ.2018.01.0003.
- [6] Saberian, M., and Khabiri, M. M. ,2018, Effect of oil pollution on function of sandy soils in protected deserts and investigation of their improvement guidelines (case study: Kalmand area, Iran). *Environmental geochemistry and health*, 40(1), pp:243-254. DOI 10.1007/s10653-016-9897.
- [7] Nnochiri,E. and Aderinlewo,O., 2016,Geotechnical properties of lateritic soil stabilized with the ashes of oil palm fronds, THE CIVIL ENGINEERING JOURNAL, 4-2016, Article no. 22, pp:1-8. DOI 10.14311/CEJ.2016.04.0022
- [8] Khabiri,M.M. , Almasi,S.A. 2017, experimental investigation of the effect of calcium chloride mix method in the optimum control of dust in roads improvement, second international conference of modern materials and structures, Yazd University,PP;1-10,ISC.
- [9] Echt, A. and Mead, K., 2016. Evaluation of a Dust Control for a Small Slab-Riding Dowel Drill for Concrete Pavement. *Annals of Occupational Hygiene*, 60(4), pp.519-524,DOI. 10.1093/annhyg/mev099

- [10] Wood, T.J., Johnson, E.N. and Cole, M.K., 2014. Research Using Waste Shingles for Stabilization or Dust Control for Gravel Roads and Shoulders ,No. MN/RC 2014-06, Department of Transportation, Research Services & Library.48p. A.N: 01522311.
- [11] Ayambem, A., Kent, D.B. and Dobson, J.C., Henry Company, Llc, 2017. Novel asphalt-based dust control formulations. U.S. Patent Application 15/421,550, US20170166792A1.
- [12] Prasad, A.S.S.V. and Babu, R.D., 2015. Efficiency of Calcium Chloride and Vitrified Tiles Sludge on the Strength Characteristics of Expansive Soil. International Journal of Advanced Research in Education & Technology (IJARET), ISSN:2394-2975,Vol. 2(3), pp.202-205.
- [13] Saylak, D, 2014, Fly Ash-Calcium Chloride Stabilization in Road Construction, Transportation Research Record: Journal of the Transportation Research Board, DOI:10.3141/2053-04.
- [14] Edvardsson, K. and Magnusson, R., 2011. Impact of fine materials content on the transport of dust suppressants in gravel road wearing courses. Journal of materials in civil engineering, 23(8), pp.1163-1170. DOI:10.1061/(ASCE)MT.1943-5533.0000282.
- [15] Marti, M., and Renae K.I. 2013,Aggregate Roads Dust Control: A Brief Synthesis of Current Practices. No. MN/RC-2013RIC67. 40p. AN: 01522383.
- [16] Muthyalu, P.V., Ramu, K. and Raju, G.P., 2012. Study on performance of chemically stabilized expansive soil. International Journal of Advances in Engineering & Technology, ISSN: 2231-1963, 2(1), pp.139-148.
- [17] Sanders, T.G. and Addo, J.Q., 1993. Effectiveness and environmental impact of road dust suppressants, No. MPC-94-28, Colorado State University, Department of Civil Engineering.46p. AN: 00669201.
- [18] Bahari,M.Shahnazari,A. 2015, Experimental investigation of the fine grained soil bed stabilization by using Nano clay, Journal of agriculture and natural resources sciences and technologies, water and soil sciences, ISSN: 2476-3594, 19th year, Summer,No.72.pp:107-113.

STUDY ON THE INTERACTION BETWEEN FORMWORK SHORING SYSTEMS AND RC STRUCTURES IN A HIGH-RISE BUILDING DURING CONSTRUCTION 2

Suchun Yang, Chengping Qu and Heng Yang

*Qingdao University of Technology, School of Civil Engineering, Qingdao, China;
18560609732@qq.com; 215437245@qq.com; hengyoung@qq.com*

ABSTRACT

In the construction process of high-rise building structure, the formwork temporary supports and the concrete structure are considered as a whole. Quantifying the load under the template supports can provide a better reference for the design of the template supports. In order to study the load transfer law between formwork support scaffolds and multi-storey structure, through the installation of sensors at the bottom of formwork supports and the floor slab, the load transfer law of the 3 adjacent formwork supports were monitored for a long time during the construction of high-rise buildings via the high-frequency wireless transmission systems. The main conclusions are as follows: (1) The monitoring data shows that the most unfavourable load occurs when concrete is poured into the upper story, about 1.9 times the axial force generated when concrete is poured into the test floor. (2) The monitoring data has a similar shape which is summed up as an ideal curve of change, 3 times of peak value, 3 times of decline and 1 time of sudden drop. (3) The transfer ratio of load accounts for about 57% ~ 69% of a total load of fresh concrete. (4) Considering the fluid-plastic state of concrete, a correction factor of 1.22 for vertical pole axial force is proposed, and the deviation between the modified simulated value and the measured value is less than 3%.

KEYWORDS

Formwork; Multistory; Shore; Load transfer law

INTRODUCTION

In recent years, the collapse of the formwork temporary supports has been frequent, which has brought serious economic property losses and casualties and caused a bad social impact. Multistory formwork shoring systems are a complex and huge issue, its arrangement method and form changes with the structural loads and its stability capacity and other factors. As a temporary support structure, it has a complex composition of components, various connection joints and many uncertainties.

So study on the template supports are from different angles. Chan et al. [1], Peng et al. [2-6], Yu [7], and Weesner [8] produced many studies on the stability capacity and design method of door-type scaffolds experimentally and theoretically. Reynolds et al [9-12] studied the influence of various components of the formwork scaffolding system. Timothy P Ambrose et al [13-17] monitor the load of shoring systems and propose a monitoring method. Manuel et al [18] propose a calculation method that allows the loads on individual shores to be calculated for each construction phase without having to resort to the use of advanced software. Mosallam, K et al [19] propose a three-dimensional computer model capable of simulating the concrete construction process is developed. The model accounts for the interaction of gravity and lateral loads and can include temporary lateral bracing elements in the supporting assembly. Qing Rong Tang [20] research for mechanism of concrete structure interacting with formwork support by manufacturing 2 test models

of two-layer and single-span reinforced concrete frame at laboratory, and analysis interaction performance between concrete structure and formwork support and the influence of construction period, curing time of concrete and load on mechanical performance of the formwork support system during the construction period.

We think that formwork temporary supports interact with the building structure to form a time-varying system. The design of multilayer formwork support system is not considered single layer load. There is, therefore, a clear need to carry out more thorough studies on the interaction between formwork shoring systems and RC structures in a high-rise building during construction. It would reveal the load change of the multilayer formwork support system and provide a guarantee for construction safety that carrying out the long-term measurement work of formwork support system.

Engineering Situation

Test high-rise building is located in Qingdao, China. There are 4 floors underground, 25 floors above ground and 2 podium floors. The main building is 96.4m high, which is the frame-core wall system.

The actual measurement of this project involves 11th floor to the 16th floor. The strength of concrete in this interval is: column $f_c'39.5\text{Mpa}$, wall and connecting beam $f_c'31.6\text{Mpa}$, beam board $f_c'23.7\text{Mpa}$, the story height of the test area is 3800mm and the floor thickness is 120mm. It is measured from April 19, 2016, until May 24, 2016, ended in the summer during the test average temperature of 16.5 degrees Celsius. The construction speed of the main structure of the project is 6 or 7 days per floor.

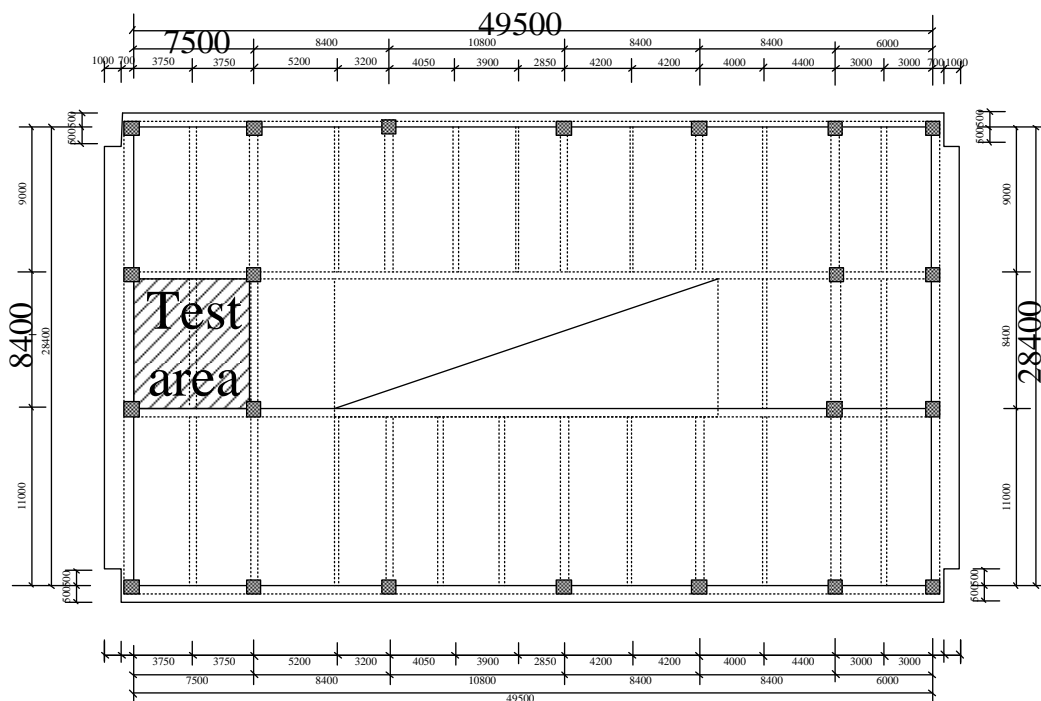


Fig. 1 – Plane layout of structure

Measurement Scheme

The Measurement Content

- (1) Monitoring formwork support system pole axial force changes: select the representative site and layout pressure sensor, continuously monitor pole axial force during the construction cycle includes erecting scaffold - setting template - lashing steel - pouring concrete - conservation concrete from 11 to 13 layers;
- (2) Monitoring changes in floor slab stress: select the cross or support at the reinforced part of the larger force to install steel bar sensor, continuously monitor the steel floor tensile force changes during the construction cycle includes erecting scaffold - setting template - lashing steel - pouring concrete - conservation concrete from 11 to 13 layers;
- (3) Monitoring the concrete strength changes in the corresponding floor: Making a multi-group of same condition test blocks (100 × 100 × 100 mm) and pressing a group of test blocks two or three days interval.

Testing point instructions

In this testing, 10 axial force sensors are arranged at corresponding positions of 11th, 12th, and 13th floors respectively, for a total of 30 pieces; 2 steel bar sensors are arranged at the 11th, 12th floors along the short side of the floors, the measuring point layout plan shown in Figure 2.

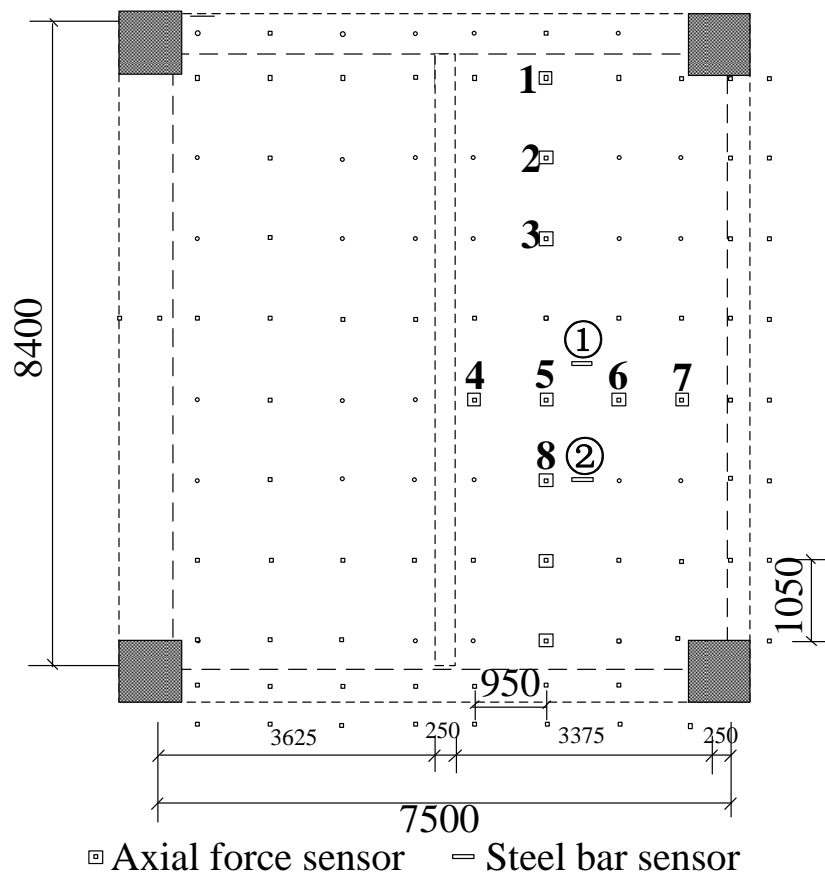


Fig.2 – Arrangement of testing points

Key construction node

The project uses a tubular scaffold with couplers as the template support frame. Tubular scaffold spacing is 950 × 1050mm. In Table 1, the erection scaffold on the 11th floor is regarded as the first day to record the construction of the key construction node.

Tab. 1 - Key construction node

Time (day)	Key events
1	erection scaffold on the 11th floor
2~4	setting template - lashing steel on the 11th floor
5	pouring concrete on the 11th floor
6~10	erection scaffold-setting template - lashing steel on the 12th floor
11	pouring concrete on the 12th floor
12~17	erection scaffold-setting template - lashing steel on the 13th floor
18	pouring concrete on the 13th floor
19	disassembling scaffold and template on the 11th floor
20~24	erection scaffold-setting template - lashing steel on the 14th floor
25	pouring concrete on the 14th floor
26	disassembling scaffold and template on the 12th floor
27~31	erection scaffold-setting template - lashing steel on the 15th floor
32	pouring concrete on the 15th floor
33	disassembling scaffold and template on the 12th floor

Monitoring equipment and installation

The main monitoring equipment and performance are showed in Table 2.

Tab. 2 - Monitoring equipment

name	Introduction
axial force sensors	Vibrating wire axial force sensor, precision is 0.1KN, the range is 20KN
steel bar sensors	Vibrating wire steel bar sensors, precision is 0.1KN, range is 10KN
acquisition system	40 channels, can simultaneously capture 40 sensor data

The installation method:

- (1) Steel bar sensors installation: In order to ensure the test precision, the steel bars to be tested in the slab are cut off, and then both ends of the steel bar are welded and connected to the steel bar, such as Figure 3a. The ends of steel bar sensors should be wrapped with a wet towel before welding to avoid burning the steel bar sensors out due to the over-temperature of welding.
- (2) Axial force sensors installation: The steel plate is placed between axial force sensors and scaffold pole to ensure the centre line of the pole and axial force sensors are in a same vertical line, such as Figure 3b.
- (3) The connection of sensor and acquisition system: After the sensors are installed, the wire of sensors are connected to the collection device, and after the power is turned on, the wireless transmitter inside the collection device can send the received data back to the terminal to complete a collection process, such as Figure 3c.



a. steel bar sensors installation b. axial force sensors installation c. acquisition system
 Fig.3 – Installation of sensors and acquisition equipment

The data transmission

The wireless transmission system, which achieves high-frequency non-stop data, is used to collect on-site sensors data in this measure. Acquisition system consists of sensors, acquisition equipment, and a wireless transmitter, remote end (computer) and analysis software, the consists of data transmission system is shown in Figure 4. The acquisition frequency is set to 20 minutes interval in the actual measurement.

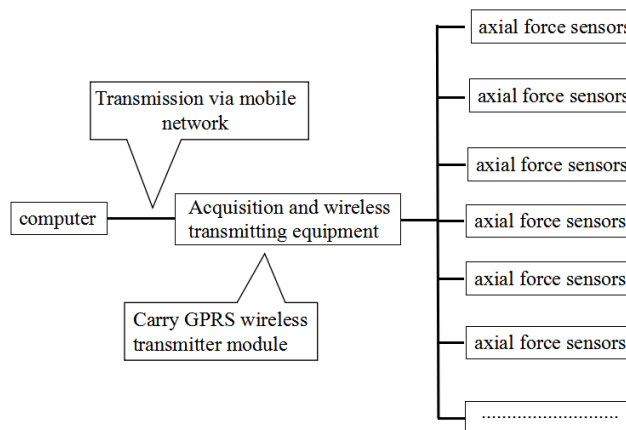


Fig.4 – Sketch map of data transmission

Concrete compressive strength monitoring

The strength and stiffness of concrete is an important variable in the process of load transfer in multilayer formwork support system. In order to monitor the concrete strength in the slab with the growth of age, 40 sets of the same test blocks were placed in the first concrete pouring, and a set of the same conditions test block is pressured every 2 to 3 days to find the average as the representative of the age, the press machine in Figure 5, the representative values are shown in Table 3. Draw the concrete strength growth curve, shown in Figure 6.



Fig.5 – Press machine

Tab. 3 - Strength of same condition test block (MPa)

age	3	6	8	10	12	14	16	19	22
$F_{cu,k}$	21.7	26.4	27.3	29.6	30.1	30.4	31.6	33.2	33.9
percentage	72%	88%	91%	99%	100%	101%	105%	111%	113%

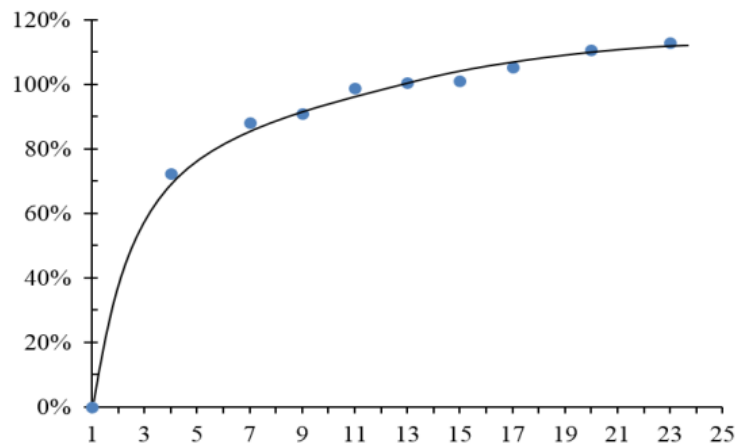


Fig.6 – Concrete strength change curve

Results and analysis of the field test

All data, from the axial force sensors, is analysed after the end of the survey to draw a line chart. The axial force changes in the vertical pole are clearly displayed in these line charts. Figure 7 to 9 are summary of all floors of axial force sensors change line chart, Figures 10 to 19 are the change line chart in the axial force sensors of the representative positions for each layer, of which the axial force sensors 1101, 1201, and 1301 are beam-side poles and the others are the under-floor poles.

The uneven force in the vertical pole

As can be seen from the line chart, the arrangement of the spacing of the vertical pole under the floor is the same, but it appeared obvious as an uneven force. The main reasons for this situation are the characteristics of the tubular scaffold with couplers, the specific reasons are as follows:

- (1) The location is different. The axial force of the vertical pole has nothing to do with the position before the concrete has been poured without strength. But structures began to bear the load autonomously as the strength of concrete, then the deflection in the middle of the structure is the largest which causes a greater force of vertical pole near the midspan. For example, the order of the thirteen-layer pole axial force from small to high order is axial force sensors 1304, axial force sensors 1305, axial force sensors 1306, an axial force sensors 1307;
- (2) The tightness of the U-shaped support at the top of the vertical pole is the main reason of the uneven force of vertical pole. If one U-shaped support at the top of the vertical pole is in a state of relaxation, it will cause the adjacent poles to endure larger load. In fact, even if there is only a slight difference between the heights of the adjacent poles and the top of the U-shaped supports, the force exerted on the pole will be greatly affected;
- (3) The degree of tightness of nodes is different, resulting in differences in the lateral transmission of the axis force, so that the force of the pole is uneven.

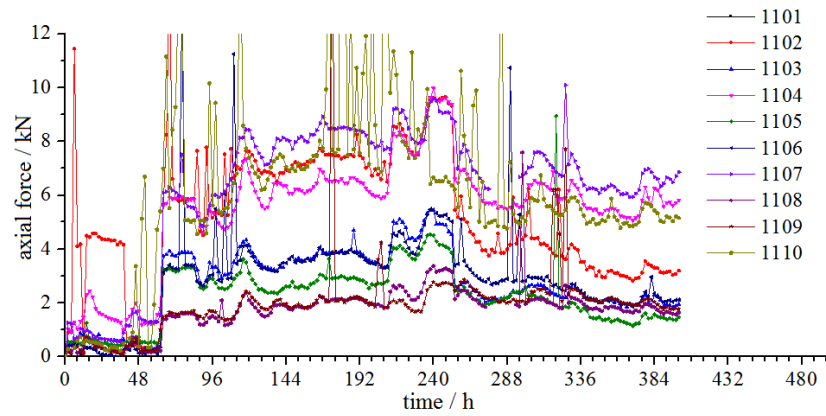


Fig.7 – 11 floor axial force variation of vertical pole

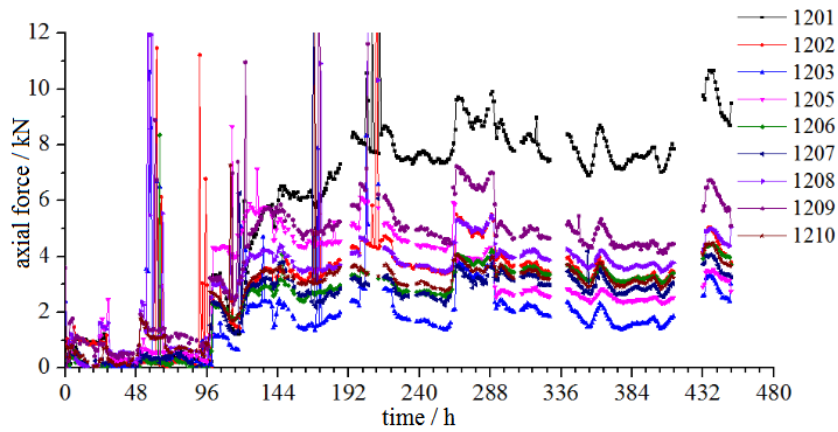


Fig.8 – 12 floor axial force variation of vertical pole

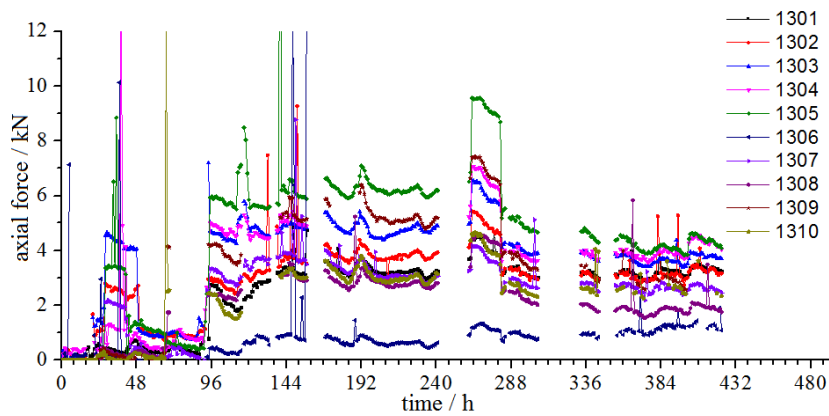


Fig.9 – 13 floor axial force variation of vertical pole

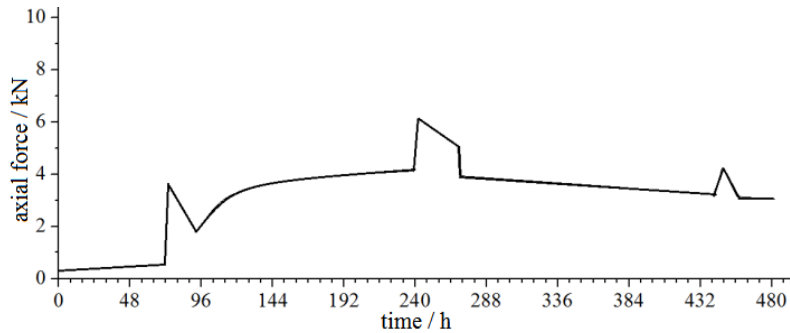


Fig.10 – The axial force of vertical pole ideal simulation figure

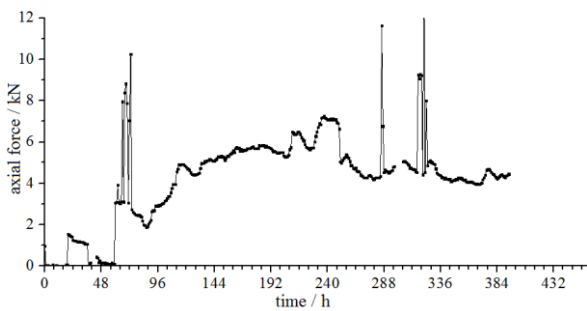


Fig.11 – 1101 axis force variation

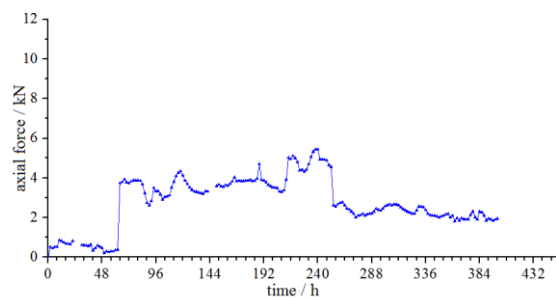


Fig.12 – 1103 axis force variation

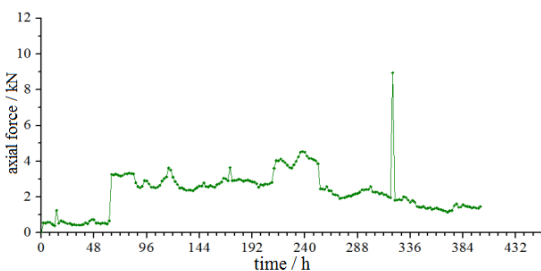


Fig.13 – 1105 axis force variation

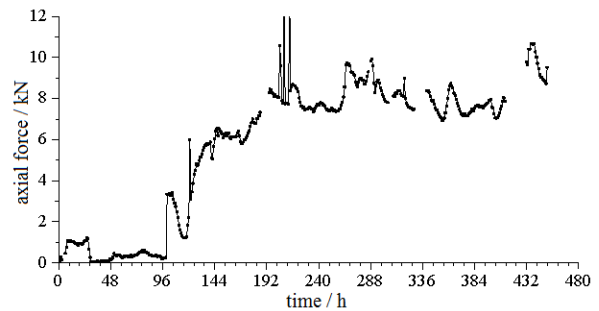


Fig.14 – 1201 axis force variation

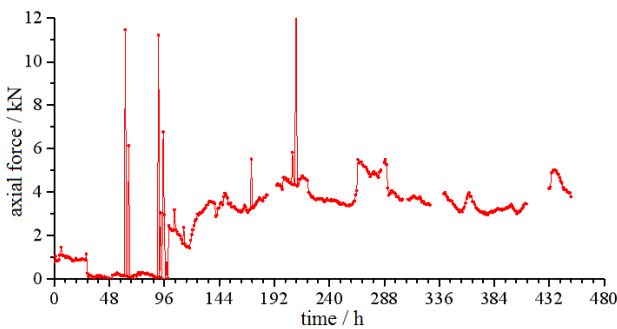


Fig.15 – 1202 axis force variation

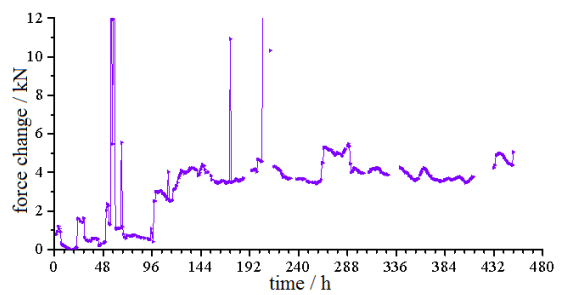


Fig.16 – 1208 axis force variation

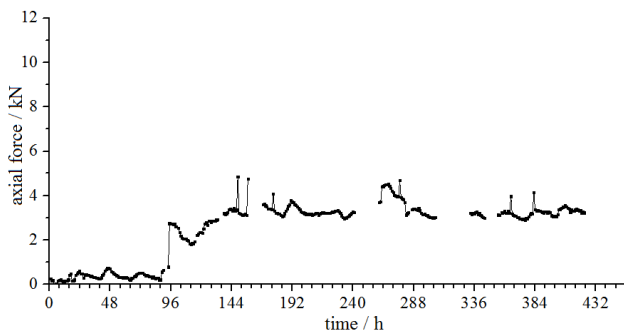


Fig. 17 – 1301 axis force variation

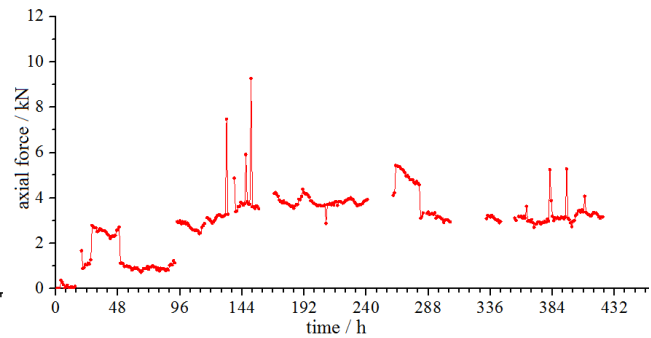


Fig. 18 – 1302 axis force variation

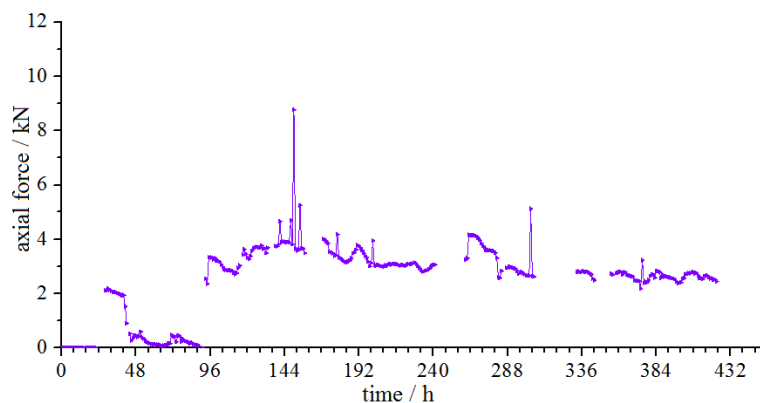


Fig. 19 – 1307 axis force variation

Analysis of pole axial force change process

From Figures 7-19, it can be seen that the axial force of each pole varies greatly due to the influence of live load, and the influence of live load should be eliminated as much as possible during the analysis. The vertical pole force is not uniform but has a uniform law of variation (Figure 10), the process of change and the reasons are summarized as follows:

Before the first pouring of concrete, the axial force increases slowly and slightly. As the support systems of the formwork are set up gradually, the self-weight of the support systems is increasing. In the non-ideal model, it can be seen that there is a large load fluctuation at this stage, which is caused by the live load.

After the first pouring of concrete, the axial force suddenly increased to about 3kN to appear the first peak, which is caused by the weight of concrete. Horizontal structural members deflect when concrete is poured. With the hardening of concrete, horizontal concrete structural members shrink. The vertical resultant force produced by shrinkage of concrete members is the resultant force of the decrease of formwork supports. The axial force of the pole decreases uniformly at a faster rate. After about 8 hours, the axial force of the pole starts to rise slowly again, because, at this time, the upper formwork support systems began to be set up.

After second pouring of concrete, the axial force of the pole appeared the second peak and then decreased again at a faster rate due to the hardening of the concrete, which is similar to the changing law of the first pouring concrete, however, the change is small. In particular, it should be noted that after a certain period of time, the axial force of the pole has dropped greatly, which is mainly caused by the removal of the formwork support systems under the floor where the axial force sensor is located.

Before the third pouring of the concrete, the axial force of the pole in the process of setting up the formwork support systems did not show the phenomenon of "slow increase", which is similar to the previous two times, mainly because the strength of the upper two floors continued to

increase and the pole was continuously unloaded, offsetting the increased constant load. After the third pouring of the concrete, there is still a small peak, and then gradually disappear.

(5) As shown in Figure 11 and Figure 12, comparing the difference of the axial force between the beam-side pole and middle span pole, it is found that the axial force increase between the first and the second pouring concrete is obviously greater than that of the upper formwork support dead weight. This is because as the strength of concrete increases, the stiffness of the slab gradually increases, the force transmission path changes, the beam takes more load, resulting in an increase of the axial force of the beam-side pole.

In summary, the load is shared by all floors, beams and support frame in multi-layer formwork supports system. The axial force has several changes and with the increase of the concrete strength and the process of the construction, the share of the load on the beam and slab and the support frame is also constantly changing. Therefore, the multi-layer formwork supports system is a dynamic integration, the law of force is influenced by a variety of factors. However, the current main calculation method ignores the internal rules of the multi-layer formwork system. It is not advisable to consider only the single-layer formwork in the design and calculation. Through the measurement, we can find that the force transmission of the multi-layer formwork supports system has a regular pattern, which makes it possible to find a more accurate design calculation method.

Quantitative analysis of axial force of support

After statistics and calculation, the axial force of the main pole is shown in Tables 4 ~ 7. Due to the supported layout under the beam is different from the one under the floor, so the data of the pole under the beam is not included.

Load of fresh concrete

The increment of axial force during the first pouring of concrete refers to the difference of axial force before and after pouring concrete, which does not include the self-weight of the formwork support frame and the slab reinforcement, mainly the self-weight of the newly poured concrete. The measured first averaged an increase of the axial force of pouring concrete is 2.80kN, theoretically, the axial force should be $24\text{kN/m}^3 \times 1.05\text{m} \times 0.95\text{m} \times 0.12\text{m} = 2.87\text{kN}$, they are very close.

Load transfer

When the upper test floor is poured into the concrete, the concrete of the test floor already has a considerable strength (about 90%), so the load transferred from the fresh concrete is "resisted" by the upper floor and the other part is transferred to the test floor, the statistics passed down the load accounts for about 57% ~ 69% of a total load of fresh concrete.

The most unfavourable load

Statistics show that the maximum axial force of each test layer pole appears when the upper floor is poured into the concrete, and the maximum axial force is 1.9 times the axial force generated when the test floor is poured into concrete. Therefore, in the design of multi-layer formwork support systems, the load of single-layer concrete should not only be considered, but a load of concrete poured from the upper floor to the lower floor should be emphasized. If the design ignores the synergetic effect between the multi-layer formwork support system and the building structure, it will only reduce the safety and reliability of the formwork support system if it is considered as a single-layer formwork support.

Unloading speed

After the first and second pouring of concrete, the unloading speed of the pole is also very fast due to the rapid increase of the strength of the concrete in the initial stage of hardening. According to the statistics, the average unloading speed is about 0.10kN / h. However, considering the continuity of construction, the change of unloading speed in the late stage of concrete hardening and the final residual axial force after unloading cannot be continuously monitored.

Pole axial force residual before demolition

The pole still has an axial force of about 1.6-3.5kN before dismantling, indicating that the support frame still provides some protection to the concrete of the roof immediately before demolition. At the same time, the force support frame of a layer on the test layer is in the second peak descent phase, bearing about 4kN axial force. Therefore, before the support frame is dismantled, the upper floor is still subjected to a large load. At this moment, it is particularly important to ensure the strength of the floor concrete during form removal. If the form removal is too early it may cause concrete cracking, deformation, and other issues.

Analysis of the changes in steel bar tension

The measured results show that the tensile strength of steel bars is small, generally not more than 1.5kN, converted to a stress is 29.85N / mm², far less than the yield strength of steel bars. In addition, due to the constraint of the formwork support below the test layer, the variation of the steel tension in the key construction nodes is not as sensitive as the axial force of the pole. Even when the lower formwork support was removed, there was no sudden increase in the tensile strength of the steel bar and the tensile force is remained about 1 kN. After the first pouring of concrete, steel bar has a compressive process, which is mainly caused by the pressure of the concrete shrinking during the initial hardening. In general, the variation of steel tension and pole axial force is consistent.

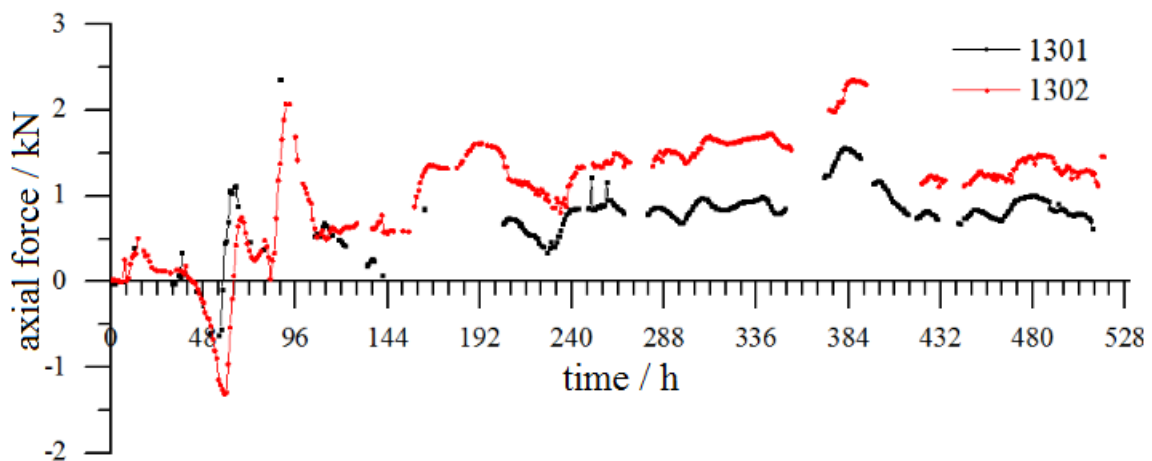


Fig.21 – Change of steel bar

Tab. 4 - Statistics of axial force change of vertical pole

The average value of each measuring point	The increase in axial force when the first pouring of concrete (kN)	Unloading speed (kN/h)	The increase in axial force when the second pouring of concrete (kN)	Unloading speed (kN/h)	The increase in axial force when the third pouring of concrete (kN)	Maximum axial force (kN)	Axial force before formwork removal (kN)
11th floor	2.96	0.16	1.38	0.12	0.55	6.05	1.66
12th floor	2.43	0.10	2.06	0.08	1.68	5.88	3.46
13th floor	3.08	0.06	2.06	0.07	0.53	5.89	2.38
The average	2.80	0.10	1.84	0.09	0.92	5.94	2.50

Tab. 5 - Changes of axial force of each floor after pouring concrete with 14F

	Pole axial force / kN	The increase of axial force / kN	Increase ratio	Age / d	Concrete strength
14th floor	/	3.00	100%	0	0
13th floor	5.89	2.06	69%	7	90%
12th floor	3.96	1.68	56%	14	101%
11th floor	Demolished			21	112%

Tab. 6 - Changes of axial force of each floor after pouring concrete with 13F

	Pole axial force / kN	The increase of axial force / kN	Increase ratio	Age / d	Concrete strength
13th floor	3.58	3.08	100%	0	0
12th floor	5.68	2.06	67%	7	90%
11th floor	3.00	0.55	18%	14	101%
10th floor	Demolished			21	112%

Tab. 7 - Changes of axial force of each floor after pouring concrete with 12F

	Pole axial force / kN	The increase of axial force / kN	Increase ratio	Age / d	Concrete strength
12th floor	2.93	2.43	100%	0	0
11th floor	5.85	1.38	57%	7	90%
10th floor	/	/	/	14	101%
9th floor	Demolished			21	112%

Numerical simulation and analysis

The calculation model is established according to the actual size of the test project. The elastic modulus of concrete for each floor needs to be determined in advance. The elastic modulus of each layer of concrete is closely related to the age. The elastic modulus of concrete can be deduced from the compressive strength of concrete cube according to the formula (1) given in the literature [22], as shown in the Table 8.

$$E_c = \frac{10^5}{2.2 + (33 / f_{cu})} \quad (1)$$

Tab. 8 - Estimated values of elastic modulus at different ages

Age/d	0	3	7	14	21
F_{cu}/MPa	0	21.7	27.0	30.4	33.9
$E_c/10^4 \text{ MPa}$	0.00	2.68	2.92	3.04	3.14

The strength grade of beams and slabs concrete are C30, and that of column concrete is C50. The measured value is input according to the concrete age during modelling. The slabs thickness is 120mm, tubular scaffold spacing is 950 × 1050mm, the diameter of tubular scaffold is 48.3mm and the thickness is 3.6mm, the density of reinforced concrete is 25kN/m³, poisson's ratio is 0.2, and the elastic modulus is input according to Tab. 8. Live loads are not considered in

Tab. 9 - Comparison of measured and simulated values

Items	Pole on the top floor	Pole on the middle floor	Pole on the bottom floor
Simulated Axis Force Mean/ kN	3.41	4.82	2.38
Measured Axis Force Mean/ kN	3.30	5.94	3.50
Deviation range	+3.3%	-19.1%	-32.0%
Simulated Axis Force Mean Considering Stress Redistribution Coefficient of Concrete/ kN	3.41	5.88 (4.82×1.22)	3.54 (2.38×1.22×1.22)
Corrected simulation deviation	+3.3%	-1.0%	+1.14%

It can be found from Table 9 that the accuracy of finite element simulation of newly poured concrete vertical pole on top floor is very high, and the deviation range is only 3.3% compared with the measured data. Similarly, it can be found that after newly poured concrete in the upper layer, part of the load is transferred to the lower layer, and the axial force of the lower column reaches the maximum value of 4.82 kN at this time, which is in accordance with the law obtained from the experimental results.

However, the axial forces of the penultimate and bottom vertical poles of the numerical simulation are quite different from the measured data, with deviations of 19.1% and 32%, respectively. The main reasons for the deviation are that the concrete is still in a fluid-plastic state and there is a redistribution of stress between the support system and the structure. However, when calculating, the vertical and horizontal components are loaded with rigid bodies, and the concrete Flow-Plastic state is not taken into account, resulting in more loads still being borne by the support system. According to the simulation data, it can be seen that the stress redistribution should be taken into account in the shorter age, the stress reduction of concrete members and the increase of the vertical bar axial force. When the axial force of vertical pole increases by about 22%, the deviations between measured and simulated values can be better controlled within 3%.

CONCLUSION

In the multi-layer formwork support system, the support frame and the building structure is an integration. However, construction design for scaffold neglects the interaction between the multi-layer formwork support frame and the main structure. There are obvious deficiencies that make the design for multi-layer formwork support system have a security risk.

The main conclusions are summarized as follows:

- (1) In the multi-layer formwork support system, the load is shared by floor, beams, and support. With the increase of concrete strength and the progress of construction, the proportion of beams and support frame to loads is also constantly changing. Multi-layer formwork support system is a dynamic integration; the law of force is influenced by a variety of factors.
- (2) The stress of the multi-layer formwork support can be simplified as 3 times of peak value, 3 times of decline and 1 time of sudden drop. It is caused by 3 times of concrete pouring, early rapid hardening of concrete and removes the formwork of the lower floor.
- (3) The maximum axial force of each test floor pole appears when the upper floor is poured into the concrete, and the maximum axial force is 1.9 times the axial force generated when the test floor is poured into concrete. Therefore, in the design of multi-layer formwork support systems, the

load of single-layer concrete should not only be considered, but a load of concrete poured from the upper floor to the lower floor should be emphasized.

(4) When the upper test floor is poured into the concrete, the concrete of the test floor already has a considerable strength (about 90%), so the load transferred from the fresh concrete is "resisted" by the upper floor and the other part is transferred to the test floor, the statistics passed down the load accounts for about 57% ~ 69% of a total load of fresh concrete.

(5) After the first and second pouring of concrete, the unloading speed of the pole is also very fast due to the rapid increase in the strength of the concrete in the initial stage of hardening. According to the statistics, the average unloading speed is about 0.10kN/h.

(6) Considering the fluid-plastic state of concrete, a correction factor of 1.22 for vertical pole axial force is proposed, and the deviation between the modified simulated value and the measured value is less than 3%.

REFERENCES

- [1] Chan SL, Zhou ZH, Chen WF, Peng JL, Pan AD. Stability analysis of semi-rigid steel scaffolding. *Eng Struct* 1995;17:568–74.
- [2] Peng JL, Pan AD, Rosowsky DV, Chen WF, Yen T, Chan SL. High clearance scaffold systems during construction–1: structural modeling and modes of failure. *Eng Struct* 1996;18:247–57.
- [3] Peng JL, Pan AD, Rosowsky DV, Chen WF, Yen T, Chan SL. High clearance scaffold systems during construction–2: structural analysis and development of design guidelines. *Eng Struct* 1996;18:258–67.
- [4] Peng JL, Pan AD, Chen WF, Yen T, Chan SL. Structural modeling and analysis of modular falsework systems. *ASCE J Struct Eng* 1997;123:1245–51.
- [5] Peng JL, Pan AD, Chan SL. Simplified models for analysis and design of modular falsework. *J Construct Steel Res* 1998;48:189–209.
- [6] Peng JL, Pan AD, Chen WF. Approximate analysis method for modular tubular falsework. *ASCE J Struct Eng* 2001;127:256–63.
- [7] Yu WK, Chung KF, Chan SL. Structural instability of multi-storey door-type modular steel scaffolds. *Eng Struct* 2004;26:867–81.
- [8] Weesner LB, Jones HL. Experimental and analytical capacity of frame scaffolding. *Eng Struct* 2001;23: 592–9.
- [9] James Reynolds; Hao Zhang; Kim J.R. Rasmussen. Investigation of U-head rotational stiffness in formwork supporting scaffold systems[J].*Engineering Structures*.2017 : 1-11.
- [10] Zhen Xian Yu;Hui Li;Tao Cheng;Li Ping Qin;Zhen Hua Wu;Yue Chen.Analysis for Collapse Accident of Fastener-Style Steel Pipe Formwork Support System[J].*Applied Mechanics and Materials*.2013 : 2917-2920.
- [11] H. Zhang. Probabilistic study of the strength of steel scaffold systems[J].*Structural Safety*.2010, Vol.32 (No.6) : 393-401.
- [12] Liu Hongbo; Jia Li; Wen Suolin; Liu Qun; Wang Gang; Chen Zhihua. Experimental and theoretical studies on the stability of steel tube–coupler scaffolds with different connection joints[J].*Engineering Structures*.2016 : 80-95.
- [13] Timothy P Ambrose;Dryver R Houston;Peter L Fuhr;Elizabeth A Devino;Michael P Werner.Shoring systems for construction load monitoring[J].*Smart Materials and Structures*.1994,Vol.3(No.1) : 26-34..
- [14] Yue-Lin Huang;Wei-Fah Chen;How-Ji Chen;Tsong Yen;Yu-Ghian Koa and Chao-Qin Lina.A monitoring method for scaffold-frame shoring systems for elevated concrete formwork[J].*Computers and Structures*.2000,Vol.78(No.5) : 681-690.
- [15] Saeed Karshenas.Construction live loads on slab formworks before concrete placement[J].*Structural Safety*.1994,Vol.14(No.3) : 155-172.
- [16] D. V. Rosowsky;T. W. Philbrick, Jr.;Dryver R. Huston.Observations from Shore Load Measurements during Concrete Construction[J].*Journal of Performance of Constructed Facilities*.1997,Vol.11(No.1) : 18-23.

- [17] KING ROYER. Construction Loads on Slabs with Shored Formwork in Multistory Buildings[J]. Concrete International. 2004, Vol. 26(NO. 7) : 109-112.
- [18] Buitrago, Manuel; Adam, Jose M.; Calderón, Pedro A.; Moragues, Juan J.; Alvarado, Yezid A. Estimating loads on shores during the construction of RC building structures[J]. Structural Concrete. 2016, Vol. 17(No. 3) : 502-512.
- [19] Mosallam, K; Chen, Wf. Construction Load Distributions For Laterally Braced Formwork[J]. Aci Structural Journal. 1992, Vol. 89(No. 4) : 415-424.
- [20] Qing Rong Tang; Zhi Qiang Fu. Time-Varying Law Experimental Research of the Interaction of Concrete Structure and Formwork Support during the Construction Period[J]. Applied Mechanics and Materials. 2014 : 466-469.
- [21] Guo Zhenhai, Shi Xudong. Principles and analysis of reinforced concrete [M]. Beijing: tsinghua university press, 2003.
- [22] Yang heng. Field measurement analysis and simulation of multi-layer formwork support system [D]. Qingdao university of technology, 2016.

CONSTRUCTION OF NEW MULTI-FUNCTION TYPE ARTIFICIAL BOUNDARY PILLAR FOR TRANSITION FROM OPEN PIT TO UNDERGROUND MINING

Honggang Ren^{1,2}, Zhuoying Tan¹ and Panxue Feng^{1,2}

- 1. University of Science and Technology Beijing, School of Civil and Resource Engineering, Beijing, China: 15120088723@163.com*
- 2. Beijing General Research Institute of Mining & Metallurgy Technology Group, Beijing, China; renhonggang_0123@163.com*

ABSTRACT

In allusion to the defects of large material consumption and high construction cost of conventional artificial boundary pillar for the transition from open pit to underground mining, a new multi-function type of artificial boundary pillar scheme of reinforced concrete is proposed, which creates favourable conditions for underground mining below the pillar and stacking tailings over the pillar. We established the mechanical model of the artificial pillar, and use MIDAS-FLAC3D software to analyse the stability of the artificial pillar. The result shows that the multifunctional artificial pillar has good impervious control and flood control characteristics and bearing capacity, and can effectively separate the influence between the open pit and the underground, which realizes the effective utilization of resources and greatly improve the economic efficiency of mines. At the same time, the tailings in the open pit will support the open slope and enhance the stability of the slope. Moreover, this method effectively reduces the area of tailings reservoir and has good ecological and environmental protection value, which can provide useful reference for related mines.

KEYWORDS

Multi-function; Artificial boundary pillars; Open pit; Underground mining; Tailings

INTRODUCTION

When open pit mining is transited to underground, boundary pillar is the critical safety insurance [1-3]. Boundary pillar could not only avoid mutual impact of the open pit production and underground production, such as blasting vibration, pit water flooding underground, etc., but also benefit the enclosed air ventilation system of underground mining. On the other hand, the boundary pillar could also give supports to side slopes of the open pit. Moreover, in a transition period, if the boundary pillars are too thin, there will be a risk of sudden fall of slope, which might lead to a waste of mineral resources and great economic loss.

Along with the sinking of the exploration, stripping ratio will increase accordingly. When stripping ratio exceeds optimal economic stripping ratio, most of the mines will convert open pit mining to underground, with an intention to cut exploration cost [4-6]. During the transition period, to minimize or isolate the impact of open pit production towards underground mining, 2 alternatives will be taken conventionally: one is that the boundary pillars with a certain thickness are left at the bottom of the pit, which is isolated from underground production; the other is to cave side slope or backfilling waste to form a waste layer to isolate open pit production with underground mining. However, due to the loose structure and uneven particle size of the deposit, the isolation performance is poor, and it usually causes a burden for underground water drainage, flood prevention and ventilation system as well.

Compared with the natural artificial boundary pillar, the artificial boundary pillar structure not only has its function, but also can recover the security pillar resources in advance, and can resolve resources supply during the transition period, and greatly improve backstopping efficiency and reduce grade deterioration of resources. Artificial pillars are reinforced concrete structures with strong integrity and high bearing capacity, and their strength and stability are 2-3 times higher than those of natural boundary columns. It supports side slope better, and anti-seepage and anti-leakage performance enjoy advantages as well. In addition, heap leaching slag and tailings can be installed at the top of the artificial boundary column to save the area occupied by the dump and tailings dam, which has good ecological and economic benefits.

MECHANICAL MODEL

One of the keys to analyse the stability of boundary pillar in the process of transforming the open pit into underground mining is to establish an appropriate mechanical model for mechanical analysis of the structure [7]. According to the stress characteristics of the roof in underground mining, it can be regarded as an elastic foundation beam. As shown in Figure 1, we define as follows: the width of the beam model on the elastic foundation of the local boundary pillar is L , which is a rectangular beam with an equal section length. Under the action of loading $q(x)$, the counterforce between the foundation and the beam is $\sigma(x)$, and the subsidence of the foundation and the beam is $y(x)$. When calculating the internal force of the local boundary pillar model, the subsidence function $y(x)$ is the basic unknown quantity. The calculation model selects the coordinate system XOY , the positive and negative sign of deformation, load and internal force as shown below.

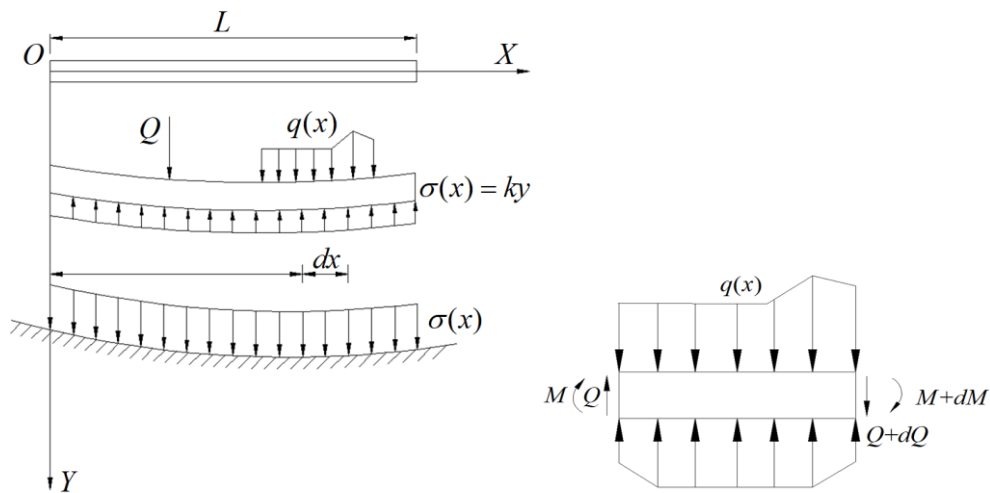


Fig.1- Microelement analysis of the boundary pillar model

It is assumed that a microelement segment dx is intercepted in the beam, the following formula is obtained according to the vertical equilibrium condition:

$$\sum Y = Q - (Q + dQ) + kydx - q(x)dx = 0 \tag{1}$$

After simplifying the calculation, the following formula can be obtained:

$$\frac{dQ}{dx} = ky - q(x) \tag{2}$$

According to the moment equilibrium condition, the following result is obtained:

$$\sum M = M - (M + dM) + (Q + dQ)dx + q(x)\frac{(dx)^2}{2} = 0 \tag{3}$$

After omitting the second order derivative, the following formula is obtained as:

$$Q = \frac{dM}{dx} \tag{4}$$

After solving the derivative of the above equation, and substitute the result into the Equation (2), the result is obtained as below:

$$\frac{dQ}{dx} = \frac{d^2M}{dx^2} = ky - q(x) \tag{5}$$

If the deflection y of the beam and the angle θ of any section of the beam are known, then the bending moment and shear force can be calculated according to the formula in mechanics of materials, that is:

$$\left\{ \begin{array}{l} \theta = \frac{dy}{dx} \\ M = -EI \frac{d\theta}{dx} = EI \frac{d^2 y}{dx^2} \\ Q = \frac{dM}{dx} = -EI \frac{d^3 y}{dx^3} \end{array} \right. \quad (6)$$

When the artificial boundary pillar is regarded as a beam on the elastic foundation, the internal force of the beam is calculated by the theory of elastic foundation beam, and the equation of internal stress is:

$$\left\{ \begin{array}{l} \sigma_x = \frac{6(q + \rho gh)}{h^3} (l^2 - x^2)y + \frac{(q + \rho gh)y}{h} \left(\frac{4y^2}{h^2} - \frac{3}{5} \right) \\ \sigma_y = \frac{\rho gh}{2} \left(1 - \frac{4y^2}{h^2} \right) - \frac{q}{2} \left(1 + \frac{y}{h} \right) \left(1 - \frac{2y}{h} \right)^2 \\ \tau_{xy} = -\frac{6(q + \rho gh)}{h^3} \left(\frac{h^2}{4} - y^2 \right) x \end{array} \right. \quad (7)$$

According to the beam theory of elastic foundation, the shear and bending moment of the beam section can be calculated, then the stress distribution on any cross section of the beam can be obtained from the above formula, and the stability of the beam can be evaluated and analysed according to the strength criterion.

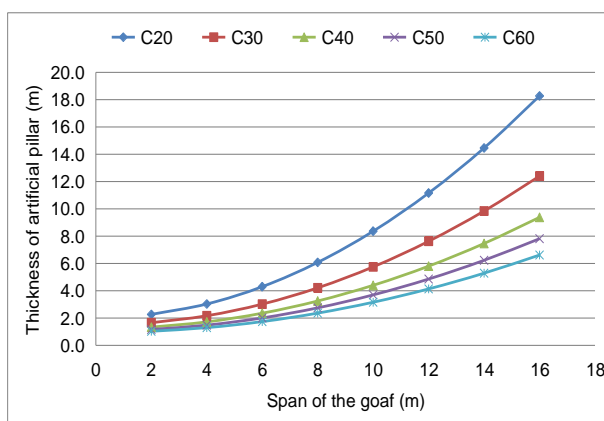
THEORETICAL CALCULATION OF THE THICKNESS OF THE ARTIFICIAL PILLAR

There are many theoretical calculation methods for calculating the safe thickness of boundary pillar, several of the commonly used methods are as follows [8]-[9]: (1) K.B.'s formula. (2) B.I.'s formula. (3) Plate beam theory. (4) Protodyakonov ground pressure theory. (5) Engineering calculation method. (6) Material mechanics method. This paper summarizes the principles and applicable conditions of various theoretical methods for calculating artificial pillars, and its engineering analytical method is shown in Table 1.

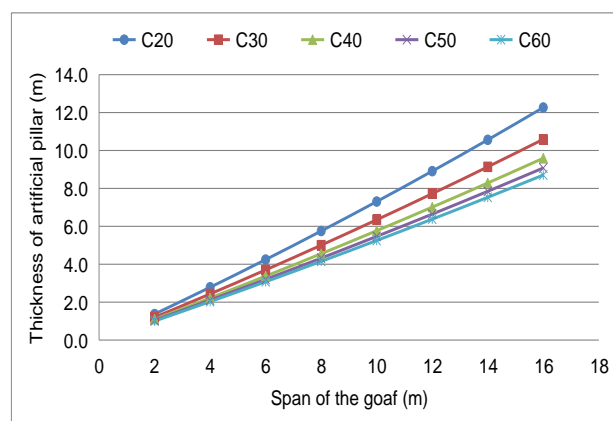
Tab.1 - Summary of engineering method for calculating safety thickness of artificial pillars

Method type	Calculation principle and consideration factor	
K.B.'s formula	The effects of goaf span and rock properties (strength and structural failure characteristics) on boundary pillar is considered, and the influence of working equipment on the bench is also considered.	
В.И.'s formula	The effects of goaf span, boundary rock mass characteristics (tensile characteristics) and dynamic load of bench blasting are considered.	
Plate beam theory	Assuming that the boundary pillar is a slab beam fixed at both ends, according to the theory of material mechanics, the formula for calculating the thickness of the safety boundary pillar is derived.	
Engineering method	calculation	The basic principle is to simplify the calculation of complex three-dimensional thick plates as the plane problem of idealized elasticity theory.
Material method	mechanics	The boundary pillar is regarded as a simply supported beam, and the thickness of the beam under ultimate load is calculated.

The above methods are used to calculate the thickness of artificial boundary pillar according to different strength concrete (C20, C30, C40, C50, C60, they mean that the compressive strength of concrete is 20MPa, 30MPa, 40MPa, 50MPa, 60MPa, respectively.), and the calculated results are shown in the following figures.

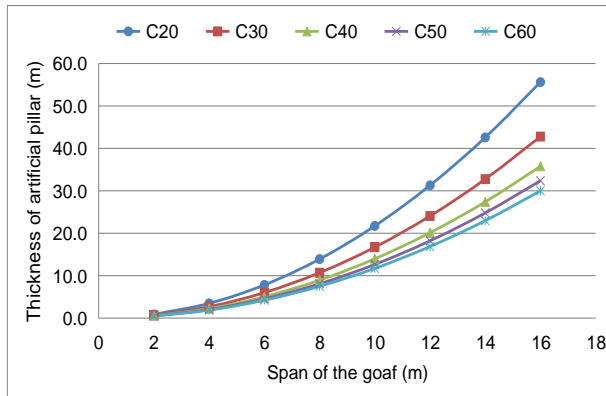


(a) K.B.'s formula

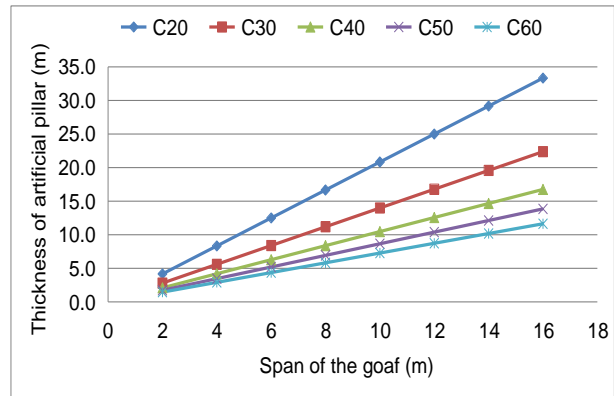


(b) Plate beam theory

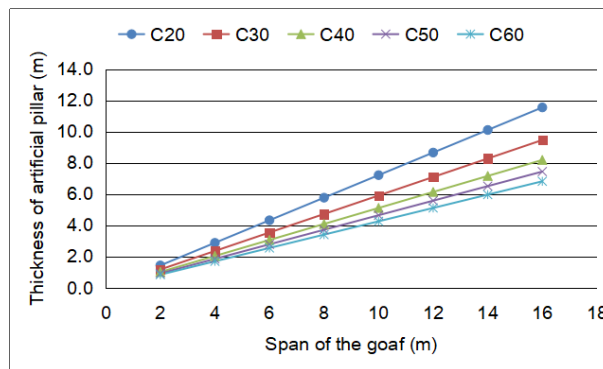
Fig.2 - Artificial pillar thickness calculated by different theories and methods



(c) Engineering calculation method



(d) Protodyakonov ground pressure theory



(e) Material mechanics method

Fig.2 - Artificial pillar thickness calculated by different theories and methods

It can be seen from Figure 2 that the thickness of the artificial pillar decreases with the increase of the concrete strength, and increases with the increase of the goaf span. Through the technical and economic analysis, it is considered that C40 strength concrete is better. For the C40 strength concrete artificial pillar, we calculated the required thicknesses under different spans by different theories and methods. See Table 2 and Figure 3.

Tab.2 - Artificial pillar thickness calculated by different methods under different span of goaf

Calculation method and theory	Span of the goaf /m							
	2	4	6	8	10	12	14	16
K.B. formula	1.3	1.7	2.4	3.3	4.4	5.8	7.5	9.4
Plate beam theory	1.1	2.2	3.4	4.6	5.8	7.0	8.3	9.6
Engineering method	0.6	2.2	5.0	8.9	14.0	20.1	27.4	35.8
Protodyakonov ground pressure theory	2.1	4.2	6.3	8.4	10.5	12.6	14.7	16.8
Material mechanics method	1.0	2.0	3.1	4.1	5.1	6.1	7.2	8.2

As can be seen from Figure 3, the calculation of the numerical values by K.B., Plate beam theory and Material mechanics method are very close, and the theoretical analysis accords with the engineering practice. However, because the Loose coefficient theory and the Protodyakonov ground pressure theory do not take into account the stress conditions of artificial pillars, the accuracy of the calculation is not high. Also, the engineering calculation method is a simplified calculation method, which ignores the external influence factors, and calculates accurately and is not worth trusting. In this paper, the calculation results of K.B. formula., Plate beam theory and Material mechanics method are used as reference and comparison. In order to ensure the reliability and accuracy of the calculation, numerical simulation and elastic foundation beam theory are used for further calculation and verification.

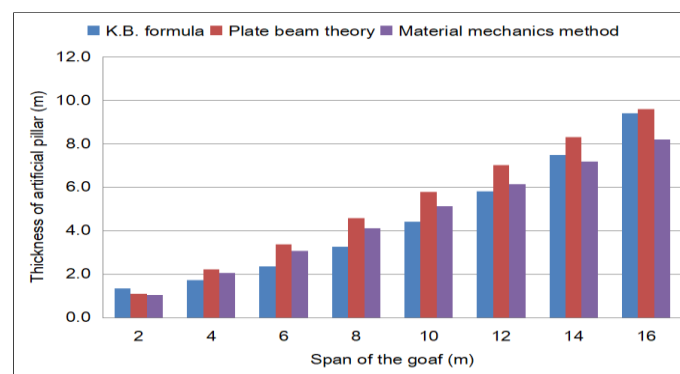


Fig.3 - Similar calculation results of artificial pillar thickness

DESIGN OF ARTIFICIAL PILLAR

Engineering background

The upper ore body of a gold mine is taken by open-pit mining. The maximum size of open stope is 881m×168m, and the maximum vertical depth of open stope is 57 m. Underground mining and main ramp exploitation system are adopted in the underground mine, and the mining method is sublevel open stopping and subsequent filling with the mining in order from the bottom to the top, see Figure 4. In order to ensure the independence of underground mining and tailings stacking in open pit and ensure the safety of underground mining and tailings rejection, it is necessary to set up artificial boundary pillar.

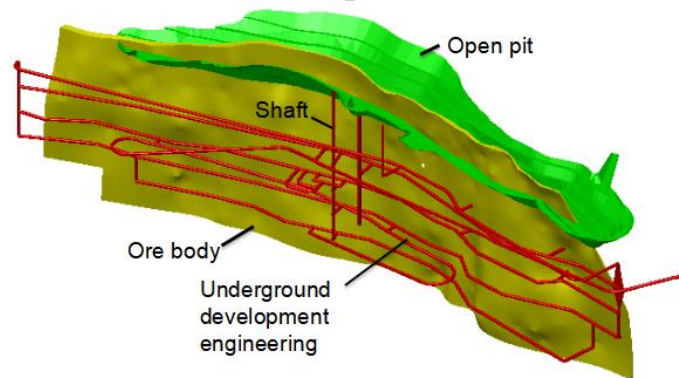


Fig.4 - 3D design model of transition from open pit to underground mining

Design range of artificial pillar

According to the mining technical conditions, artificial bottom width, stability state of the open pit slope, mine hydrogeology and other factors, the design of the artificial pillar is divided into five areas: A, B, C, D and E. The distribution characteristics of artificial pillars in various regions are shown in Table 3 and Figure 5.

Tab.3 - Subarea characteristics of the artificial pillar in a gold mine

Subarea name	Location	Width (m)	Length (m)
A	9S~19	6	213
B	0~9S,32~42,18~20	10	300
C	0~10S	8	163
D	12~18	22	80
E	28~32	12	61

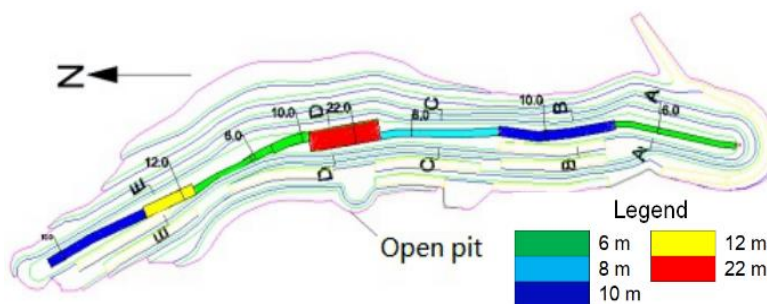


Fig.5 - Layout plan of artificial pillar

Structure of an artificial pillar

After completion of open pit mining, short hole and minor delay blasting will be adopted at bottom of the open pit to provide an even slope for artificial pillar construction. The artificial pillar uses reinforced concrete structure, to connect with reinforced concrete artificial pillar with anchor bolt and integrate with wall rock. Due to long distance of the open pit bottom, the artificial pillar will be constructed in steps and layers to form an integrated structure at the end. It cannot only improve stability of the boundary pillar, but also get portion of the ores to ensure stable transition from open pit production to underground mining. The schematic diagrams of artificial pillar structure are shown in Figure 6. and Figure 7.

After completion of open pit mining, short hole and minor delay blasting will be adopted at the bottom of the open pit to provide an even slope for artificial pillar construction. The artificial pillar uses reinforced concrete structure to connect reinforced concrete artificial pillar with anchor bolt and integrate with wall rock. Due to the long distance of the open pit bottom, the artificial pillar will be constructed in steps and layers to form an integrated structure at the end. It cannot only improve the stability of the boundary pillar, but also get a portion of the ores to ensure the stable transition from open pit production to underground mining. The schematic diagram of the artificial pillar structure is shown in Figure 6. and Figure 7.

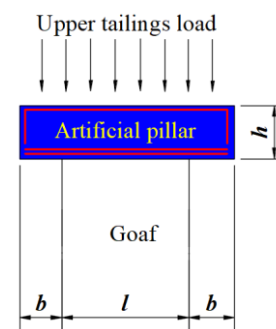
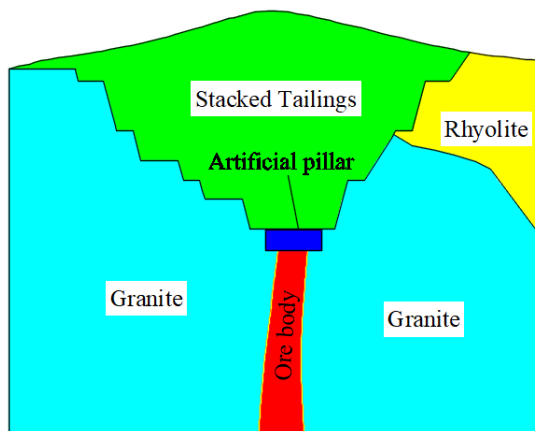


Fig.6 - Structure arrangement of artificial pillar Fig.7 - Magnifying structure of artificial pillar

Isolation and cushion layer of artificial pillar

In order to avoid possible cracks in the pillars of artificial boundary and prevent surface water from penetrating into the underground, the upper layer is provided with an isolation layer. The structure of the isolation layer is 100 mm thick powdery rock and 0.5mm thick geomembrane above it. It can also lay 0.5mm thick geotextiles, plus a layer of agricultural film. In order to prevent the blasting damage to the artificial pillar structure when the underground ore body is being mined, the blasting cushion is left at its bottom. The cushion is made up of gravel, which is placed above the ore body before the construction of artificial pillars. See Figure 8.

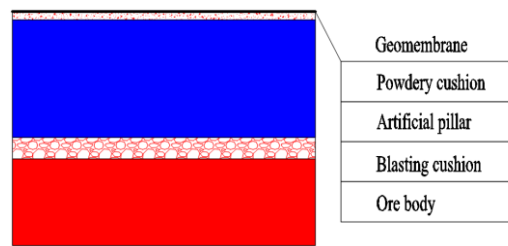


Fig.8 - The upper isolation layer and the lower cushion structure of artificial pillars

STABILITY ANALYSIS OF ARTIFICIAL PILLAR

In practical application, the factors affecting the thickness of the artificial boundary pillar mainly include the span of the goaf, the physical and mechanical parameters of the ore and rock, the mining order, the engineering geology and hydrogeology of the rock mass, and the condition of the original rock stress and so on. However, some factors can only be considered in theoretical calculation, which often leads to a certain gap between the calculation results and the actual situation [10]-[11]. In order to make the calculation result closer to reality, comprehensively considering the factors affecting the stability of artificial pillars, the FLAC3D software is used to simulate the artificial pillar under different spans to ensure that the parameters of the boundary structure are more reasonable.

Mechanical parameters of rock mass

Physical and mechanical parameters of the ore rock are the basic parameters of numerical simulation. The accuracy of numerical simulation results depends on whether the parameters values are correct or not. Generally, the mechanical parameters of rock are obtained by the rock mechanics test under ideal conditions, and then it can be used for numerical simulation after the test data are reduced by the Hoek-Brown criterion, The rock mass parameters after deducted in this paper are shown in Table 4.

Tab.4 - Rock mass parameters after being deducted

Lithology	Bulk modulus(GPa)	Poisson ratio	Tensile strength (MPa)	Cohesion (MPa)	Friction Angle (°)
Granite	4.16	0.19	3.71	4.93	32.40
Ore body	4.16	0.19	3.71	4.93	32.40
Rhyolite	1.28	0.30	0.96	3.70	39.93
Tailings	0.05	0.10	0.10	0.07	18.50

Numerical simulation calculation

The 3D numerical calculation model and typical section model of the mining area are established by using MIDAS software. See Figure 9.

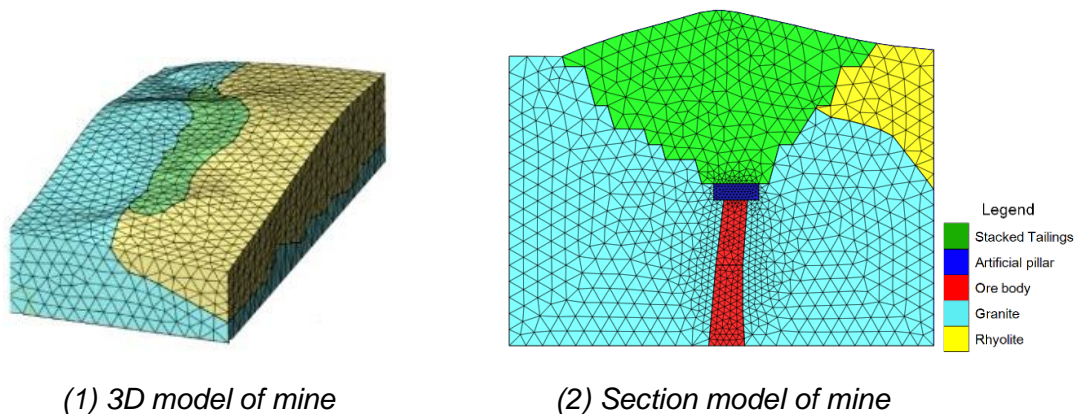


Fig.9 - The numerical simulation model based on MIDAS software

In order to comprehensively study the safety thickness of artificial pillars under different spans, the numerical simulation of the artificial pillars stability under different spans (6~22 m) was carried out by FLAC3D. Taking the goaf with a span of 7 m and a height of 20 m as an example, the models of artificial pillar thickness of 3m, 4m, 5m, 6m and 7 m are constructed respectively. Moreover, the stress state and artificial pillar safety state of 5 goaf models are studied and analysed. Figure 10 shows the displacement and stress cloud map of the mine section.

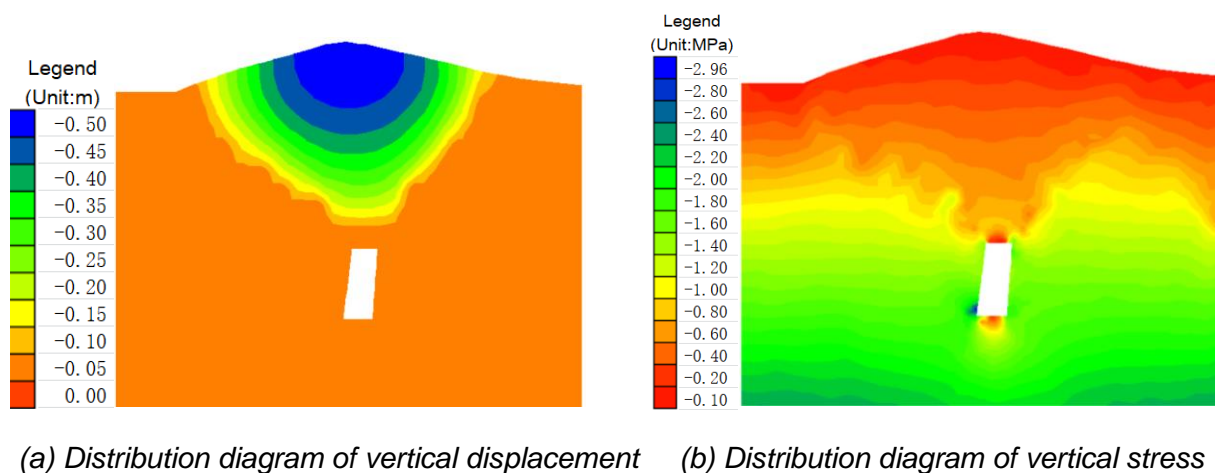


Fig.10 - The results of calculation by using FLAC3D software

When the span of the goaf is 7 m, the maximum displacement of artificial pillars at different thicknesses is shown in the Figure 3. It is shown that the displacement of the artificial pillar is inversely proportional to its thickness.

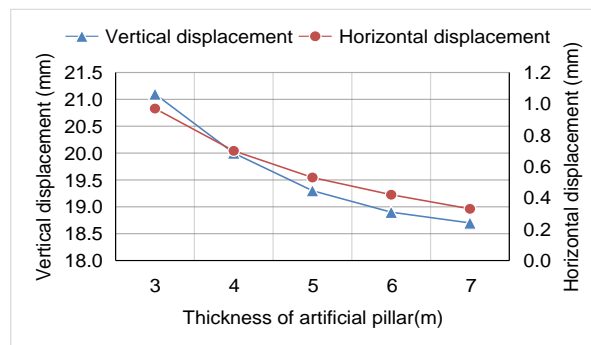


Fig.11 - The maximum displacement of artificial pillars at different thicknesses

The principle of Griffith criterion is that the failure of rock is caused by tensile stress [12]-[15]. Since the tensile stress is the most important factor determining the stability of the mined out area, this paper mainly analyses the influence of tensile stress on artificial pillars. It can be seen from Figure 1 that the maximum tensile stress of the artificial pillar appears in the middle area, and the tensile stress zone becomes smaller with the increase of the thickness of the top pillar. Table 3 shows the maximum tensile stress and safety factor under different boundary pillar thickness, it can be found that with the increase of the thickness of the top pillar, the maximum tensile stress of the boundary column becomes smaller and the safety factor increases.

Tab.5 - The maximum stress of different boundary pillar thickness when the span is 7 m

Thickness of boundary pillar / m	Maximum tensile stress / Mpa	Safety factor
3	1.36	1.19
4	1.04	1.56
5	0.98	1.66
6	0.94	1.73
7	0.91	1.79

Based on the principle that the safety factor of tensile stress in artificial pillar is not less than 1.2, the minimum boundary pillar thickness is recommended as shown in Table 6.

Tab. 6 - The recommended values of different boundary pillar thickness from numerical simulation

The span of the goaf / m	6	8	10	12	22
Thickness of artificial pillar / m	2.2	3.2	4.2	5.2	11.2

Comparison between theoretical calculation and numerical simulation results

Figure 12 shows the comparison between theoretical calculation and numerical simulation of artificial pillars with different widths. The research shows that when the width of the artificial pillar is less than 5m, the numerical simulation value of tensile stress is larger than that of the elastic foundation theory. When the width of the artificial pillar is greater than 5m, the result is opposite. The shear stress value calculated by elastic foundation is higher than that of the numerical simulation. This is because the elastic foundation beam theory does not consider the lateral pressure affected by the horizontal sides of the beam, and in the actual project, the slope of the open pit has lateral pressure on the artificial pillar, which will reduce the shear stress.

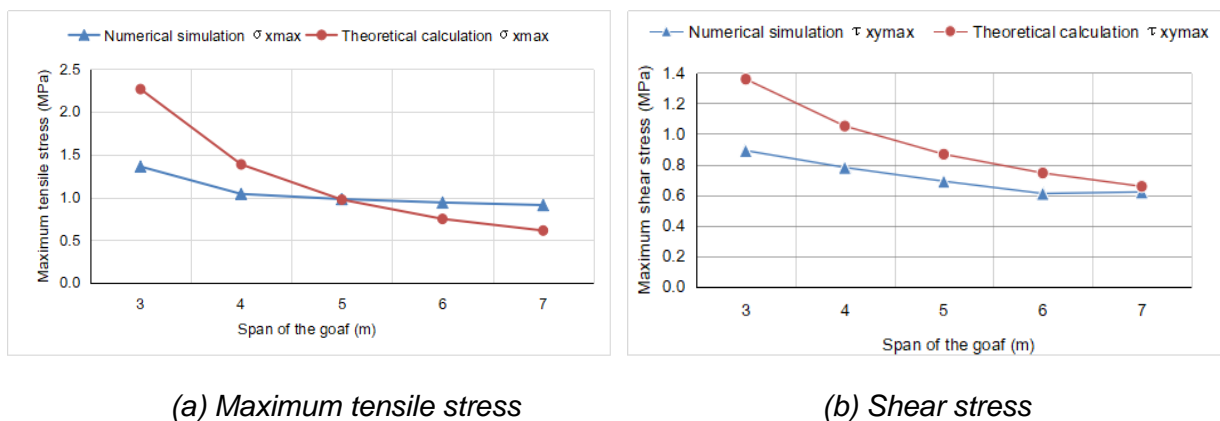


Fig.12 - Comparison between theoretical calculation and numerical simulation results

CONCLUSION

A new multi-function type of artificial boundary pillar scheme of reinforced concrete is proposed in this paper, which creates favourable conditions for underground mining below the pillar and stacking tailings over the pillar. Based on a variety of theoretical methods and numerical simulation techniques, the stability of artificial pillars with different structure sizes is analysed, which provides a reference for mine safety mining and actual production.

In this paper, the mechanical model of the artificial pillar is established, and the numerical simulation of MIDAS-FLAC3D software is used to verify and compare the results. The simulation results show that the thickness of the artificial pillar and the span of the goaf have an important influence on its stability. The maximum tensile stress of the artificial pillar is inversely proportional to its thickness, and it is directly proportional to the width of the goaf.

The multi-functional artificial pillars have good impervious and flood control characteristics and pressure bearing capacity, and can effectively separate the influence of the open pit and the underground that realizes the effective utilization of resources and greatly improve the economic efficiency of mines. At the same time, it enhances the stability of the slope for the piled tailings in the open pit the slope play a supporting role. And it effectively reduces the tailings reservoir area,

and has good ecological and environmental value, which can provide an demonstration role for the relevant mines.

ACKNOWLEDGMENTS

The financial support from the fund of the National Natural Science Foundation of China (No. 51574015) is greatly appreciated.

REFERENCES

- [1] E. Bakhtavar, K. Shahriar, K. Oraee. Transition from open-pit to underground as a new optimization challenge in mining engineering[J]. *Journal of Mining Science*, 2009, 45(5):485-494.
- [2] E. Bakhtavar. Transition from open-pit to underground in the case of Chah-Gaz iron ore combined mining[J]. *Journal of Mining Science*, 2013, 49(6):955-966.
- [3] E.A Cordova, M.G Nelson. Open pit and underground mine interaction with phase 2[C]. 44th U.S. Rock Mechanics Symposium and 5th U.S.-Canada Rock Mechanics Symposium, 2010, Salt Lake City, Utah.
- [4] Bakhtavar Ezzeddin, Shahriar Kourosh, Oraee Kazem. Mining method selection and optimization of transition from open pit to underground in combined mining[J]. *Archives of Mining Sciences*, 2009, 54(3):481-493.
- [5] Lu Guang-luo, Zhou Quan, Liu Xiao-ming. Safety analysis of interlayer thickness from open pit to underground mining[J]. *Journal of Mining and Safety Engineering*, 2011, 28(1):132-137.
- [6] Zhao Xing-dong, Li Lian-chong, Tang Chun-an. Stability of boundary pillars in transition from open pit to underground mining[J]. *Journal of Central South University*, 2012, 19(11): 3256-3265.
- [7] I.V. Sokolov, A.A. Smimov, Yu. G Antipin. Rational design of ore discharge bosom in transition from open pit to underground mining in udachny mine[J]. *Journal of Mining Science* January, 2013, 49(1): 90-98.
- [8] C. Gonzalez-Nicieza, M.I. Alvarez-Fernandez, A. Menendez-Diaz. A comparative analysis of pillar design methods and its application to marble mines[J]. *Rock Mechanics and Rock Engineering*, 2006, 39(5): 421-444.
- [9] Liu Hong, Hu Qian-ring, Wang Jin-an. Analysis on stability of pillar and stiff roof system in the gob area[J]. *Journal of Coal Science&Engineering*, 2009, 15(2): 206-209.
- [10] Bi Jinzhong, Wang Ping, Chen Cong. Study on safety thickness of top-pillar in transferring from open pit to underground mining[J]. *Nonferrous Metals: Mine Section*, 2013, 65(4):8-11. (in Chinese)
- [11] Shi Jianjun, Meng Haili, Gao Kelin. Numerical simulation of the stability of boundary pillar[J]. *Mining and Metallurgical Engineering*, 2004, 24(6):7-10. (in Chinese)
- [12] Liu Ting-ting, Lu Guo-bin, Tong Li-ming. Numerical simulation study of the influence on stability of slope by underground mining under opencast coal mine slope[J]. *Journal of Coal Science&Engineering*, 2011, 17(4): 397-400.
- [13] Alexander Vyazmensky, D.Stead, D. Elmo. Numerical analysis of block caving-induced instability in large open pit slopes:A finite element / discrete element approach[J]. *Rock Mechanics and Rock Engineering*, 2010, 43(1): 21-39.
- [14] A.Mortazavi, EP. Hassani, M. Shabani. A numerical investigation of rock pillar failure mechanism in underground openings[J]. *Computers and Geotechnics*, 2009, 36: 691-697.
- [15] A. Jaiswal, B.K. Shrivastva. Numerical simulation of coal pillar strength[J]. *International Journal of Rock Mechanics & Mining Sciences*, 2009, 46: 779-788.

EXPERIMENTAL STUDY OF BITUMINOUS MIXES, FATIGUE PHENOMENON UNDER TANDEM SOLICITATION AT LARGE STRAIN

M'hammed Merbouh

FIMAS Laboratory, Department of Civil Engineering and Hydraulic, University Tahri Mohamed of Bechar, BP 417 Bechar, 08000, Algeria; mmerbm@yahoo.fr

ABSTRACT

Asphalt mixture in pavement is exposed to a fatigue phenomenon which often causes its failure after a certain period of operation. Conventionally this is simulated in the laboratory by a mechanical stress in the form of continuous sine under the effect of a single axle. In recent years the designs of aircraft and large vehicles have changed a lot, given the needs in volume and transport capacity requested. We often see the tandem axles, tridem axel etc. Damage of asphalt mixture is related to vehicle characteristics (number and loads per axle, suspension type, speed, tyre type and configuration...); rest period, temperature and pavement material properties. Modern conceptions of jumbo aircraft type (e.g. Airbus A380, B777 etc...) and new designs of heavy trucks have imposed other forms of solicitation. This type of loading is dual axles with higher strain amplitude. Currently the road pavement and airport asphalt are subject to high levels of strain (or stress) of short duration at each passage of axles. The choice of the structure and the sizing of a roadway require consideration of several technical criteria, economic and geographic, such as heavy traffic and its developments. In this context, fatigue tests were carried out under load at large deformation (high strain amplitude) and can have multipeak shapes (tandem low valleys between two successive peaks). These tests were used to assess and compare the effect and aggressivity of large amplitudes of strain in terms of life, according to two types of signals (single axle and tandem).

KEYWORDS

Asphalt mixture; Pavement; Fatigue; Large strain; Sine; Single axle; Tandem

INTRODUCTION

Pavement layers are subjected to bending forces that do not cause immediate failure, but the repetition of which can eventually lead to a fatigue crack. The effects of multi-axle loads are taken into account in the form of coefficients of aggressivity, dependent on the geometry of the axles and the type of structure, often roughly, resulting from simplified assumptions of superposition of elastic fields [1], [2], [3]. The classical fatigue model, calculated from the fatigue of the laboratory tests with a sinusoidal signal applied at various levels of deformation, is only a function of the level of longitudinal deformation [4]. Future development of pavement operating conditions, appearance of trucks or heavy traffic loadings and jumbo aircraft like Airbus A380 and B777 in real-life conditions, requires a more detailed analysis of the behaviour of materials under this type of stress [5]. The specificity of the load with high level of deformation and the particular shape of the signal-time deformation of tandem axles must be at the heart of such an analysis. On pavements, the aggressiveness of these loads is even more dangerous in intersections [6].

Changes in traffic and recent architecture have imposed new conditions of stress, such as multipeak loading and large strain. Thus, the standard fatigue test is questionable. One of the main criticisms related to these conditions is that the test is not representative with the signal shape nor the magnitude of stresses applied during the successive passage of axles "heavy weights" on a pavement structure. Thermo-viscoelastic behaviour of the asphalt pavement materials induces a dependency on the pavement's response, in terms of strain, on several factors such as the speed of vehicle and the temperature of asphalt layers [7], [8], strain level, binder composition, healing and rest periods, frequencies, strain level [9], loading form [10], air voids content and compaction, aggregate characteristics [11], and even the configuration of the tire [12]. The natural frequency of an HMA layer depends on the delayed response associated with the viscous properties of the material, during the unloading phase [13]. There is a strong need to improve the design criteria, so that they integrate the different configurations of charges corresponding to the different vehicle types, with specific signals simulating complex loadings. On the floor, the frequency and temperature are not constant, and the solicitation is not continuous. In practice, signals are intermittent and there are often multipeak forms in tandem or tridem at high amplitudes. Aggression increases with increasing number of axis [14]. The objective in this work is to adapt the classic test of fatigue on trapezoidal specimen, to make a comparison and to analyze the differences between the sine and tandem signals, thus to quantify their aggressiveness and to take into account the particular context and improve knowledge of mix asphalt and design rules.

EFFECT OF TEST CONDITIONS ON ASPHALT MIXTURE FATIGUE – A REVIEW

Fatigue of asphalt pavement depends mainly on load conditions; different variables interact differently. Generally, the controlled strain mode of testing displays better fatigue life than the controlled stress mode of loading [16], but at higher levels of strain the difference with the imposed stress mode is reduced [17]. Application of very high deformation (600-1000 μ strain) under sinusoidal loading at 20°C, the lifetimes obtained are in the order of 10^4 - 10^5 cycles, with flexural stiffness in order of 1400 - 1600 MPa [18]. Fatigue life of asphalt mixtures and binders decrease with increase in frequency, the fatigue life of the blends and binders decrease with increasing stress level. The correlation is good between the durations of the mixture and the binder [19]. By increasing temperature, fatigue life of HMA decreases. By Indirect Tensile Fatigue (ITF) test when the temperature changes from 5; 25 to 40 ° C, the life of HMA falls in the order of 2100; 1800 to 1700 cycles at a stress level of 250 kPa. At a stress level of 400 kPa, it drops by (1300; 1150; 1000 cycles) for the same temperatures [20]. The "3D-MOVE" model treats the tire-pavement interaction as a moving loaded area. The model incorporates pavement response parameters such as the dynamic tire-pavement load variations and corresponding complex contact stress distributions (normal and shear), vehicle speed, and viscoelastic material characterization. The response from a conventional tandem axle, contact shear stresses did not significantly influence the tensile strain at the bottom of the asphalt concrete layer [21]. An example with VISCOROUTE, the response curves obtained, for a twin-wheel single axle, give very similar results to a sine signal in the longitudinal direction (for ϵ_{xx}) and to a tandem signal in the transverse direction (for ϵ_{yy}). The amplitude of these responses is relative to the solicitation rates [22]. HMA resistance is governed by two fundamental mechanisms: the number of repetitive load cycles for microcracks to coalesce into macrocracks in a crack initiation process (N_i) and the number of repetitive load cycles for macrocrack propagation through the HMA layer thickness in a crack propagation process (N_p), based on continuum fracture-mechanics and work theory to exhibit discriminate and rank HMA mixes [23]. When vehicle speed increases, the dynamic deflection of pavement surface is higher than the situation in static, due to the overlapping effect. A discontinuous zone of shear stress was observed on the base surface between the location under moving load and the location moving load just passed [24]. For HMA, fatigue test was conducted at

10 and 20 °C, and at loading frequency of 10 Hz, using the energy approach, either in the stress controlled mode or in controlled displacement mode. The rate of change of the dissipated energy indicates a value of the plateau which is dependent on the loading mode. And, the cumulative energy is independent on the loading mode; there is a relation between the two modes of loading. Stress controlled mode tests are more practical in the laboratory, but their lifetimes are shorter [25]. The increase in fatigue life with frequencies gives an exponential relation at 20 and 30 °C; and it is higher when the stress levels are lower. At higher load frequencies, the difference in fatigue time between the different levels of stress was much higher [26].

EXPERIMENTAL APPROACH

Material

The material used for this campaign has been widely studied for fatigue behaviour in the past IFSTTAR (LCPC) and international RILEM research committee projects [15]. This is an asphalt mixture (0-6mm). It is a 0/6 mm continuously graded dense asphalt concrete normally used for surface layers. The binder is a pure 50/70 and the binder content is 6.85%. The theoretical compaction ratio of the mix is 95%. The specimens were cut from slabs (400x600x120 mm) manufactured with a rolling compactor according the standard (EN 12697-33). Trapezoidal specimens were cut to perform mechanical tests as complex modulus (EN 12697-26) and fatigue. The complex modulus of the mix is around 8000 MPa at (20°C and 25Hz) and 14000 MPa at (10°C and 10 Hz).

Tab.1 – Composition and grading curve of considered material

Granulometry [% passing]							
Sieve [mm]	0,08	0,31	1,0	2,0	4,0	6,3	8,0
Mix Asphalt	11,8	22,6	39,0	59,5	70,2	97,0	100

Test Conditions and Applications

Load Signal and Forms

Fatigue tests of the following campaign are performed at 20 °C, and at different strain levels. Their range has been fixed to reach fatigue life between 10^4 and 10^5 loading cycles. This range of fatigue life is more representative for airfield pavements. They are higher than classical ones compared to levels to reach one million of cycles usually aimed to define the ϵ_6 value leading to a fatigue life of 10^6 cycles (EN 12697-24). Multi peak signal is compared to classical sinusoidal approaches. The experimental investigations are focused on the influence of the decrease between the two peaks. This is numerically controlled by the λ parameter. We take both cases: $\lambda = 0.25$ and 1 , $\lambda = (\epsilon_{\max} - \epsilon_{\min})/2\epsilon_{\max}$, where ϵ_{\min} is the minimum strain level between the two peaks and ϵ_{\max} is the maximum strain level. We define the signals applied based on a single parameter λ , which sets the shape of the signal. Figure 1 shows the shape of the sine and obtained tandem. The factor λ may vary from: 0.0 to 1.0. From the tandem signal at 25/3 Hz, we find the sine signal for the maximum value of $\lambda = 1.0$, but at 25 Hz. Given the capabilities of the machine fatigue of LRPC-Bordeaux ($F_{\max} = 12\text{daN}$), these bending tests at high amplitudes must be made on standard trapezoidal specimens, attached to the base and free at the top, at a temperature of 20 °C and frequency of 25Hz (sine) and $25/3 = 8.33$ Hz (tandem). Representing vehicle speeds about 100 and 35 km/h. Four pieces can move independently of each other. During the test, the system regulates on the corresponding channel and the vibratory pot for each specimen. The origin of the fatigue

test is in the comparison of tensile deformation by bending, calculated at the base layers of asphalt pavement, with the values of maximum strain supported by a coated specimen in the laboratory [27].

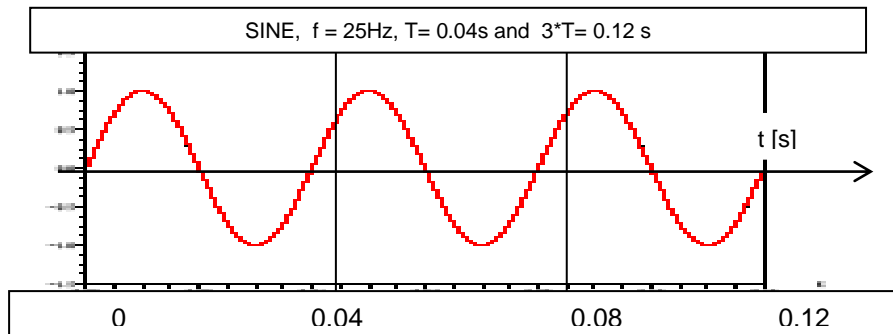


Fig. 1a - Illustration of Sine (Tandem_1,0) signal

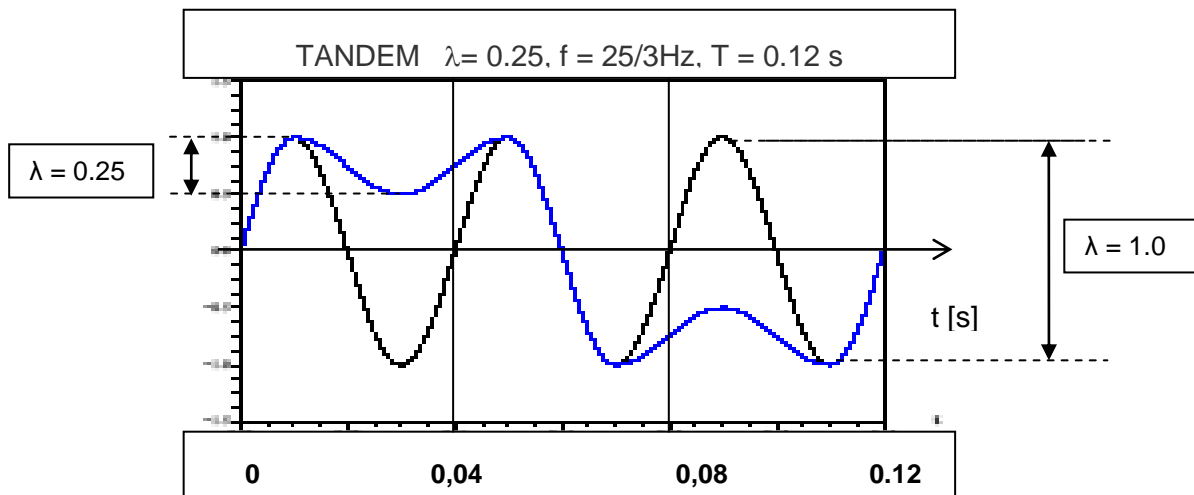


Fig. 1b - Illustration of Tandem_0,25 signal

Fatigue testing at high strain

Machine Test has four vibratory pots (Figure 2) to test four specimens simultaneously under the same test conditions. The four specimens can evolve independently of each other. During the test, the system regulates, on the corresponding channel, the vibratory pot for each specimen. Fatigue tests are performed in imposed constraint mode. We tried to reproduce in the laboratory the real conditions of large strain, using the protocol loading "software DataPhysique." The test program is to scan the spectrum amplitudes solicitations on pavement. If we translate the magnitude of stress in terms of life, we tried to reproduce life spans ranging from 10^4 to 10^5 cycles. The strain ϵ_f (ϵ_{moy}) and the temperature ($20\text{ }^\circ\text{C}$) are constant for the entire program. We must quantify the tandem_0.5 effect to equivalent number of peaks, with respect to the sinusoidal loading reference: for the same period the sinusoidal signal has three peaks (positives), while the signal tandem has two peaks Figure 4.

Tests are performed continuously with alternating sequences of fatigue with a duration T_f ($T_f = 11s$) and sequences of rest period T_r ($T_r = 1.5s$), to facilitate storage of measurements [15].



Fig. 2a - Machine test of fatigue

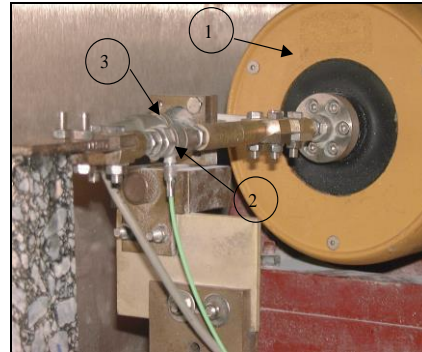


Fig. 2a - Specimen biasing device
 (1) Vibrator, (2) Force sensor
 (3) Displacement sensor

The maximum values of stress and strain were measured at regular intervals. The magnitude of ϵ_f corresponding to the third level of strain is the maximum allowed by the system. The three levels are well above ϵ_6 applied to conventional fatigue testing of this material and do not exceed about $200\mu\text{strain}$, but correspond to compare strains to those that can be measured in pavement.

The experimental simulation takes into account the phenomenon of viscoelasticity, which leads to more realistic stress field; it explains the presence of a higher strain in the second axle [28], especially in the passage of a rolling load. It allows rigorously take into account the speed of vehicles. It also helps to highlight phenomena that traditional elastic numerical modelling does not allow it, as the strain rate.



Fig. 3a - Tandem (Truck)



Fig. 3b - Tandem (A380)
 (Long. and Transv)

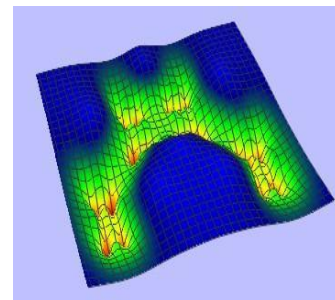


Fig. 3c - 3D graphical Visualization of deformations generated by a B747 aircraft (CESAR-LCPC) [29]

We define the parameter λ establishing the position of the descent (trough) between two successive peaks of a tandem. In this context it is proposed fatigue tests at high strain amplitudes, as both types of signals, sine or tandem_ $\lambda = 1.0$ (where the hollow between two successive peaks of the tandem is maximum) and tandem_ $\lambda = 0.25$ (where descent between two peaks is 1/4 of its maximum), in which we impose sequences fatigue and whose objectives are:

- Determine the laws of fatigue when imposed strain is much higher than those applied in the usual test fatigue.

- Quantify the effect of large amplitudes of strain, which exceed those applied by an axle of 130 kN in road pavements, on the one hand and the effect of multi-peak signals on the other hand (tandem_ $\lambda = 0,25$).

The inclusion of these two parameters can provide answers on this subject, namely:

- The effect of large amplitudes, in order to scan the range of high stress, with cumulative shipments.
- The effect of tandem_0,25 and back to zero between two peaks of loading giving multi-peak loads, compared to the reference sinusoidal loading Figure 5.

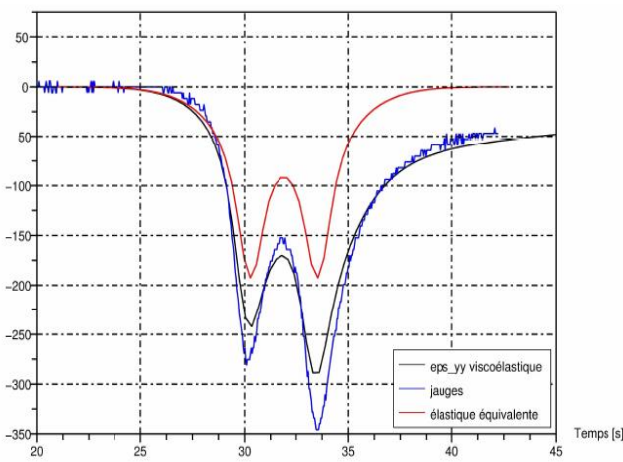


Fig. 4a- Elastic and viscoelastic simulations (Viscoroute) and transversal strain measurements at the bottom of bituminous layers [30]

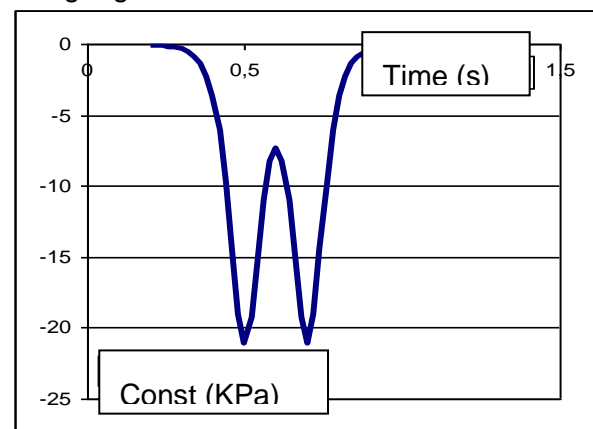


Fig.4b - Simulation of constraints evolution, according to Boussinesq

The imposed stress is measured in the order of 5 – 8 daN. This has been applied in the technical capacity margins of the testing machine, which must not exceed 10 daN.

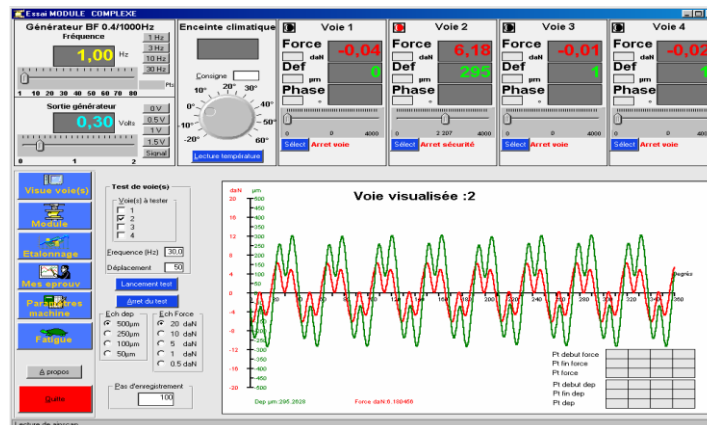


Fig.5 - Exp. Visualisation of the fatigue test

RESULTS

Treatment of raw results

In the literature several approaches are used to determine the fatigue criterion. Results are collected in log file, giving each moment, the imposed strain (ϵ_{moy}), the stress and time. These results are processed in MS Excel to calculate the number of cycles depending on the chosen frequency and the corresponding stiffness. The dispersions are minimal for sine signals by cons in tandem we recorded some dispersion translated by some outliers (in Figure 6), due to the complexity of the signal, the viscoelastic properties and the heterogeneous nature of the material itself.

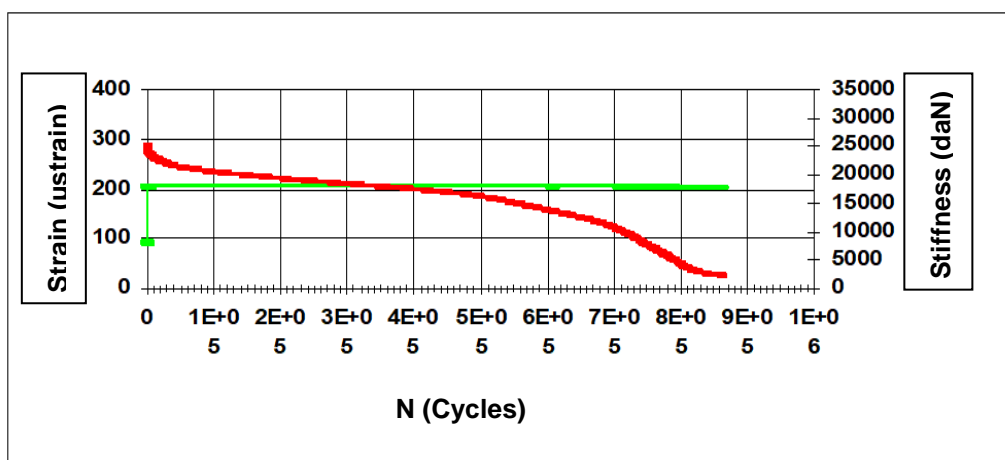


Fig. 6.a - Strain and fatigue curves of SINE Signal

To determine K_0 value, which corresponds to the initial stiffness, we can use a linear regression on the part of the fatigue curve called phase II [31]. In this phase the behaviour is approximately linear, which corresponds to the evolution of stiffness by increase of diffuse damage [32]. K_0 is the intersection of the regression line with Y axis of stiffness.

The phenomenon of fatigue damage (progressive) of bituminous mixes can be evaluated by the damage method on the linear part of the curve, called phase II (in Figure 6b). Along the plateau obtained for the ratio of dissipated energy changes (for the energy approach method). This phase is often reached after phase I of rapid reduction of the initial stiffness, when the material is well heated [14], and before the crack propagation phase III at the micro and macro scales (sudden drop in stiffness which explains the ruin of the material).

The initial stiffness K_0 is a parameter characterizing the material and its response [33], according to the mode and magnitude of the stress.

There are linear relations between the rate of dissipated energy change and the number of load applications to failure without the rest period, showing approximately constant relations even if loading wave pattern is different and there are linear relations between the rate of stiffness change and the number of load applications to failure [34].

According to Molenaar [35], the idea behind the endurance limit principle for asphalt concrete is that there is an applied stress corresponding to " $K_0 / 2$ ", a non-unique, in which it is stated that fatigue does not occur. Fatigue failure results from an accumulation of plastic deformation, which is the case of controlled load. The latter depends on the temperature and the loading rate.

A comparison has been established between the traditional fatigue criteria, where the number of cycles corresponding to 50% of the initial rigidity and that based on energy are sought,

where the number of cycles at the maximum energy ratio or the maximum stiffness of Rowe defined by the stiffness multiplied by the corresponding number of cycles, and the criterion based on the viscoelastic continuum damage (VECD) approach. The latter criterion is defined by the number of loading cycles at the point of inflection of the pseudo-stiffness standardized with respect to the curve of the damage variable. They showed that there is a correlation between the traditional criteria (especially those based on the energy ratio) and the VECD criteria, as well as the relative lifetime of the energy ratio or the maximum stiffness of Rowe is higher than that of fatigue at ($N_f/50\%$). This indicates that the traditional approach is conservative [36].

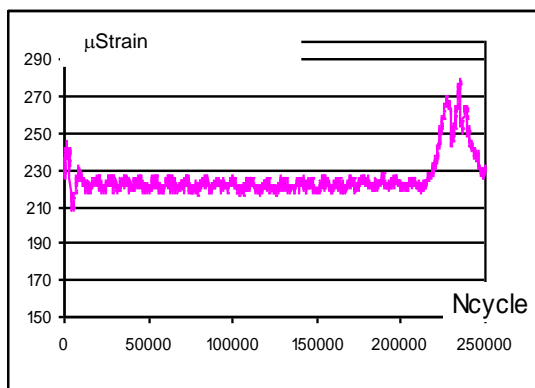


Fig. 6.b1- Strain curve, Tandem $_{\lambda=0,25}$

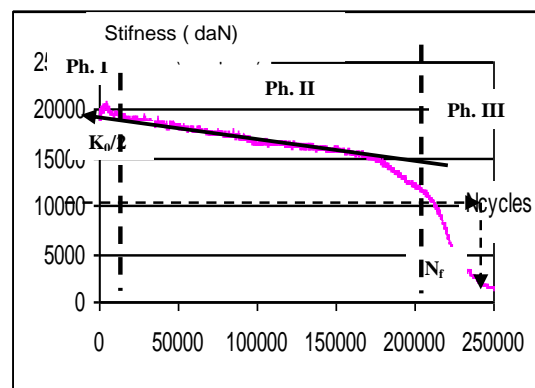


Fig. 6.b2- Fatigue curve, Tandem $_{\lambda=0.25}$

In another approach based on the Crack Meander Technique, Muniandy et al. [37] observed that the Crack Meander method can be used as another way to study fatigue performance by mapping cracks, especially when fatigue resistance is desired. The analysis of the cracks has the tendency of progress of the stresses of traction, with the number of cycles. The sequence corresponding to the maximum value of the tensile strain and the maximum crack (length, area and density) were comparable for the different mixtures tested. The comparison of fatigue performance can be determined by this laboratory approach. The (reinforced) sample that had the longest life obviously showed the macro-crack aspect rather than the micro-crack. However, the control sample (less durable than the previous one) had balanced micro and macro cracks. The sample with the shortest life had more micro-cracks than the other two types of mixtures.

The application of the fuzzy estimation algorithm was developed by Tigdeir et al. [38]. It does not provide an equation but can fit linear or nonlinear shapes with fuzzy subsets of life and strain variables. Taking into account the specific variables of the bituminous mix, by increasing the conditional statements in the fuzzy implications, could increase the accuracy of the estimation of the fatigue life. The fuzzy logic model resembles the results better than the regression model, and has flexible ranges; it may be according to the tests results but this is not the case for the regression model.

Comparison of aggressivity

We calculate the average slopes on all the fatigue curves and the average strain using two different methods (mean of the values obtained directly by recording and the mean by integral). The slope of phase II increases with increasing levels of deformation. However, the third level of strain is the most damaging, under the effect of the signal tandem $_{0.25}$ (average gradient on

phase II in the order of 0.22).

Knowing that the laws of fatigue have always obtained an exponent of about 0.2, this means that the increase of the deformation can be estimated by 2^5 aggressions. It is therefore possible to compare with the values of ε^5 and $d\varepsilon^5/dt$ for both types of loading in question. Three average levels of deformation have been applied for both types of signals:

- Sine at 25Hz : 192 ; 277 ; 386 μ strain
- Tandem_ $\lambda = 0.25$ at 25/3Hz : 235 ; 288 ; 358 μ strain

The average slopes obtained, corresponding to the fatigue curves of each level, are as follows:

- Sine at 25Hz: -0.0143; -0.0330; -0.1118
- Tandem_ $\lambda = 0.25$ at 25/3Hz: -0.0134; -0.0305; -0.1092

By observing the deformation levels close to the two signals as well as the slopes obtained, we can say that the recorded aggressivities are quite close.

Laws of behaviour

The pairs of values (ε_{moy} , N_f) are determined for each waveform, the laws of fatigue can be traced, according to the standard NF 98-261-1. Figure 7 summarizes the results obtained for the two tests.

Fatigue lines of two signals are combined and slopes obtained are close. Given the complexity of signal and the viscoelastic nature of mix, the dispersion is larger for tandem loads especially when the amplitude of deformation is higher. Direct characterization of the behaviour of mix on fatigue depends on the intrinsic behaviour of the tested material [39].

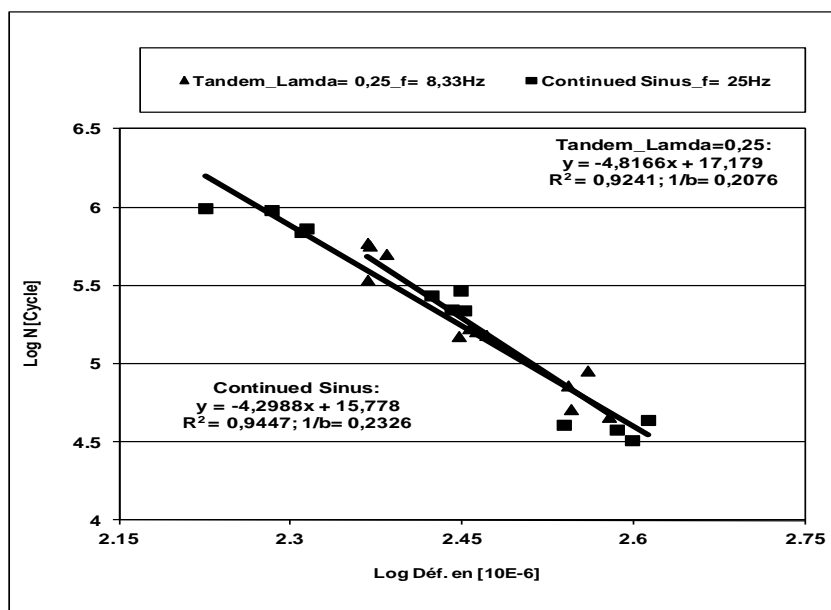


Fig. 7 - Fatigue laws for tandem_0.25 and sine (tandem_1.0)

At high levels of strain, the effect of frequency is significant for conventional mixtures [40]. The low frequencies limit the power dissipation [41]. The magnitude of the stress increases this dissipation, and the phenomenon of heat is related to frequency. The latter plays a more important role in point of view of changes in the stiffness and performance of the mix in terms of life, than evolution of the shape of tandem (from $\lambda = 0.25$ to $\lambda = 1.0$).

From the results mentioned above, one can deduce that the shape of load in tandem has a negligible effect on fatigue response, irrespective of the factor form λ (from $\lambda = 0.25$ to $\lambda = 1.0$). At $f = 25/3$ Hz, the lifetime in tandem is the same as for the sinusoidal loading at $f = 25$ Hz. This means that the increase in λ value (depth of the peak through) has no remarkable effect, since it gives a life very similar or even identical to a sinusoidal with $f = 25$ Hz.

The effect of frequency is minimal on the evolution of complex modulus; linear viscoelastic limit is influenced more by temperature than by frequency [42]. These findings indicate the validity of the approach using the change in frequency for the transition from three sine signals 25Hz to a single tandem 25/3 Hz. When the load time decreases, the fatigue life will increase. This increase is much larger for lower stress (or strain) levels than the higher levels [43]. This is explained in the same sense of the decrease effect in frequency.

However, the combined effects of change in frequency (25 Hz to 25/3 Hz) and change in signal shape (sine for tandem) are fully compensated. It is found that damage caused by the dual-axes is much higher than single axes, for the same strain levels [44]. Fatigues laws confirm previous findings by similar slopes, where the difference only appears from the second decimal place to the order of 3 %. Indeed, testing sinus and tandem_0.25 lead to nearly identical values of ϵ_5 and ϵ_6 , which correspond respectively to 10^5 and 10^6 cycles (Table 2). The material behaviour within the range of large strain (300 to 400 μ strain), under the effect of two types of signals, is very close.

Tab. 1 - Summary table

Signal	Frequency [Hz]	Strain at 10^5 cycles ϵ [μ strain]	Strain at 10^6 cycles ϵ [μ strain]	Slope law of fatigue 1/b
Sine or Tandem_ $\lambda = 1$	25 or 25/3= 8,33	321	187	0,2328
Tandem_ $\lambda = 0,25$	25/3= 8,333	324	200	0,2078

Given the complexity of tandem_0.25 signal and the experimental difficulties (capacity of the testing machine, and the nature of the material) for larger strain, allowing more precision on the laws of fatigue under strain exceeding 350 μ strain, an extrapolation of the fatigue line of this signal in terms of life can easily be obtained by using the sine of fatigue signal. The lowest levels of strain lead to aggression less intense signals.

According to the overall reading of the results obtained, generally the service life is the same in both cases of loading, independently of the form factor λ . One could expect a lifetime that could be similar to that obtained in the case of a sinusoidal signal at a frequency $f = 8.33$ Hz. For the two signals used in the experiments, the fatigue laws have slopes close to 0.2.

The signal in tandem_0.25 is least aggressive. The variation between the peaks is lower and the damage is less different. For tow signals used in the experiments, with regard to the average amplitude (tensile strain) of the loading tandem $\lambda = 0.25$, this last loading is the most aggressive (large tensile period), but we cannot ignore that the frequencies are different between tandem and sine.

It is to highlight that: At the same level of strain the differences are notable, from the point

of view of aggressiveness, between the effect of a high frequency (25Hz) and that of a low frequency (25/3 Hz).

CONCLUSION

- For tandem signal, the change in stiffness is also described in three phases as in the case of ordinary fatigue test (sine). Indeed, the loss of stiffness in phase I is greater in tandem stresses than in sine. However, the tandem_0.25 signal appears more aggressive than the sine signal.
- Large strains in the margin of “300-350 μ strain” for tandem and sine signals, under 5 - 8 daN for stress, give lifetimes in the order of 10^5 cycles.
- According to the obtained results, generally the lifetimes are the same for both loading cases, regardless of the form factor λ . This means that a decrease in the value of λ (depth of the intermediate peak) has no remarkable effect (Tandem $\lambda = 1.0$ vs. Tandem $\lambda = 0.25$). The lifetime for Tandem_ $\lambda = 0.25$ signal at $f = 8.33$ Hz could be similar to that obtained in the case of a sinusoidal signal at $f = 25$ Hz. For tow signals used in the experiments, the fatigue laws have slopes (1/b) in the order of 0.2.
- The frequencies are different between tandem and sine. Since, we find the aggressive role of the highest frequencies. The signal of tandem_0.25 is more aggressive than the signal of sine. It is to highlight that: At the same level of strain the differences are notable, from the point of view of aggressiveness, between the effect of a relatively high frequency of sine (at 25Hz) and that of a low frequency of tandem (at 25/3 Hz).
- A signal tandem ($\lambda = 0.25$) at 25/3 Hz is almost equivalent to three signals sine at 25Hz. It can be noted that at the strain levels tested the passage of one tandem axle is equivalent to the passage of three single axles.
- For tow signals used, with regard to the average amplitude of the loading tandem $\lambda = 0.25$ (in the meantime of tensile strain), this last loading is the most aggressive (large tensile period).
- These tests presented a different view compared to traditional fatigue tests. Further improvements can be considered, to establish more extended tandem fatigue models, taking into account the effect of temperature, higher strain: levels, frequency variation, the combination of loading.

ACKNOWLEDGEMENTS

The author wish to acknowledge the following persons for their support and help in this study;

- Pr D. Breyse, I2M Institute, Bordeaux-1 University, France.
- Technical staff for Regional Laboratory “LRPC-Bordeaux”, and IFSTTAR-Center, Nantes, France.

REFERENCES

- [1] Francis Kuhn: LTN Innovation dans les transports guides urbains et régionaux, les infrastructures des systèmes de transport urbain de surface, INRETS, 1er S PFI, 20 mai 2005.
- [2] Guide technique - Conception et dimensionnement et structures et chaussée- ISBN: 2-7208-7010-2_ SETRA-LCPC 01/12/1994
- [3] Thomas D. Gillespie, S. M. Karamihas, M. W. Sayers, M. A. Nasim, M. A., W. Hansen & N. Ehsan: Effect of heavy-vehicle characteristics on pavement response and performance, National Cooperative Highway Research Program, NCHRP Report 353, Transportation Research Board, National Research Council, 1993.

- [4] E. Riahi, F. Allou, F. Dubois, L. Ulmet, J. Absi, C. Petit : Etude de la variation des champs mécaniques et thermique dans le béton bitumineux lors de chargement cyclique, 22ème Congrès Français de Mécanique Lyon, 24 au 28 Août 2015.
- [5] N. Amoo and N. Thorpe: A Pavement Damage Based System for Charging HGVS for their Use of Road Infrastructure, Highway Workshop, Univ. of Bergamo, 26-27 Nov. 2004.
- [6] Genevieve Giuliano, *Robert E. Skinner*: Commercial Truck and Bus Safety, Highway/Heavy Vehicle Interaction, A Synthesis of Safety Practice 3, Townes, Transportation Research Board of the National Academies, Executive Committee, pp. 54-58, March 2003.
- [7] Ghazi El Khateeb: Fatigue Performance: Asphalt Binders versus Full-Scale Pavement. Canadian Journal of Transportation-Vol 2, N° 1, 2008.
- [8] A. Chabot, O. Chupin, L. Deloffre & D. Duhamel: ViscoRoute 2.0, a tool for the simulation of moving load effects on asphalt pavement. Road Materials and Pavement Design, 11(2), 227–250. (2010).
- [9] H. U. Bahia, H. Ihai Karen, B. Sadi Kose: Non-Linear Viscoelastic and Fatigue Properties of Asphalt Binders. The Asphalt Research Group Department of Civil and Environmental Engineering. Univ. of Wisconsin-Madison Madison, WI 53706. A. M. of the AAPT 1999.
- [10] X. Hu, F. Zhou, S. Hu & L. F. Walubita: Proposed loading waveforms and loading time equations for mechanistic-empirical pavement design and analysis. Journal of Transportation Engineering, 136(6), 518-527(2010)..
- [11] Nuha Salim Mashaan, Mohamed Rehan Karim, Mahrez Abdel Aziz, Mohd Rasdan Ibrahim, Herda Yati Katman, and Suhana Koting : Evaluation of Fatigue Life of CRM-Reinforced SMA and Its Relationship to Dynamic Stiffness. ScientificWorldJournal. doi: 10.1155/2014/968075; 2014: 968075.
- [12] I. L. Al-Qadi, P. J. Yoo, M. A. Elseifi, and Ibrahim Janajreh: Effects of Tire Configurations on Pavement Damage. Conference: Asphalt Paving Technology: Association of Asphalt Paving Technologists- Proceedings of the Technical Sessions. AAPT- 2005.
- [13] Imad. L. Al-Qadi, W. Xie, and M. A. Elseifi,: Frequency determination from vehicular loading time pulse to predict appropriate complex modulus in MEPDG. Electron. J. Assoc. Asph. Paving Technol., 77, 739–772. 2008.
- [14] E. Riahi, F. Allou, F. Dubois, L. Ulmet, J. Absi, C. Petit : Etude de la variation des champs mécaniques et thermique dans le béton bitumineux lors de chargement cyclique, 22ème Congrès Français de Mécanique Lyon, 24 au 28 Août 2015.
- [15] M. Merbouh: Contribution to modeling of the rheological behavior of mix Asphalt, Influence of extreme conditions of temperature and traffic on fatigue. PhD, Mechanic and Engineering. December 21, 2010. University Bordeaux 1. French.
- [16] R. D. Barksdale Partical application of fatigue and rutting tests on bituminous base mixes. Asphalt Paving Technol. 1978;47:115–159.
- [17] A. A. Tayebali, J. A. Deacon, J. S. Coplantz, et al.: Mix and mode-of-loading effects on fatigue response of asphalt-aggregate mixes"Proceedings of the Association of Asphalt Paving Technologists, vol. 63, p.118–151, 1994.
- [18] Hasan Ziari, Rezvan Babagoli, Mahmoud Ameri, Ali Akbari: Evaluation of fatigue behavior of hot mix asphalt mixtures prepared by bentonite modified bitumen. ScienceDirect Journal of Construction and Building Materials 68 (2014) 685–69.
- [19] Umme Amina Mannan, Md Rashadul Islam, Rafiqul A. Tarefder: Effects of recycled asphalt pavements on the fatigue life of asphalt under different strain levels and loading frequencies. International Journal of Fatigue 78 (2015) 72–80.
- [20] Amin Lotfi-Eghlim, Mohammad Saied Karimi: Fatigue behavior of hot mix asphalt modified with nano al2 o3 –an experimental study. Advances in Science and Technology Research Journal. Vol. 10, No. 31, Sept. 2016, pages 58–63 DOI: 10.12913/22998624/64011.
- [21] R. V. Siddharthan, J. Yao, Peter E. and Sebaaly: Pavement strain from moving dynamic 3d load distribution. Journal Transp. Eng. 1998.124:557-566/ Nov./Dec. 1998.
- [22] Denis Duhamel, Armelle Chabot, Philippe Tamagny, Larbi Harfouche : « *VISCOROUTE* » Viscoelastic Modeling Software for Asphalt Pavements. Bulletin des laboratoires des ponts et chaussées - 258-259 Oct./Nov./Dec. 2005 - réf. 4538 - pp. 89-103.
- [23] L. F. Walubita, G. S. Simate, E. Ofori-Abebresse, E. Martin Amy, R. L. Lytton, L. E. Sanabria: Mathematical formulation of HMA crack initiation and crack propagation models based on continuum fracture-mechanics and work-potential theory. doi.10.1016/j.ijfatigue.2011.12.020. Int. Journal of Fatigue. Vol.40, July 2012, pp. 112-119.

- [24] P. Cao, C. Zhou, D. Feng, Y. Zhao and B. Huang: A 3D Direct Vehicle-Pavement Coupling Dynamic Model and Its Application on Analysis of Asphalt Pavement Dynamic Response. Article ID 394704, doi.org/10.1155/2013/394704, Vol 2013. Hindawi PC Mathematical Problems in Engineering.
- [25] M. Boudabbous, A. Millien, C. Petit, J. Neji: Energy approach for the fatigue of thermoviscoelastic materials: Application to asphalt materials in pavement surface layers. ScienceDirect, International Journal of Fatigue 47 (2013) 308–318
- [26] G. Al-Khateeb, & K. A. Ghuzlan,: The combined effect of loading frequency, temperature, and stress level on the fatigue life of asphalt paving mixtures using the IDT test configuration. International Journal of Fatigue, 59, 254-261. (2014)
- [27] C. De La Roche: Module de rigidité et comportement en fatigue des enrobés bitumineux, Thèse de doctorat, Ecole centrale Paris, 1996.
- [28] A. Chabot, P. Tamagny, D. Duhamel, D. Poché: Visco-elastic modeling for asphalt pavements – software ViscoRoute, 10th ICAP, 12-17 August, Québec, Canada, 2006.
- [29] LCPC / AIRBUS / STBA A380 Pavement Experimental Program (PEP), AIRBUS INDUSTRIE, A380 Programme, Toulouse, France 25th October 2001.
- [30] A. Chabot, Tamagny P., D. Duhamel, D. Poché: Visco-elastic modeling for asphalt pavements – software ViscoRoute » 10th International Conference on Asphalt Pavements, 12-17 August (2006), Québec, Canada.
- [31] H. Omrani, A. Tanakizadeh, A. R. Ghanizadeh, M. Fakhri: Investigating different approaches for evaluation of fatigue performance of warm mix asphalt mixtures, Materials and Structures, Apr.2017.
- [32] D. Perraton, H. Baaj, H. D. Benedetto et M. Paradis: Évaluation de la résistance à la fatigue des enrobés bitumineux fondée sur l'évolution de l'endommagement du matériau en cours d'essai, aspects fondamentaux et application à l'enrobé à matrice de pierre, Canadian Journal of Civ. Eng. pp 902-913. 30(5): 902–913 (2003), doi:10.1139/I03-067.CNRC Canada.
- [33] I. Hafeez, M. A. Kamal, M. W. Mirza, Bilal S. Barkatullah: Laboratory fatigue performance evaluation of different field laid asphalt mixtures. Constr Build Mater 44:792–797 (2013).
- [34] K. Kogo, K. Himeno : The effects of different waveforms and rest period in cyclic loading on the fatigue behavior of the asphalt mixtures, DOI10.1201/9780203882191.ch50. June 2008, DOI10.1201/9780203882191.ch50
- [35] A. Molenaar: Prediction of Fatigue Cracking in Asphalt Pavements: Do We Follow the Right Approach? Transportation Research Record: Journal of the Transportation Research Board, Volume 2001, D.C., 2007, pp. 155–162. Doi: 10.3141/2001-17.
- [36] Rafiqul A. Tarefder, Damien Bateman, Aravind K. Swamy: Comparison of fatigue failure criterion in flexural fatigue test, ijf2013. Int. Journal of Fatigue 55 (2013) 213–219
- [37] Ratnasamy Muniandy, Nor A. Binti Che Md Akhir, S. Hassim, D. Moazami: Laboratory Fatigue Evaluation of Modified and Unmodified Asphalt binders in Stone Mastic Asphalt Mixtures using a newly Developed Crack Meander Technique. DOI: http://dx.doi.org/10.1016/j.ijfatigue, Ref.: International Journal of Fatigue 3198 (2014).
- [38] Mesut Tigdemir, Mustafa Karasahin, Zekai Sen : Investigation of fatigue behaviour of asphalt concrete pavements with fuzzy-logic approach. doi.org/10.1016/S0142-1123(01)00183-9. International Journal of Fatigue 24 (2002) 903–910
- [39] D. Bodin, C. de La Roche, J-M. Piau and Gilles Pijaudier-Cabot: Prediction of the intrinsic damage during bituminous mixes fatigue tests, RILEM Syposium Zurich, 2003.
- [40] Mansour Fakhria, Kaveh Hassania, Ali Reza Ghanizadeh: Impact of loading frequency on the fatigue behavior of SBS modified asphalt mixtures. Elsevier Procedia - Social and Behavioral Sciences 104 (2013) 69 – 78
- [41] Nicole Rivière: Comportement en fatigue des enrobés bitumineux, Thèse de doctorat, Université de Bordeaux1, 1996.
- [42] A. Carter, D. Perraton: La mesure du module complexe des enrobés bitumineux, 2nd Material Specialty Conference of the CSCE, Montréal, Québec, Canada Jun 5-8, 2002.
- [43] U. A. Mannan, Md Rashadul Islam, Rafiqul A. Tarefder: Effects of recycled asphalt pavements on the fatigue life of asphalt under different strain levels and loading frequencies. International Journal of Fatigue 78 (2015) 72–80.
- [44] H. K. Salama; K. Chatti: Evaluation of fatigue and rut damage prediction methods for asphalt concrete pavements subjected to multiple axle loads, International Journal of Pavement Engineering, DOI: 10.1080/10298430903578978. 05 March 2010.

WATER HAMMER IN PIPELINE WITH DIFFERENT CHARACTERISTICS OF VALVE CLOSING AND UNSTEADY WALL FRICTION

Haixiao Jing, Wen Wang and Guodong Li

State Key Laboratory of Eco-hydraulics in Northwest Arid Region of China (Xi'an University of Technology), Xi'an, China; jinghx@xaut.edu.cn

ABSTRACT

This paper presents an analytical investigation of water hammer pressure variation in a reservoir-pipe-valve system. Laplace transform method is used to get the analytical solutions for different characteristics of the valve closing. Specifically, sudden valve closing and piecewise linear closing are used, the latter can be treated as approximated arbitrary characteristics of valve closing. Unsteady wall friction is also included. The new solutions compare well with the previous experimental data. The results show that this solution is suitable for water hammer with laminar and low Reynolds number turbulent unsteady flow. The effects of different characteristics of the valve closing on the water hammer pressure variations are also studied. This solution can be a better choice for optimization of valve closing to reduce the maximum water hammer pressure.

KEYWORDS

Water hammer; Laplace transform; Valve closing laws; Unsteady wall friction

INTRODUCTION

Water hammer frequently occurs in pressure pipelines when fluid in motion is forced to stop in a short time. Extreme high and low pressures alter in the process. This phenomenon presents a major problem for practical hydraulic systems, such as bursts of pipe and intrusion of contaminated water. More than 80% of breakdowns in water supply systems can be attributed to water hammer phenomenon [1]. Numerous investigations have been carried out for this problem, which can be traced back to 19th century. Steady state wall friction based on Darcy-Weisbach formula is used widely in classical one dimensional water hammer equations. However, due to the nonlinearity of friction term, numerical methods are applied extensively to solve these equations numerically. While unsteady wall friction is found to be important and two types of unsteady wall friction models are developed. One is the model developed firstly by Zielke [2], in which the unsteady wall friction is represented by a convolution term. The other is the one by Brunone et al.[3] where unsteady wall friction is related to instantaneous mean flow, instantaneous local acceleration and instantaneous convective acceleration. After that, many investigations have been carried out to extend the unsteady friction model to turbulent flow [4]. To get the solution of the water hammer model, most of the studies have focused on the development of numerical models by method of characteristics, such as Bergant et al.[5]. Other numerical methods, such as finite volume method [6] are also used for this problem. Yao et al.[7] investigated the attenuation of water hammer pressure by a time-varying valve closure by multiple scale asymptotic method. Ghidaoui et al.[8] have made good review about the theoretical and practical aspects of water hammer.

An important objective of water hammer analysis is the prediction of water hammer pressure and reduction (or control) of the pressure during water hammer process. Several methods can be used to reduce water hammer pressure, including: 1) optimization of the operation

of the pipe system, 2) modification of existing infrastructure and 3) installation of protection devices, such as relief valve [9]. Previous studies have shown that the pattern of water hammer pressure is strongly dependent on the duration of valve closure and changes of valve operation can reduce water hammer pressure significantly [10]. Azoury et al.[11] studied the effects of valve closure schedule on water hammer by method of characteristics. Provenzano et al.[12] derived analytical solutions for different closing function without considering wall friction.

In recent years, accurate control of water hammer pressure is revisited by optimizing the valve operation using optimization models. Bazargan-Lari et al.[13] optimized closing valve rule curve by using a multi-objective optimization model and Bayesian networks. Chen et al.[14] obtained optimal parameter selection of valve closing using nonlinear optimization techniques. Bohorquez and Saldarriaga [9] proposed a methodology for obtaining the optimal valve closure curves in water distribution systems in Bogota, Colombia. Numerical methods are used to solve water hammer equations in all these optimization studies. While Cao et al.[15] derived a travelling wave solution and solved the extremum of the function by Ritz method to realize the accurate control of water hammer in pipes. However, the wall friction is neglected in their study. Optimal flow control of water hammer requires a forecasting model capable of predicting the non-uniform and unsteady water flow in space and time [14]. Analytical solution is still very useful because it helps to reach clear and in-depth physical understanding and also to provide sufficiently simple yet general and accurate tool for practical prediction and control [16]. However, previous analytical studies of water hammer are confined to sudden valve closing and frictionless pipe.

In this study, analytical solutions for water hammer with unsteady friction and different valve closing laws are derived. Laplace transform method is employed for this purpose. The rest of the paper is structured as follows. Firstly, the governing equations are briefly described and dimensionless variables are introduced. Then, analytical solution for any type of closing valve laws is derived by using Laplace transform. Two special solutions for sudden closing law and piecewise linear closing law are obtained. Unsteady wall friction is then included by following reference [17]. The analytical results are validated by comparing with experimental data. The effects of different closing laws on pressure variations are studied by using the analytical solution. Method of transforming the profile of velocity decrease at valve end to variation of valve opening is also presented. Finally, some conclusions are drawn.

METHODS

Governing equations

A simple reservoir-pipe-valve system is considered in this study, as is shown in Figure 1. After the closing of the valve, the governing equation for the perturbed flow velocity $u(x,t)$ and dynamic pressure $p(x,t)$ are as follows:

$$\frac{1}{\rho_0 c^2} \frac{\partial p}{\partial t} + \frac{\partial u}{\partial x} = 0 \quad (1)$$

$$\frac{\partial u}{\partial t} + \frac{1}{\rho_0} \frac{\partial p}{\partial x} = -\frac{2}{\rho_0 R} \tau_w \quad (2)$$

Where, ρ_0 is the unperturbed fluid density, c is the pressure wave velocity which is dependent on the compressibility of fluid and pipe wall. R is the inner radius of pipe and τ_w denotes the wall shear stress. In the literature of hydraulics, steady state wall friction based on Darcy-weisbach formula is often used [8]. While unsteady wall friction is also proposed and proved to be important for water hammer phenomenon [18].

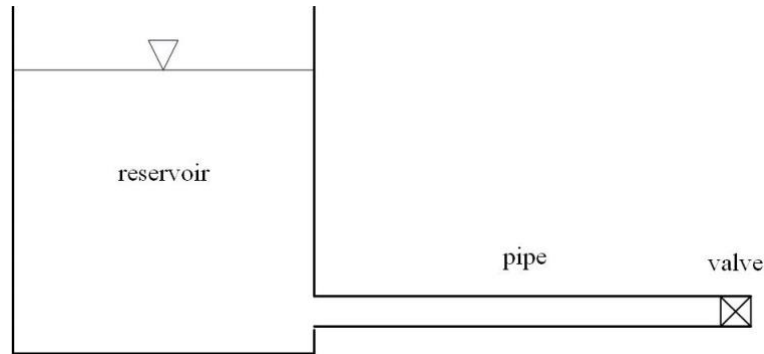


Fig. 1 - Sketch of the pipeline system

Boundary condition (BC) at reservoir end ($x = 0$) is:

$$p(x, t) = 0, \quad x = 0 \quad (3)$$

This represents the constant pressure head at reservoir. While at valve end ($x = L$), BC becomes

$$u(x, t) = U(t), \quad x = L \quad (4)$$

Or

$$\frac{\partial p}{\partial x} = -\rho_0 \frac{\partial u}{\partial t} = -\rho_0 \frac{dU}{dt} = f(t), \quad x = L \quad (5)$$

Where, Equation(2) without wall friction has been used. $U(t)$ represents the valve closing law.

Initial conditions (ICs) for this problem are:

$$p(x, t) = 0, \quad t = 0 \quad (6)$$

$$\frac{\partial p}{\partial t} = 0, \quad t = 0 \quad (7)$$

Numerical methods, such as method of characteristics, finite volume method etc., are widely used to solve the above governing equations [5]. In hydraulic engineering, dynamic pressure $p(x, t)$ for water hammer has received more attention. In order to get analytical solution of $p(x, t)$, we will separate the two unknowns $u(x, t)$ and $p(x, t)$.

After cross differentiation of Equation (1) and (2), we can eliminate $u(x, t)$ and obtain

$$\frac{\partial^2 p}{\partial x^2} - \frac{1}{c^2} \frac{\partial^2 p}{\partial t^2} = -\frac{2}{R} \frac{\partial \tau_w}{\partial x} \quad (8)$$

This is the governing equation for dynamic pressure $p(x, t)$ of water hammer. The BCs and ICs keep unchanged as above.

For simplicity, dimensionless variables are introduced as in [17]

$$u^* = \frac{u}{U_0}, p^* = \frac{p}{\rho_0 c U_0}, t^* = \frac{t}{L/c}, x^* = \frac{x}{L}, \tau_w^* = \frac{\delta \tau_w}{\rho_0 \nu U_0} \quad (9)$$

Where, * denotes the dimensionless variables, $\delta = \sqrt{\nu L/c}$ is the characteristic thickness of the Stokes oscillatory boundary layer. ν denotes the kinematic viscosity of fluid. Then the dimensionless governing equation for pressure, ICs and BCs become

$$\frac{\partial^2 p^*}{\partial x^{*2}} - \frac{\partial^2 p^*}{\partial t^{*2}} = -\frac{2\delta}{R} \frac{\partial \tau_w^*}{\partial x^*} \quad (10)$$

ICs at $t^* = 0$ become

$$p^*(x^*, t^*) = 0, \quad \frac{\partial p^*(x^*, t^*)}{\partial t^*} = 0 \quad (11)$$

BCs become

$$p^*(x^*, t^*) = 0, \quad x^* = 0 \quad (12)$$

$$\frac{\partial p^*}{\partial x^*} = -\frac{\partial u^*}{\partial t^*} = f(t^*), \quad x^* = 1 \quad (13)$$

From now on, * will be omitted for all dimensionless variables for brevity.

Solution by integral transform method for arbitrary closing laws

After neglecting the wall shear stress and taking Laplace transform for the governing equation and BCs, we get:

$$\frac{\partial^2 \bar{p}}{\partial x^2} - s^2 \bar{p} = 0, \quad 0 < x < 1 \quad (14)$$

BCs:

$$\bar{p} = 0, \quad x = 0 \quad (15)$$

$$\frac{\partial \bar{p}}{\partial x} = F(s), \quad x = 1 \quad (16)$$

Where, ICs have been used and

$$\bar{p}(x, s) = \int_0^\infty e^{-st} p(x, t) dt, \quad p(x, t) = \frac{1}{2\pi i} \int_\Gamma e^{st} \bar{p}(x, s) ds \quad (17)$$

$F(s)$ is the Laplace transform of $f(t)$.

The above ordinary differential equation can be easily solved, the solution is:

$$\bar{p}(x, s) = F(s) \frac{\sinh(sx)}{s \cosh(s)} \quad (18)$$

Define

$$G(x, s) = \frac{\sinh(sx)}{s \cosh(s)} \quad (19)$$

Hence, $p(x, t)$ can be obtained after inverse Laplace transform

$$\begin{aligned} p(x, t) &= \frac{1}{2\pi i} \int_\Gamma e^{st} F(s) G(x, s) ds \\ &= f(t) * g(t) = \int_0^t f(t') g(t-t') dt' \end{aligned} \quad (20)$$

Where, convolution theorem has been used. $g(t)$ is the inverse Laplace transform of $G(s)$ and can be obtained as below.

$$g(t) = \frac{1}{2\pi i} \int_\Gamma e^{st} G(s) ds = \frac{1}{2\pi i} \int_\Gamma e^{st} \frac{\sinh(sx)}{s \cosh(s)} ds \quad (21)$$

For the integral above, simple poles at:

$$s = i \frac{(2m+1)\pi}{2} = ik_m, \quad m = 0, \pm 1, \pm 2, \pm 3, \dots \quad (22)$$

By Cauchy's residue theorem, we get:

$$\begin{aligned} g(t) &= \sum_{m=-\infty}^{\infty} \frac{e^{ik_m t} \sinh(ik_m x)}{ik_m \sinh(ik_m)} = \sum_{m=-\infty}^{\infty} \frac{1}{ik_m} \frac{\sin(k_m x)}{\sin(k_m)} e^{ik_m t} \\ &= \sum_{m=0}^{\infty} \frac{2 \sin(k_m x)}{k_m \sin(k_m)} \sin(k_m t) \end{aligned} \quad (23)$$

Where, $k_{-(m+1)} = -k_m$ has been used.

Finally, for given valve closing law $f(t)$, we can get $p(x, t)$ from Equation (20).

Two special closing laws with unsteady friction

From the boundary condition at valve end Equation(5), different $f(t)$ represent different characteristics of valve closing. In this section, two valve closing laws, these are sudden closing and piecewise linear closing, are studied. Also, unsteady friction is included in the results by following [17].

Sudden valve closing

For this case, the dimensionless BC at valve end ($x = 1$) for $u(x, t)$ is

$$u(t) = 1 - H(t) \quad (24)$$

Where, $H(t)$ is Heaviside step function.

Hence, $p(x, t)$ at valve end ($x = 1$) can be obtained

$$\frac{\partial p}{\partial x} = -\frac{\partial u}{\partial t} = \delta(t) \quad (25)$$

Where, $\delta(t)$ is Dirac delta function.

So, we have $f(t) = \delta(t)$. From Equation (20), the pressure p can be calculated:

$$\begin{aligned} p(x, t) &= \int_0^t f(t') g(t-t') dt' \\ &= \int_0^t \delta(t') \sum_{m=-\infty}^{\infty} \frac{1}{ik_m} \frac{\sin(k_m x)}{\sin(k_m)} e^{ik_m(t-t')} dt' \\ &= \sum_{m=-\infty}^{\infty} \frac{1}{ik_m} \frac{\sin(k_m x)}{\sin(k_m)} \int_0^t \delta(t') e^{ik_m(t-t')} dt' \\ &= \sum_{m=-\infty}^{\infty} \frac{1}{ik_m} \frac{\sin(k_m x)}{\sin(k_m)} e^{ik_m t} \end{aligned} \quad (26)$$

Considering the fact that the time scale of wall friction is much longer than one water hammer pressure cycle, Mei and Jing[17] included unsteady wall friction in their formula by introducing a slow vary parameter $P_m(t)$. $P_m(t)$ can be explicitly expressed by using asymptotic method of multiple scales and boundary layer theory. In this study, unsteady wall friction is included by following exactly the method but not repeat here for simplicity. The final dimensionless result becomes:

$$p(x, t) = \sum_{m=-\infty}^{\infty} P_m(t) e^{ik_m t} \frac{\sin(k_m x)}{ik_m \sin(k_m)} \quad (27)$$

$$P_m(t) = e^{-\lambda_m \varepsilon t}, \quad \lambda_m = (1 + i \operatorname{sgn}(k_m)) \sqrt{\frac{|k_m|}{2}} \quad (28)$$

And $\operatorname{sgn}(k_m)$ denotes the sign of k_m . $\varepsilon = \delta/R$ is a small dimensionless parameter. δ has been defined in above section.

Piecewise linear valve closing

We can approximate any closing curve by using piecewise linear lines. So dimensionless boundary condition at valve end ($x = 1$) for u becomes:

$$u(t) = \begin{cases} a_1 t + b_1, & t_0 < t < t_1 \\ \dots \\ a_n t + b_n, & t_{n-1} < t < t_n \\ \dots \\ a_N t + b_N, & t_{N-1} < t < t_N \\ 0, & t > t_N \end{cases} \quad (29)$$

Where, a_n and b_n are coefficients to be determined. And the following constraints must be required.

$$u(t) = \begin{cases} 1, & t = 0 \\ 0, & t = t_c \end{cases} \quad (30)$$

Besides, $u(t)$ must be continuous.

Similarly, BC at valve end for p becomes:

$$\frac{\partial p}{\partial x} = -\sum_{n=1}^N a_n [H(t-t_{n-1}) - H(t-t_n)] \quad (31)$$

Hence,

$$f(t) = -\sum_{n=1}^N a_n [H(t-t_{n-1}) - H(t-t_n)] \quad (32)$$

Finally, solution of pressure p becomes:

$$\begin{aligned} p(x,t) &= \int_0^t f(t') g(t-t') dt' \\ &= \int_0^t (-1) \sum_{n=1}^N a_n [H(t'-t_{n-1}) - H(t'-t_n)] \sum_{m=-\infty}^{\infty} \frac{1}{ik_m} \frac{\sin(k_m x)}{\sin(k_m)} e^{ik_m(t-t')} dt' \\ &= -\sum_{m=-\infty}^{\infty} \frac{1}{ik_m} \frac{\sin(k_m x)}{\sin(k_m)} \sum_{n=1}^N a_n \int_0^t [H(t'-t_{n-1}) - H(t'-t_n)] e^{ik_m(t-t')} dt' \\ &= -\sum_{m=-\infty}^{\infty} \frac{1}{ik_m} \frac{\sin(k_m x)}{\sin(k_m)} e^{ik_m t} \sum_{n=1}^N a_n I_{mn} \end{aligned} \quad (33)$$

Where,

$$I_{mn} = \begin{cases} 0, & t < t_{n-1} \\ \frac{-1}{ik_m} [e^{-ik_m t} - e^{-ik_m t_{n-1}}], & t_{n-1} < t < t_n \\ \frac{-1}{ik_m} [e^{-ik_m t_n} - e^{-ik_m t_{n-1}}], & t > t_n \end{cases} \quad (34)$$

Similarly, the unsteady wall friction can be included and the final dimensionless form of $p(x,t)$ becomes:

$$\begin{aligned} p(x,t) &= \int_0^t f(t') g(t-t') dt' \\ &= -\sum_{m=-\infty}^{\infty} e^{-\lambda_m \varepsilon t} e^{ik_m t} \frac{1}{ik_m} \frac{\sin(k_m x)}{\sin(k_m)} \sum_{n=1}^N a_n I_{mn} \end{aligned} \quad (35)$$

Where, λ_m and ε are the same as in above section.

RESULTS

Validation of unsteady friction with experiments by Bergant et al.

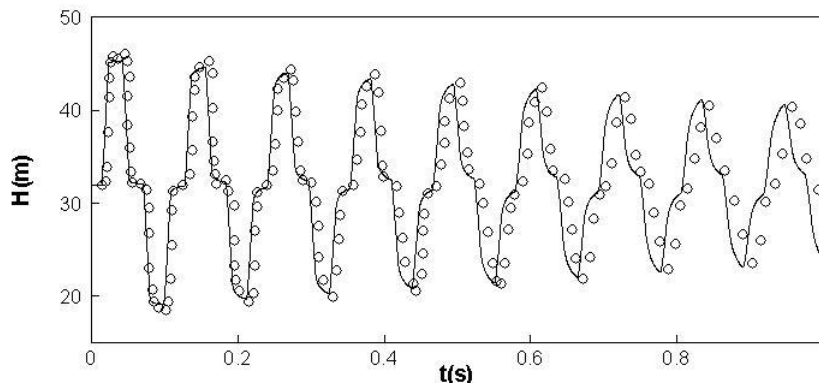
In order to validate the reliability of analytical result for unsteady friction of water hammer, three experimental results by Bergant et al.[18] for laminar and low Reynolds turbulent water hammer flow are used to compare with analytical results. The experimental setup is as follows. A straight long sloping copper pipe with length $L = 37.23\text{m}$, diameter $d = 22.1\text{mm}$ is connected with two water tanks at both ends, the pressure head at upstream end is constant $H = 32\text{m}$ and a fast closing valve at downstream end is installed. The pipe slope is constant at 5.45%. The pressure head at downstream end is changed to achieve required steady velocity or Reynolds number.

Three cases with steady state velocities $U_0 = 0.1, 0.2, 0.3 \text{ m/s}$ are carried out. The Reynolds numbers are 1870, 3750, 5600, respectively. Valve closing time $t_c = 0.009 \text{ s}$ for all three cases, which is $t_c^* = t_c c / L = 0.3189$ for dimensionless closing time. Linear closing law will be used in all three cases. Water hammer wave velocity is $c = 1319 \text{ m/s}$. Pressure variations at two different locations ($x = 0.5$ at the middle section of the pipe and $x = 1$ at valve end) are recorded.

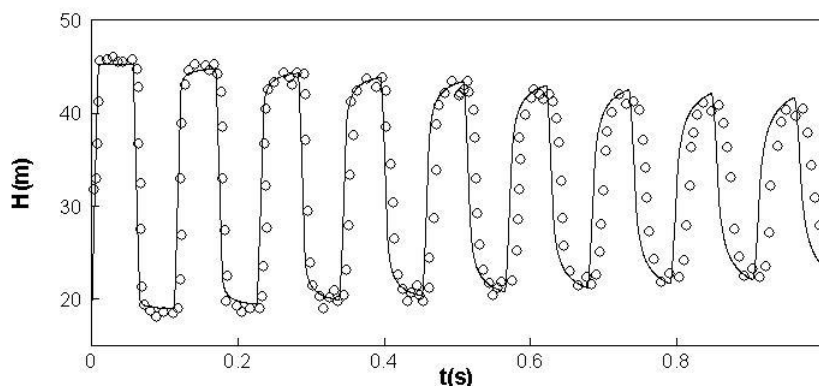
The results can be found in Figures 2, 3 and 4. Good agreement with experimental data can be found in the first several cycles for all three cases. While with the time increases, slight phase advance appears for three cases. Amplitude decay rates for all three cases are also well captured. For quantitative analysis, it is easy to obtain that $t_c < 2L/c$ for all three cases, which means that valve is closed completely before water hammer pressure reflects back to the valve. Hence the maximum pressure head occurs during the first period and the value can be obtained theoretically from Joukowsky's formula, these are 45.45m, 58.89m and 72.34m for three cases (note that the initial pressure head has been added). For case 1, the maximum pressure heads of experimental and analytical results are 46.04m, 45.23m at $x = 0.5$ and 45.84m, 45.29m at $x = 1.0$. For case 2, the maximum pressure heads of experimental and analytical results are 58.59m, 58.47m at $x = 0.5$ and 58.05m, 58.57m at $x = 1.0$. For case 3, the values are 71.55m, 72.48m at $x = 0.5$ and 71.70m, 71.86m at $x = 1.0$. Both experimental and analytical results are very close to the theoretical ones. It can be found that for all the cases the maximum pressure heads of experimental results at valve end ($x = 1.0$) are slightly lower than the values at the middle section ($x = 0.5$) due to the line packing effect, while this phenomenon cannot be found from the analytical results. This is due to the fact, that the line packing effect, which can cause slightly rise of maximum pressure, is neglected in the derivation of the analytical solutions.

More importantly, for the phase difference, it can be obtained from case 1 that the times of the last pressure crests (the 9th pressure period) of experimental and analytical results are 0.958s, 0.947s at the middle cross section ($x = 0.5$), and 0.911s, 0.905s at $x = 1.0$. The times of phase advance are 0.011s and 0.006s which are 9.7% and 5.3% of the water hammer period ($4L/c$). For case 2, the phase advance are 8.86% and 7.45% of the water hammer period at sections $x = 0.5$ and $x = 1.0$, respectively. And for case 3, the phase advance are 6.95% and 7.01% of the water hammer period at sections $x = 0.5$ and $x = 1.0$, respectively. The reason of this phase advance is probably due to error of the valve closing time. As is found in [19], the phase advance of water hammer pressure can be observed with the decrease of valve closing time. The time of valve closure in the experiments is 0.009s, which is relatively small and measurement error is difficult to avoid.

In general, the accuracy of this analytical solution is acceptable. The unsteady wall friction used in this study is proved to be suitable for water hammer with laminar flow and low Reynolds number turbulent flow, although it is derived from laminar boundary layer theory in [17].

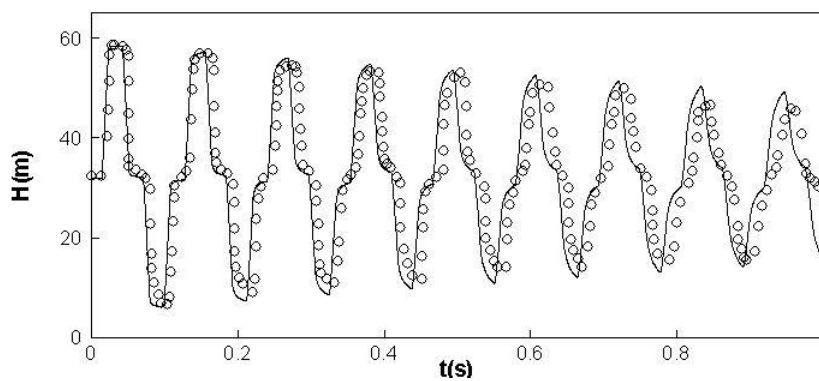


(a) $x = 0.5$



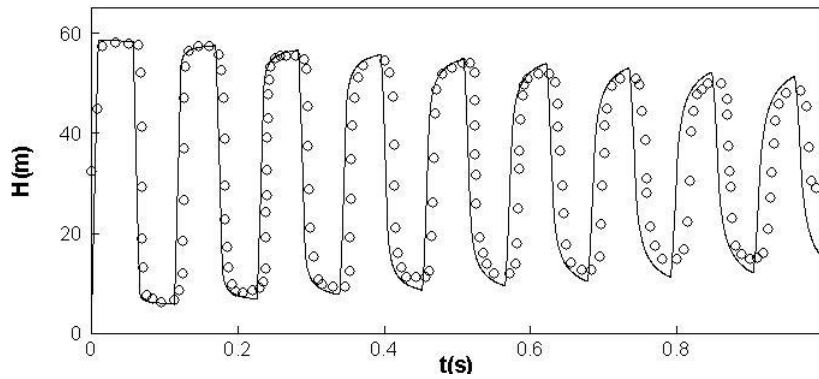
(b) $x = 1.0$

Fig. 2 - Comparison of analytical results with experimental data by Bergant et al.[18] for case 1. Solid lines (analytical results), circles(experimental data).



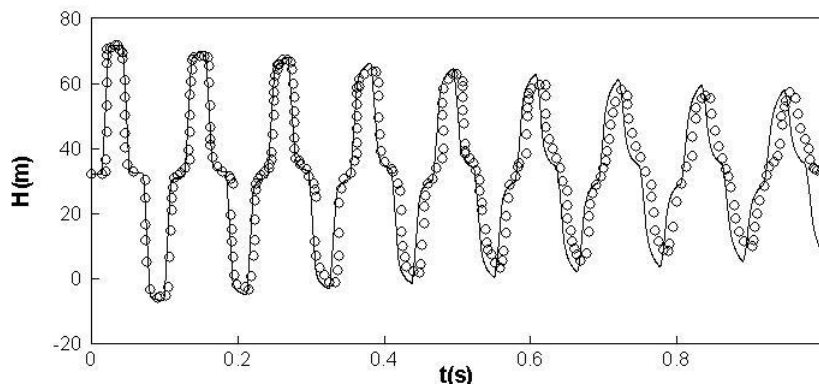
(a) $x = 0.5$

Fig. 3 - Comparison of analytical results with experimental data by Bergant et al.[18] for case 2. Solid lines (analytical results), circles (experimental data).

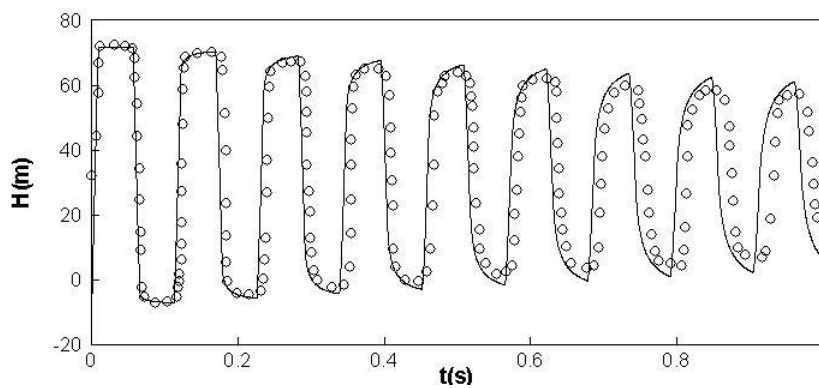


(b) $x = 1.0$

Fig. 3 - Comparison of analytical results with experimental data by Bergant et al.[18] for case 2. Solid lines (analytical results), circles (experimental data).



(a) $x = 0.5$



(b) $x = 1.0$

Fig. 4 - Comparison of analytical results with experimental data by Bergant et al.[18] for case 3. Solid lines (analytical results), circles(experimental data).

Effects of valve closing laws on water hammer pressure

There are mainly four types of closing laws for velocity $u(t)$, including: 1) Convex closing laws; 2) Linear closing law; 3) concave closing laws; 4) sudden closing law. And the following closing function is proposed by Provenzano et al. [12].

$$u(t) = U_0 \left[1 - \left(\frac{t}{t_c} \right)^m \right] \quad (36)$$

Where, m is the exponent. $m < 1$ is concave closing law, $m = 1$ is linear closing law and $m > 1$ is convex closing law. In the following part of this section, dimensionless variables will be used. Figure 5 is the valve closing laws with different exponent m . And $\varepsilon = 0.02$ is used in this case. Different values of dimensionless valve closing time t_c (as is defined in equation (9)) are also chosen to analyse its effects on pressure variations, where the water hammer period is $t_c = 4$ and $t_c = 2$ is the critical value for direct and indirect water hammer.

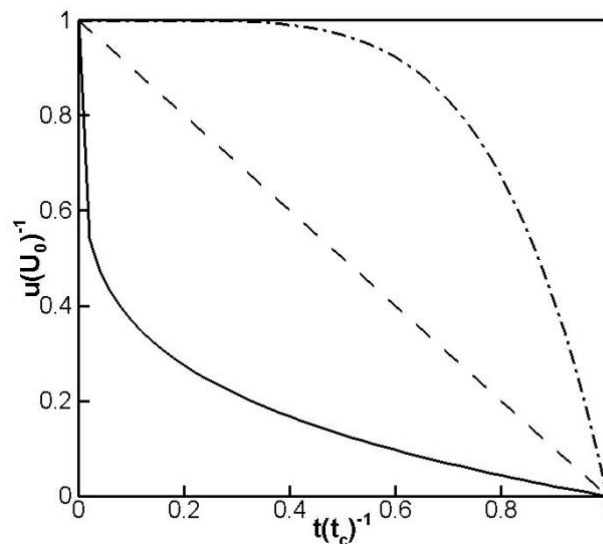


Fig. 5 - Valve closing laws with different exponent m . Solid line ($m = 0.2$), dashed line ($m = 1$), dash-dot line ($m = 5$).

With three closing laws, the results of dimensionless pressure p at valve end ($x = 1$) are given in Figures (6), (7) and (8). From the figures, it can be found that the shapes and amplitudes of pressure vary significantly for different m . For $m = 0.2$ which represents a fast valve closing followed by a slow valve closing, it can be found from Figure (6) that the pressure increases rapidly then slowly and reaches the maximum value. While for the case $m = 5$, which represents a slow valve closing followed by a fast valve closing, the water hammer pressure first increases slowly then rapidly, and finally reaches its maximum value. The shapes of the pressure variations are proved to be related to the valve closing laws.

And with the increase of closing time t_c , the maximum amplitudes of the cases with $m = 0.2$ and $m = 5.0$ decay slowly. More specifically, the maximum pressures with $t_c = 1.5$ for both $m = 0.2$ and $m = 5.0$ are 1. And when the closing time increases to $t_c = 4.5$ (note that critical value of valve closing time is $t_c = 2$), the maximum pressures become 0.849 and 0.894 respectively, with decreases of 15.1% and 10.6%. However, for the case with $m = 1.0$, the maximum amplitudes become smaller quickly. A decrease of 56.6% is found when closing time increases from $t_c = 1.5$ to $t_c = 4.5$. On the other hand, for constant valve closing time the maximum amplitudes of pressure

change obviously with different m . This means that optimization of valve closing laws is an effective way to reduce water hammer pressure.

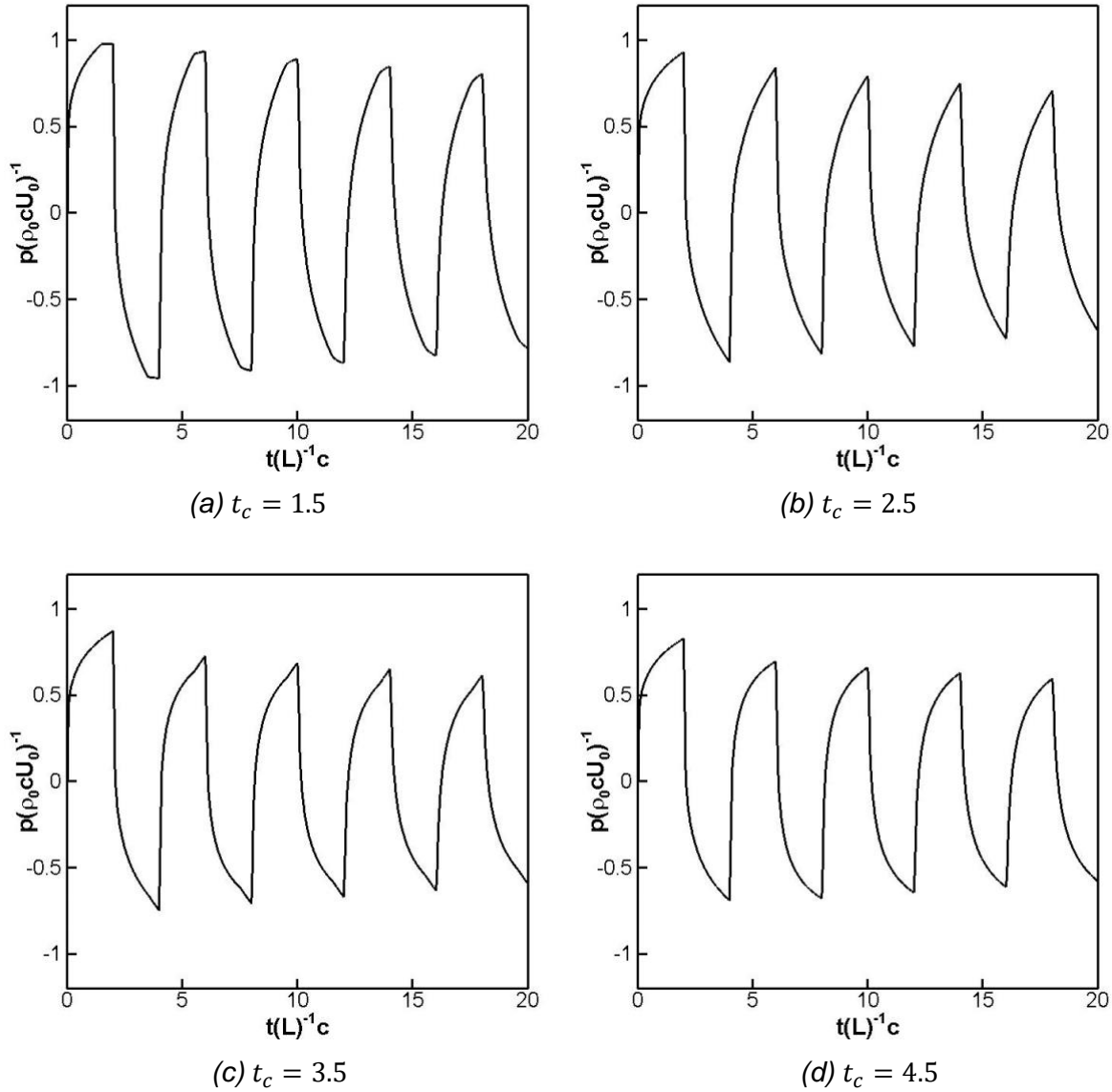


Fig. 6 - Pressure p at valve end with $m = 0.2$ and different closing time.

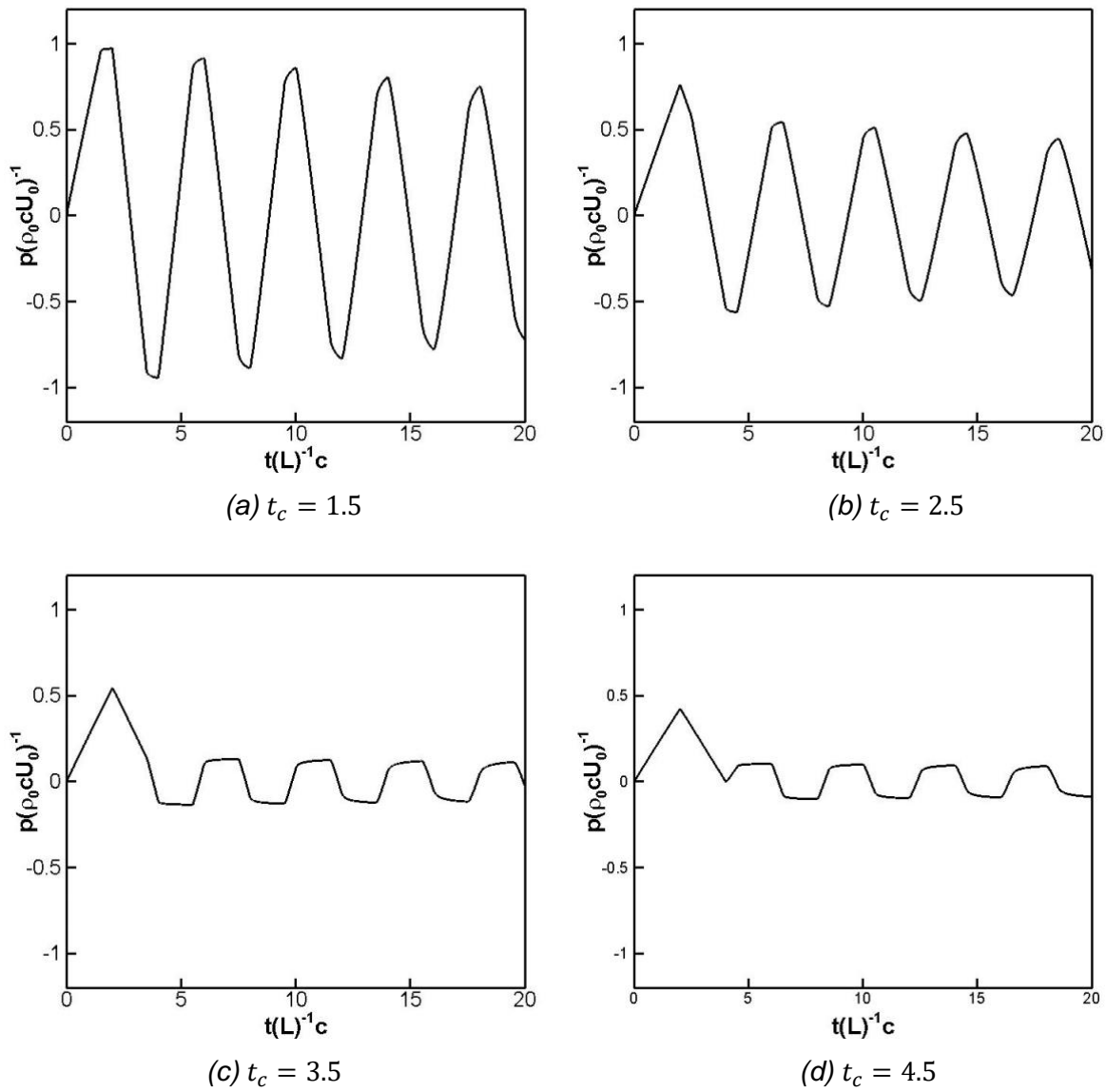


Fig. 7 - Pressure p at valve end with $m = 1$ and different closing time.

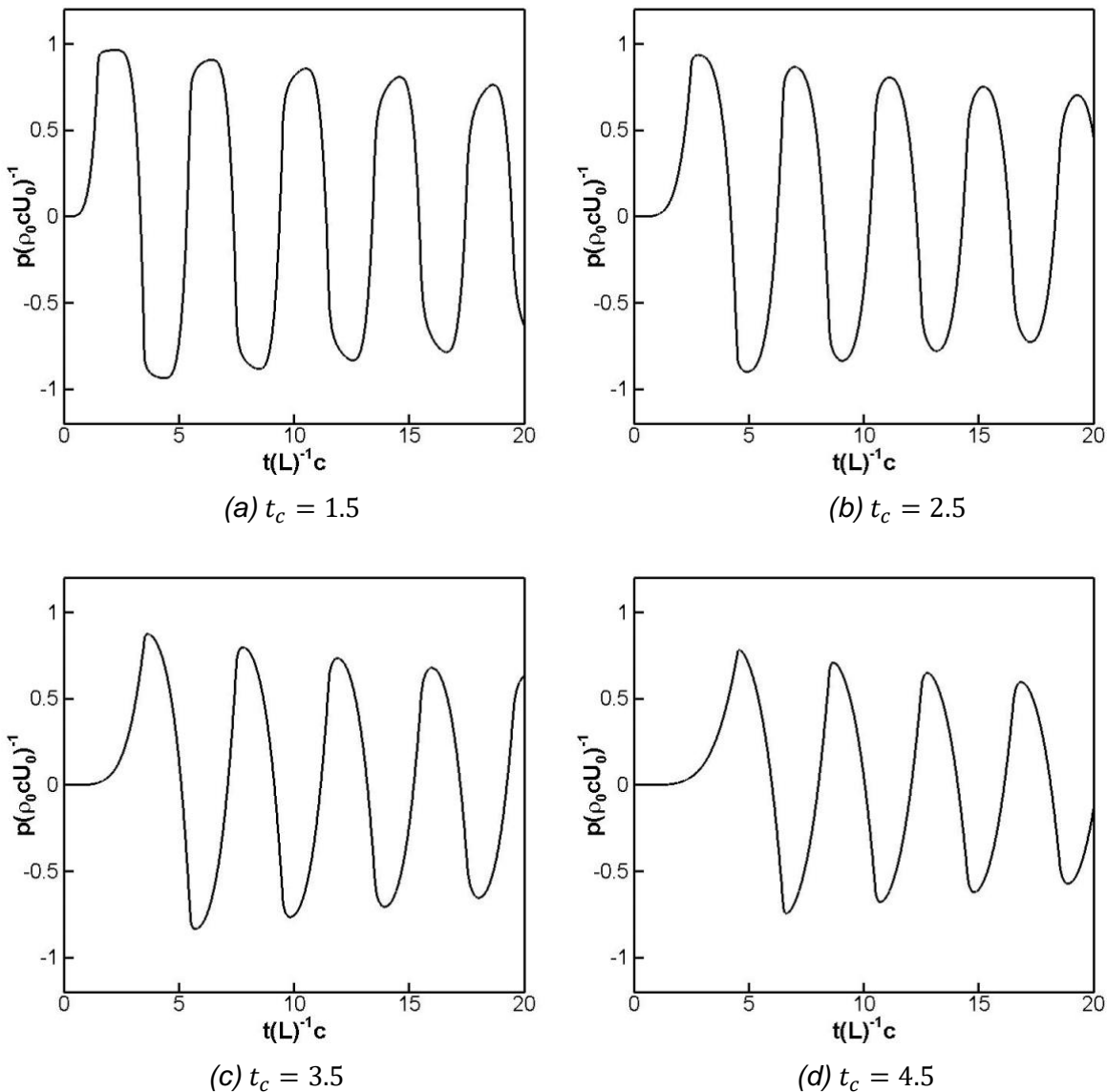


Fig. 8 - Pressure p at valve end with $m = 5$ and different closing time.

Relations to the decrease of valve opening

In the above analysis, different schedules of flow velocity variation at valve end are used, however in practical engineering the schedule of valve opening are used and controlled to reduce water hammer pressure. Hence, it is necessary to relate the two ways. At valve end, the pressure head loss and the velocity in dimensional form are related as follows [20].

$$h = \frac{p}{\rho g} = K_L \frac{u^2}{2g}, \quad x = L \quad (37)$$

Where, K_L is the valve loss coefficient which is dependent on valve type and the valve opening $\kappa = A/A_0$. A is the instantaneous valve opening and A_0 is the area when the valve is fully open. For a given valve and schedule of flow velocity variation at valve end, the schedule of valve opening $\kappa(t)$ can be obtained by combining Equation (37) and (35). Taking a gate valve as example, the relation of loss coefficient K_L and valve opening κ is determined and expressed as follows[21].

$$K_L = \left(\frac{1 + 0.632\sqrt{1 - \kappa^2}}{\kappa} - 1 \right)^2 \quad (38)$$

For a linear decrease of flow velocity with different closing time at valve end, the resulted valve opening $\kappa(t)$ is presented in Figure 9. It can be found that the linear decrease of flow velocity at valve end indeed does not correspond with a linear closing of the valve. In practical engineering, the optimal velocity variations at valve end can be transformed to the variations of valve opening by this method.

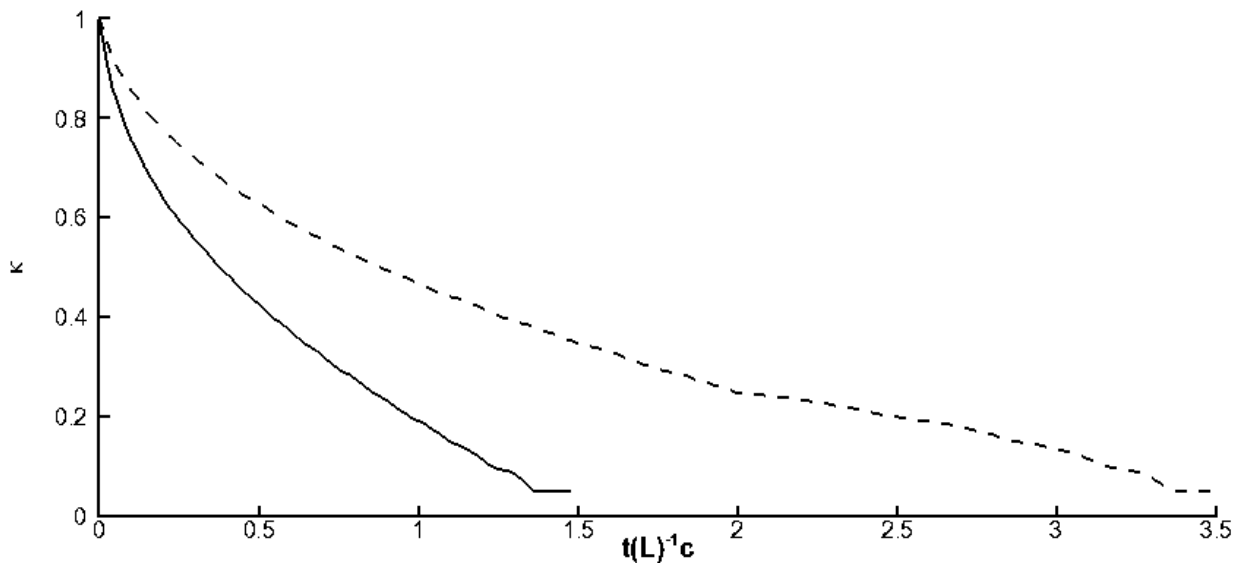


Fig. 9- Variation of valve opening for a linear decrease of flow velocity (gate valve). Solid line: $t_c = 1.5$, dashed line: $t_c = 3.5$.

CONCLUSION

In this study, a new analytical solution for water hammer in simple reservoir-pipe-valve system is derived by using Laplace transform method. The main differences with previous studies are that both effects of valve closing laws and unsteady wall friction are included in this solution. To validate the solution, experimental data is used by comparing against analytical results of this study. Effects of different valve closing laws on water hammer pressure variations are also studied. Relation of flow velocity decrease at valve end and decrease of valve closing is also proposed. The main conclusions are given as follows.

After comparing with experimental data, the new solution is proved to be suitable for water hammer prediction with initial laminar unsteady flow and low Reynolds number turbulent flow. Comparing the results of three types of closing valve laws, these are convex closing law, linear closing law and concave closing law, the shapes and amplitudes of pressure p at valve end vary obviously. With the increase of closing time, the maximum amplitude of pressure decay faster for linear closing law than that for other two closing laws. And for the same closing time, the maximum amplitudes of different closing laws vary obviously. By using the local head loss formula of valve, it is easy to transform the decrease of flow velocity at valve end to the decrease of valve closing.

In practical hydraulic engineering, the flow is turbulent with high Reynolds number. Analytical solution with unsteady turbulent friction is expected. While analytical solution derived in this paper is still very useful. Firstly, it can be used to validate numerical methods. Secondly, this solution can be employed for the detection of leaks and blockages where the transient flow can be

controlled to be laminar. Besides, for optimization of valve closing laws to control water hammer accurately, this analytical solution is a better choice than the numerical solution.

ACKNOWLEDGEMENTS

This study is supported by the Natural Science Foundation of Education Department of Shaanxi Province, China (No. 16KJ1543).

REFERENCES

- [1] Kodura A., 2010. Influence of valve closure characteristic on pressure increase during water hammer run. Environmental engineering III. Taylor & Francis Group, London.
- [2] Zielke W., 1968. Frequency-dependent friction in transient pipe flow. Journal of Basic Engineering, vol. 90: 109-115.
- [3] Brunone B, Golia UM, Greco M., 1995. The effects of two-dimensionality on pipe transients modeling. Journal of Hydraulic Engineering, vol. 121, no.12: 906–912.
- [4] Mitosek M, Szymkiewicz R., 2012. Wave Damping and Smoothing in the Unsteady Pipe Flow. Journal of Hydraulic Engineering, vol. 138, no. 7: 609-628.
- [5] Bergant A, Tijsseling AS, Vítkovský JP, et al., 2008. Parameters affecting water-hammer wave attenuation, shape and timing—Part 1: Mathematical tools. Journal of Hydraulic Research, vol. 46, no.3: 373-381.
- [6] Zhao M, Ghidaoui MS., 2004. Godunov-type solutions for water hammer flows. Journal of Hydraulic Engineering, vol. 130, no.4: 341-348.
- [7] Yao E, Kember G, Hansen D., 2015. Analysis of water hammer attenuation in applications with varying valve closure times. Journal of Engineering Mechanics, vol.141: 04014107-1.
- [8] Ghidaoui MS, Zhao M, Mcinnis DA, Axworthy DH., 2005. A review of water hammer theory and practice. Applied Mechanics Reviews. vol. 58 no.1: 49-76.
- [9] Bohorquez J, Saldarriaga J., 2015. Valve operation optimization for minimizing transient flow effects in water distribution systems(WDS). application to main pipes in Bogota, Colombia. World Environmental and Water Resources Congress: Floods, Droughts, and Ecosystems, May 17--21, 2015, Austin.
- [10] Streeter VL, Wylie EB., 1967. Hydraulic Transients. McGraw-Hill, New York.
- [11] Azoury PH, Baasiri M, Najm H., 1986. Effect of valve-closure schedule on water hammer. Journal of Hydraulic Engineering, vol. 112: 890-903.
- [12] Provenzano PG, Baroni F, Aguerre RJ., 2011. The closing function in the waterhammer modeling. Latin American applied research, vol. 41: 43-47.
- [13] Bazargan-Lari MR, Kerachian R, Afshar H, Bashi-Azghadi SB., 2013. Developing an optimal valve closing rule curve for real-time pressure control in pipes. Journal of Mechanical Science and Technology, vol. 27: 215-225.
- [14] Chen T, Xu C, Ren Z, Loxton R., 2015. Optimal boundary control for water hammer suppression in fluid transmission pipelines. Computers & Mathematics with Applications, vol.69, no.4: 275-290.
- [15] Cao HZ, He ZH, He ZY., 2008. The analytical research on the wave process and optimal control of water hammer in pipes. Engineering Mechanics. Vol. 25, no.6: 22-26.(in Chinese)
- [16] Xuan LJ, Mao F, Wu JZ., 2012. Water hammer prediction and control: the Green's function method. Acta Mechanica Sinica, vol.28, no.2: 266-273.
- [17] Mei CC, Jing HX. 2016. Pressure and wall shear stress in blood hammer-analytical theory. Mathematical Biosciences. vol. 280: 62-70.
- [18] Bergant A, Simpson AR, Vitkovsky J., 2001. Developments in unsteady pipe flow friction modelling. Journal of Hydraulic Research. vol.39, no.3: 249-257.
- [19] Jing HX, Zhang DS, Li GD., 2018. Pressure variations of fluid transients in a pressurized pipeline. Fluid Dynamics Research. Vol. 50: 045514.
- [20] Larock BE, Jeppson RW, Watters GZ, 2000. Hydraulics of pipeline systems. CRC Press.
- [21] Jović V, 2013. Analysis and modelling of non-steady flow in pipe and channel networks. John Wiley & Sons, Ltd.

CHECKING THE ACCURACY OF LABORATORY TESTS

Otto Dvořák, František Wald

University Centre for Energy Efficient Buildings of Czech Technical University in Prague, Třínecká 1024, 273 43 Buštěhrad, Czech Republic; otto.dvorak@uceeb.cvut.cz

ABSTRACT

In fire engineering, the quality of results of crucial test methods is key for validation of advanced numerical models. Therefore, it is important that the correct functioning of the test equipment and test procedures is achieved. This contribution is an assessment of the accuracy respectively the precision of the test methods based on the knowledge of the repeatability r and the reproducibility R determined by the round robin test (inter laboratory comparison) with reference testing materials.

KEY WORDS

Repeatability; Reproducibility; Repeatability limit; Reproducibility limit; Test method; Test result; Accuracy; Precision; Test apparatus; Reference material

INTRODUCTION

Thermal technical and fire characteristics of materials are important input data of CFD fire models that determine the quality of their predictions. These characteristics are usually determined by ISO, IEC, CEN or national test standards/procedures. These standards are validated. Standards for the determination of thermal technical characteristics of materials/products sometimes specify the conformity of measurements under repeatability and reproducibility conditions using the repeatability limits r and the reproducibility limits R . They also contain procedures for verifying the correct function of the test apparatus by comparing the difference between the test results measured by the interlaboratory or intralaboratory comparison on CRM (Certified Reference Materials) or SWS (Secondary Working Standards) substances/materials and their nominal values, with the tolerance expressed in the relevant standards with the r and/or R inequality.

The repeatability limit, r is the difference between the two test results obtained by the same operator with the same instrument under constant operating conditions on the same test material over the long term under the normal and correct execution of the test method exceeded the value given in the standard only in one case from twenty. (e. g. $r = 1.4 \text{ }^\circ\text{C}$ (see EN ISO 13736 [1])).

The reproducibility limit, R is the difference between the two individual and independent test results obtained by different operators working in different laboratories with the same test material over the long term under the normal and correct execution of the test method exceeded the value in formula (3) only in one case of twenty. (e. g. $R = 3.2 \text{ }^\circ\text{C}$ (see ISO 13736 [1])).

The above quoted standard requires verification after purchase experimental apparatus and subsequently periodically to verify its trueness/ not damage either:

a/ with one test performed on CRM and SWS, with the difference between a single result and a CRM or SWS reference value being within the following tolerance:

$$|x - \mu| \leq R/\sqrt{2} \quad (1)$$

where:

$x...$ is the test result,

$\mu....$ is the certified CRM value or SWS reference value,

$R...$ is the limit of reproducibility of the test method,

b) or n-times repeated tests performed on CRM or SWS; the difference between the average of n results and the CRM certified value or the SWS reference value should be within the following tolerance:

$$|\bar{x} - \mu| \leq R_1/\sqrt{2} \quad (2)$$

where:

$\bar{x}...$ is the arithmetic mean of repeated test results,

$\mu...$ is the CRM certified value or SWS reference value,

$R_1...$ is equal to the formula given by formula (3):

$$R_1 = \sqrt{R^2 - r^2(1 - 1/n)} \quad (3)$$

where:

$R...$ is the limit of reproducibility of the test method,

$r...$ is the limit of repeatability of the test method,

$n...$ is the number of retests performed on CRM or SWS.

The question is, whether the above mentioned inequalities are statistically correct.

Statistical model

The error of the determination result can be defined as the difference between the result and the actual / reference value of the measured quantity, i.e. according to equation (4)

$$x - \mu = \xi + e \quad (4)$$

where:

$x...$ is the test result,

$\mu...$ is the actual / reference value of the measured quantity,

$\xi...$ is the error caused by deviation from defined experiments conditions,

$e...$ is the random error that occurs even if the repeatability conditions are met,

The variance of the total error ($X - \mu$) denote σ^2 , equals the sum of the variance ξ and the variance ϵ according to the Equation:

$$\sigma^2 = \sigma_\xi^2 + \sigma_e^2 \quad (5)$$

where:

$\sigma^2...$ is the total variance under reproducibility conditions,

$\sigma_\xi^2...$ is the component of the whole variance representing the variability of uncontrollable factors,

$\sigma_e^2...$ is the variance under repeatability conditions.

These components of the total variance correspond to the respective reproducibility limits R value and repeatability r . If R and r are known from the round tests (e.g. they were determined during validation of the test method), the test concerned standard requires that two measurements x_1 and x_2 , measured under the following conditions:

1. the repeatability met the following criterion with a probability of 0.95:

$$|x_1 - x_2| \leq r \quad (6)$$

If the difference is greater than r , i.e. according to Equation (7), we would consider the measured values as being overloaded by an excessive error (as "unrepeatable").

$$|x_1 - x_2| > r \quad (7)$$

2. the reproducibility met the following criterion with a probability of 0.95:

$$P((x_1 - x_2) \leq R) = 0.95 \quad (8)$$

If the difference is greater than R , i.e. according to Equation (8), we would consider the measured values as being overloaded by an excessive error (as "unreproducible").

$$|x_1 - x_2| > R \quad (9)$$

If the reference / nominal values μ of measured variables, such as CRM or SWS materials, are available, then a pair of x_1 and x_2 values is not necessary to verify e.g. the "reproducibility" of the results; one measurement/one result would be sufficient, but the following criterion would have to be met:

$$P((x) \leq R/\sqrt{2}) = 0.95 \quad (10)$$

If the reference value μ of the measured quantity is known and a possibility of repeating this determination is possible, the determination can be realized of either:

a/ **n- times under repeatability conditions** (same day, in the same laboratory, on the same apparatus, with the same operator),

b / or **n- times under reproducibility conditions** (e.g. in n different laboratories, other times, on a third-party apparatus, of course, with other staff).

Ad a /

By selecting a particular laboratory, the measurement date, a specific operator, and a test equipment is chosen a specific system of repeatability conditions. Then a total error $(x - \mu)$ is equal to the sum of the error of this particular system ξ and the arithmetic error mean \bar{e} under repeatability conditions, that is

$$|\bar{x} - \mu| = \xi + \bar{e} \quad (11)$$

This corresponds to variable:

$$\text{Var } |\bar{x} - \mu| = \text{Var} (\xi) + \text{Var} (\bar{e}) \quad (12)$$

From the Equations (5) ($\sigma_{\xi}^2 = \sigma^2 - \sigma_e^2$) and (12) result that:

$$\text{Var } |\bar{x} - \mu| = \sigma^2 \cdot \sigma_e^2 + \sigma_e^2 / n = \sigma^2 - \sigma_e^2 (1 - 1/n) \quad (13)$$

Since σ^2 and σ_e^2 are proportional to the limits of reproducibility R and repeatability r (in the same order), equation (13) can be rewritten as follows:

$$|\bar{x} - \mu| \leq \frac{1}{\sqrt{2}} \cdot \sqrt{R^2 - r^2(1 - 1/n)} \quad (14)$$

The validity of the above criteria according to Equations (2) and (3) is confirmed.

Furthermore, it is clear that failure to meet the criterion $|\bar{x} - \mu| \leq R_1 / \sqrt{2}$ indicates that:

- a) a test device/method does not meet the required reproducibility limit or,
- b) a laboratory in question is working with a large systematic error, or that the environment conditions are significantly different from normal conditions, etc.

Ad b /

The standard test method could further recommend in its Annex to the Testing Laboratory another option to verify the trueness of its test equipment and the trueness of the test by inter-laboratory comparison with another laboratory and with the same test sample, e.g. under reproducibility conditions.

Then, according to the laws of probability and mathematical statistics:

$$\text{Var } |\bar{x} - \mu| = \text{Var } (\xi + e) \cdot 1/n = \sigma^2 \cdot 1/n^1) \quad (15)$$

With a following assessment criterion:

$$|\bar{x} - \mu| \leq R / \sqrt{2}n \quad (16)$$

To complete:

- If the values x and μ on a specific experimental device are known, then on average of many repetitions should apply that $|\bar{x} - \mu| = 0$,
- if $|\bar{x} - \mu| \neq 0$, it signals a systematic error on the device,
- if $|\bar{x} - \mu| > \xi$, and $P(|\bar{x} - \mu| > \xi) = \alpha$

- balance sheet can be supplemented by:

- if $|\bar{x} - \mu| > \xi$, and $P(|\bar{x} - \mu| > \xi) = \alpha$
when α is the significance level,
 $\xi = 1,96.s$ when $\alpha = 0,05$
 $\xi = 1,64.s$ when $\alpha = 0,1$.

etc, when s (or σ) is the standard deviation of random errors,

- if from repeated measurements $|\bar{x} - \mu| > \xi$ (systematic error exists) then $\xi = 1,96. s / \sqrt{n}$

¹⁾ The variance of a random variable X is often referred in statistics either as $\text{Var}(X)$, (*variance* X), $\sigma^2(X)$, $s^2(X)$ or $D(X)$

and $\xi = t \cdot s / \sqrt{n}$. The selective standard deviation s can be estimated from the known formula

- $s = \frac{1}{n-1} \cdot \sum_1^n (x_i - \bar{x}^2)^{1/2}$, when the coefficient t depends on n and α . Related standards, see [2-7].

CONCLUSION

The practical applicability of the above mentioned criteria for the correct function of a test device has been confirmed by the facts according to the relations (1), (2) and (3).

A more precise justification of a test equipment provides inter laboratory comparison (round – robin test) with other laboratories and evaluating the determination results according to the above derived relationships (15) and (16).

This option could be recommended during the revision of test standards in the form of a supplement to an already established Annex for verification of test equipment. It could also be used by research laboratories developing new test methods and / or accredited testing laboratories or laboratories with a good laboratory practice.

When working with specific r and R values, they should not be labelled as repeatability and reproducibility, as is commonly in the standards, but correctly as the limits of repeatability and reproducibility [7].

ACKNOWLEDGEMENT

This work has been supported by the Ministry of Education, Youth and Sports within National Sustainability Programme I (NPU I), project No. LO1605 and the Ministry of Interior, project No. VI20162019034.

REFERENCES

- [1] EN ISO 13736: 2013. Determination of flash point- Abel closed cup method.
- [2] ISO 5725-1: 1994/Cor. 1:1998-02. Accuracy (trueness and precision) of measurement methods and results – Part 1: General principles and definitions.
- [3] ISO 5725-2: 1994/Cor. 1:2001-10. Accuracy (trueness and precision) of measurement methods and results – Part 2: Basic method for the determination of repeatability and reproducibility of a standard measurement method.
- [4] ISO 5725-3: 1994/Cor. 1:2001-10. Accuracy (trueness and precision) of measurement methods and results – Part 3: Basic method for the determination of the precision of a standard measurement method.
- [5] ISO 5725-4: 1994. Accuracy (trueness and precision) of measurement methods and results – Part 4: Basic method for the determination of the trueness of a standard measurement method.
- [6] ISO 5725-5: 1998/Cor.:2005-08. Accuracy (trueness and precision) of measurement methods and results – Part 5: Basic method for the determination of the precision of a standard measurement method.
- [7] ISO 5725-6: 1994/Cor.1:2001-10. Accuracy (trueness and precision) of measurement methods and results – Part 6: Use in practice of accuracy values.
- [8] ISO 3534-1:2006. Statistics – Vocabulary and symbols – Part 1: General statistical terms used in probability.
- [9] ISO 3534-2:2006. Statistics – Vocabulary and symbols – Part 2: Applied statistics.